1981

Spectroscopic analysis of gaseous air pollutants with tunable diode lasers

Tsu-Yen Chang
Iowa State University

Chang, Tsu-Yen

SPECTROSCOPIC ANALYSIS OF GASEOUS AIR POLLUTANTS WITH TUNABLE DIODE LASERS

Iowa State University PH.D. 1981

Spectroscopic analysis of gaseous air pollutants with tunable diode lasers

by

Tsu-Yen Chang

A Dissertation Submitted to the

Graduate Faculty in Partial Fulfillment of the

Requirements for the Degree of

DOCTOR OF PHILOSOPHY

Department: Chemistry
Major: Analytical Chemistry

Approved:

Signature was redacted for privacy.

In Charge of Major Work

Signature was redacted for privacy.

For the Major Department

Signature was redacted for privacy.

For the Graduate College

Iowa State University
Ames, Iowa

1981

TABLE OF CONTENTS

LIST OF TABLES

LIST OF FIGURES

I. INTRODUCTION

The world's attention to environmental pollution has grown by leaps and bounds during the past two decades. This trend is vividly reflected in the mushroom growth of texts, research reports, publications and conferences [1-11], both in the U.S. and around the globe, on the environmental issues since 1963. The environmental movement was highlighted by the passage of the Clean Air Act of 1970 by the U.S. Congress. The resultant awareness and understanding of mankind's impact on our environment have led to a conclusion that in order to preserve the living quality on the earth, it is essential to control and reduce further pollution and hence to secure a cleaner and safer environment.

One of the suggestions to achieve such a goal, made by American Chemical Society's Committee on Environmental Improvement in 1978, was "continued improvement in the analytical chemical methods needed to monitor, control and study the environment"[12]. The purpose of this research which has been envisioned along the same philosophy is two-fold. One is to solve some problems encountered when diode lasers are used as a tool for gaseous air pollutants studies. The other is to develop a new analytical method for monitoring gaseous air pollutants by taking advantage of certain characteristics of diode laser, photoacoustic detection and wavelength modulation. A brief introduction on the air pollution, its effects on the environment and a survey of current methods in measuring and monitoring the air pollutants will be presented in this chapter.

A. Air Pollution and Its Effects on the Environment

Air pollutants can occur in the forms of gases, solid particles, or liquid aerosols. Gaseous pollutants constitute about 90% of the total mass emitted to the atmosphere, while particulates and liquid aerosols make up the remaining 10% [8-13]. The study of gaseous pollutants will therefore lead us to a better understanding of the mechanism and subsequently the control of air pollution.

Gaseous pollutants are evolved primarily from the combustion of fuels and waste materials. For example, the burning of high-sulfur fuel is responsible for sulfur dioxide emission, and motor vehicles account for most of the carbon monoxide and hydrocarbon emissions in the atmosphere. These pollutants and their potential adverse effects on the environment have been studied extensively by scientists. Their finding clearly demonstrated that atmospheric constituents, both near ground and throughout the rest of the troposphere and stratosphere, affect the life on the earth either directly or indirectly.

Some pollutants, such as CO, H_2S, NH_3, SO_2, NO, NO_2, O_3 and mercaptans, are toxic. Others, like polycyclic aromatic hydrocarbons, aromatic amines, nitrosamines and vinyl chloride, are carcinogens or potential carcinogens [5]. In addition to the adverse effects on human beings, these pollutants may also cause deterioration of textiles, corrosion of metals and building materials and damage to vegetation [4,5,8,9].

Nitrogen oxides play important roles in the photochemistry of troposphere. Even as low as 0.5 ppm of nitrogen dioxide in the atmosphere

can trigger the formation of smog. The combination of particulates, smog and sulfur containing compounds in the air was thought to be responsible for air pollution episodes which caused thousands of deaths in London in 1952, and again hundreds of deaths in New York City in 1966 [9]. The presence of ammonia speeds up atmospheric sulfate production [14] and also combines with nitrate to form ultrafine particles, which not only cause acidification of precipitation but also reduce visibility.

Besides these direct adverse effects, air pollution also shows possible long range effects on the climate. Chlorofluorocarbons, e.g. freons, deplete stratospheric ozone layer which protects living matter from excessive exposure to ultraviolet rays [15,16]. Increasing carbon dioxide concentration in the atmosphere, as produced by the extensive burning of fossil fuels during the past few decades, is raising the global temperature due to the "greenhouse effect"[3,8,1]. It has been pointed out that even a relatively small increase in average temperature could be detrimental to the well-being of the human race. The disruption of food production cycle and the melting of ice in the poles even to the point of flooding a large part of the world are two of the most ominous examples.

To realize the effects of various pollutants on the environment is an important matter. However, it is also equally important to understand the connection between sources of air pollution and the location of a critical receptor of the pollutant. It involves the transport, transformation and dispersion of the pollutant through the atmosphere. A complete and thorough analysis of the transport and

diffusion of pollutants in a given region is necessary for the purpose of determining the cumulative concentrations at all points within the region as a function of time. Thus, accurate mathematical models can be established and be utilized for future predictions. Therefore, monitoring methods are needed to provide spatial and temporal information. Two kinds of monitoring methods are currently being explored. One stresses the in situ measurement capability using movable instruments. The other relies on the remote sensing capability by measuring either the integrated concentration (e.g. long path laser absorption) or concentration profile which can then be integrated (e.g. various LIDAR applications)[17].

B. Measurement and Monitoring of Gaseous Air Pollutants

The optimal analytical technique to be employed in a particular monitoring exercise depends on the concentration range which is likely to be encountered and the time variation of the pollutant concentration. These factors are in turn largely dependent upon where the measurements are to be made.

Concentrations in the vicinity of a polluting source depend greatly on the source strength and wind direction. Large short-term variations in concentration may be observed. At locations increasingly removed from the sources, the short-term variations become progressively less. When the concentrations are varying rapidly, real-time continuous measurements are desirable in order to obtain meaningful information on peak levels. However, for most measurements of a 'background' type, e.g. determination of the general pollutant level in a particular region,

time resolution of less than one hour is not normally necessary.

In this section, analytical methods for the measuring and monitoring of gaseous air pollutants will be grouped into two categories: the existing methods and the laser monitoring methods, and will be discussed accordingly.

1. Existing methods

Existing analytical techniques for gaseous air pollutants analysis may be classified as chemical and physical methods [18].

Chemical methods utilize chemical properties of the species to be analyzed. These include colorimetric, acidimetric, electrochemical methods and so on. These methods generally have the disadvantage of a need of sample collection and preconcentration due to their low sensitivity. Sampling system and procedure have to be well designed in order to obtain quantitatively representative results and to avoid sampling errors. Besides, a sampling procedure can be time-consuming and hence makes continuous monitoring difficult. Therefore, these methods can only be employed to background type of measurements.

On the other hand, physical methods involve direct measurements of physical or optical properties, either of pollutant itself or following its interaction with another compound. They include chemiluminescence, fluorescence, absorption spectroscopy, mass spectrometry and chromatographic methods. Some of them may be combined to achieve a better result. Examples are GC/MS and GC/IR. In general, most of the physical methods can be employed to continuous monitoring and automated to satisfy many monitoring requirements.

In practice, chemiluminescence method has been widely used for the determination of ozone, nitrous oxide and sulfur containing compounds. Detection limit of sub-part-per-billion has been obtained [18]. Gas chromatography is by far the most widely used analytical technique for organic atmospheric pollutants. Unfortunately, it is usually not sensitive enough to measure ambient level pollutants without sample preconcentration, which will then introduce additional error and make continuous monitoring difficult. Infrared absorption spectrometry has historically been used to detect and to identify the constituents of air pollutants [19]. For example, it is officially recommended by National Institute for Occupational Safety and Health (NIOSH) for the carbon monoxide measurement in air [20]. Today, many commercially available gas analyzers for in-plant measurements are based on this principle and their sensitivities can be 0.02 ppm for some gases with 20-meter pathlength [21].

These automated, physical methods are generally precise and accurate. However, they are limited to single-point measurement and are usually reasonably reliable to about 0.01 ppm only. For the study of behavior and status of trace gases in the natural atmosphere at ppb level and below, this sensitivity is far from satisfactory. The need for these trace gas measurements has stimulated research further into more sensitive analytical techniques. Also, techniques for rapid, non-interfering source monitoring, pollutant transportation monitoring, spatial resolution monitoring, of ambient pollutant concentration need to be developed. For the routine monitoring of the atmosphere, techniques with adequate sensitivity, simple operation and reasonable cost have to

be available.

2. Laser monitoring techniques

Due to their simplicity, high sensitivity, speed of measurement, less interfering, higher specificity and selectivity, and potential of mutipollutant detection, the spectroscopic methods have allured scientists for their applications in pollutant monitoring since 1970 [22,23].

With the fast development of lasers, spectroscopic methods based on lasers for air pollution analysis have been exploited quite extensively during the past few years, and they appeared to be highly promising in various areas of application mentioned above [24-27]. Especially for the routine monitoring, it is increasingly evident that laser monitoring techniques may be the only answer.

The laser as a source offers four unique features unavailable in conventional incandescent light sources: high power, coherence, spectral purity and spatial collimation. Most laser monitoring techniques utilize all of these properties in their measurements. Because of the high spectral purity, and hence high resolution, these techniques generally offer greater flexibility of operation and can monitor a wider variety of pollutants. The high power, collimation and coherence have made remote sensing and long path monitoring feasible. Even though remote sensing has attracted inordinate attention, it should not be generally considered a substitute for point sampling, but only an adjunct to it. The use of lasers for point monitoring and refinements in correlation and Fourier transform spectroscopy can be equally important. Nevertheless, in some cases, remote sensing represents the only economical

or technically feasible technique.

The most promising laser monitoring techniques for gaseous air pollutants under development today are based on the principles of Raman scattering, resonance fluorescence and resonance absorption [26-28].

In Raman scattering, the wavelength of a backscattered radiation is shifted by an amount which is characteristic of the vibrational frequencies of the pollutants. Figure 1 shows the frequency shifts of the rotational-vibrational Raman spectra of typical trace molecules present in the atmosphere as well as the major atmospheric constituents, with respect to the transmitted laser frequency [29]. The estimation of the absolute concentration of each species can then be performed by comparing the Raman backscattered intensity with that of the Raman line from N_2 molecules which occupy the same volume [30-32]. Therefore, it can be used to monitor a variety of gases using a single, fixed frequency laser and has the ability to measure the actual number of pollutant molecules in a sample volume. It also shows a high potential as a remote sensing method. Unfortunately, it has the disadvantage that it requires a high power laser to achieve low detection limits because of the small Raman-scattering cross section. So this method will probably be limited to major atmospheric constituents and source monitoring. Besides, with a high power laser, eye safety becomes an important factor which further limits the use of this technique.

The resonance fluorescence process has typically higher cross sections than Raman scattering. However, its intensity suffers from quenching in the lower atmosphere because of the collosions with air molecules when used as a remote sensing technique. The sensitivity is

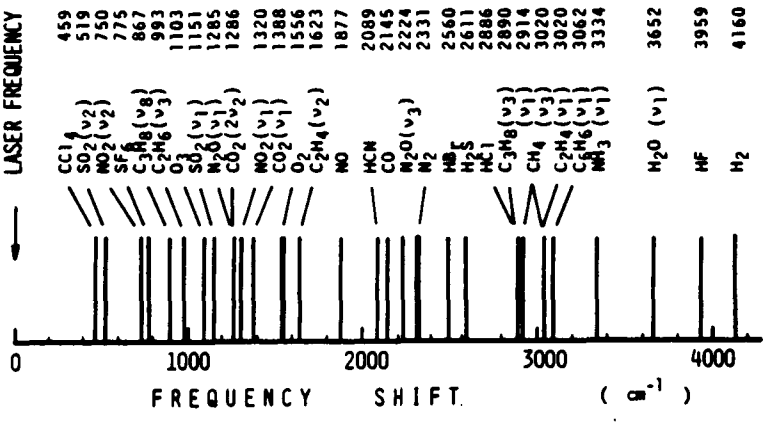

Figure 1. Frequency shifts of Q-branch of vibrational-rotational Raman spectra of typical molecules present in ordinary and polluted atmosphere relative to the exciting laser frequency.

thus usually too low for ambient air level, and is only suitable for source monitoring. Nevertheless, resonance fluorescence has a clear advantage in the remote monitoring of the upper atmosphere where the pressure is low and for point-sampling with a low pressure in gas cell. A point sampling system measuring nitrogen dioxide based on resonance fluorescence has been developed by Gelbwachs et al. [33] and Birnbaum and Tucker [34]. It can provide real-time, automatic monitoring of ambient atmospheric NO_2 levels. Detection limit of 1 ppb can be readily obtained. Okabe, et al. [35] have used a system with similar functional components to measure SO_2 fluorescence and obtained a detection range from 0.1-1600 ppm.

The method based on resonance absorption is the most sensitive one because absorption cross sections are the largest of the optical interaction and are not affected by quenching. Since most of the atmospheric pollutant gases have strong characteristic absorption lines in the so-called 'fingerprint' region (2-20 μm) of the infrared, the infrared lasers have thus attracted great attention for their uses in laser monitoring techniques.

There are four basic monitoring techniques for pollutant gases based on infrared absorption method. They are reduced-pressure point sampling for high specificity [36], in situ ambient air and source monitoring [37], single-ended remote monitoring [38] and long-path bistatic monitoring [23]. Each of these has its particular usefulness and makes specific demands on the laser.

Single-ended remote monitoring usually requires much higher power than other techniques. This high power can so far only be obtained from molecular gas lasers which can be tuned to different discrete emission

lines, such as CO_2 and CO lasers, or from those which can emit a line spectrum such as HF and DF lasers. However, they suffer from the fact that the detection of gases is limited almost entirely to accidental (usually partial) coincidence between their emission wavelengths and the spectral absorption lines of the gases to be analyzed [28,39,40]. On the other hand, the power requirement for other techniques can be met by different types of continuously tunable lasers, which offer the advantage of being able to scan through spectral absorption lines of molecular species. As a result, they will enable us to utilize their relatively large absorption cross sections to the fullest extent possible and at the same time to select wavelength regions with minimum potential interferences [41,42].

Some important tunable infrared lasers available at the present time are listed in Table 1, along with their power, wavelength coverage and highest resolution obtainable. Pulsed optical parametric oscillators (OPO) showed promise for remote space-resolved monitoring using topographic backscattering due to their high power [43]. However, this type of laser device does not offer a very narrow linewidth. The best obtained was only in the order of 10^{-3} cm^{-1} [44], which is not narrow enough for high resolution study of line parameters such as line position, linewidth, etc.

High pressure gas lasers (HPG lasers) have great potential in differential absorption systems using natural reflectors, but efforts remain in making them into practical devices [45]. Spin-flip Raman lasers (SFR lasers) have been applied to balloon-borne in situ measurement of NO to a height of 28 km in the stratosphere by Patel, et al. [46].

Table 1. Properties of tunable infrared lasers [47-49]

Tunable Source	Wavelength Region		Highest Resolution obtained (cm^{-1})	Typical Power (W)	
	overall (μm)	continuous (cm^{-1})		cw	pulsed
OPO	0.55-3.5 ($LiNbO_3$)	3000	1×10^{-3}	10^{-2}	10^5
	1.2-8.5 (Ag_3AsS_3)				
	8-12 (CdSe)				
Diode laser	1-34	2	3×10^{-6}	10^{-3}	10
SFR laser	3 (HF-pumped)	15		1	10^3
	5-6 (CO pumped)	50	1×10^{-6}		
	9-14 (CO_2 pumped)	100	3×10^{-5}		
HPG laser	9-11 (CO_2)	10	3×10^{-2}	1	10^5
Color-center Laser	0.88-3.3	500	10^{-5}	10^{-2}	

These lasers have higher power than diode lasers but their complex operation lowers their attraction and limits their uses in laboratory at the present time. Color-center lasers offer narrow line width (10^{-5} cm^{-1}) and have higher power than diode lasers [47]. However, their output wavelength does not cover the 'atmospheric window' region and therefore they have only limited uses in the study of air pollution. Tunable diode lasers have already been used for point monitoring, in situ source monitoring and long-path ambient air monitoring [25,48]. Because of their low-power, a retro-reflector is required in long-path monitoring. The small size, simple operation and low cost of such diodes have made them the most practical and desirable lasers for air pollution studies. In addition, their extremely narrow line width (10^{-6} cm^{-1}) have been used for accurate line parameter study of pollutant gases [49], which is the basis for the determination of their concentrations.

In this research work, the diode lasers are chosen, for the above-mentioned advantages, to study the possible improvement of the monitoring techniques for gaseous air pollutants. The diode lasers will be used first to demonstrate the accuracy of an internal calibration method for line positions and, at the same time how this method can be used to study other line parameters and pressure broadening coefficients. Secondly, the diode lasers will also be used in photoacoustic detection in which the wavelength modulation technique will be employed to improve the signal-to-noise ratio. The technical details as well as their potential uses in the analysis and monitoring of gaseous air pollutants, of these two schemes will be discussed in later chapters.

II. LITERATURE REVIEW

Since the first laser beam radiated from a ruby laser in 1960, a variety of lasers have been developed. Lasers with wavelengths extending from the infrared through the visible, to the ultraviolet region found widespread use in both industrial applications and academic research. Powerful, collimated, coherent, and monochromatic light emitted from lasers opened a new era for the spectroscopists and revolutionized the research on spectroscopy. Interactions with optical cross section considered too small by using conventional light sources, can now be observed due to the high power of the laser [50]. High resolution is obtainable because of the inherent high spectral purity of the laser. The best resolution attainable in the infrared region from the grating monochromator is about 0.07 cm^{-1} [51], but with infrared lasers 0.001 cm^{-1} can be easily achieved [52]. The extremely short pulse available from lasers enables one to study very rapid transition of the atoms and molecules.

Among the many types of lasers, the tunable diode laser is chosen and used in this research work. Therefore, I elect to review the literature only related to this type of laser in this chapter. The operational principle and characteristics of the diode lasers will be discussed first followed by the discussion of their drawbacks. The application of diode lasers to high resolution spectroscopy and to line parameter study of gaseous air pollutants has been very successful. It will be reviewed along with its existing calibration problem. The analytical techniques for monitoring atmospheric constituents and pollutant gases

by the use of diode laser spectroscopy will then be reviewed in the last section of this chapter.

A. Operational Principle and Characteristics of Tunable Diode Lasers

Tunable diode lasers, also called semiconductor diode lasers, are made of semiconductor diodes. They include some binary compounds such as InSb, InAs, GaSb, PbSe, PbS, PbTe, and pseudobinary alloys such as $Pb_{1-x}Sn_xTe$, $PbS_{1-x}Se_x$, $Pb_{1-x}Sn_xSe$, $GaAs_xSb_{1-x}$, $Hg_{1-x}Cd_xTe$ and $In_{1-x}Ga_xAs$. Among them, the lead-salt diode lasers are the most useful in infrared spectroscopy and air pollution study. Detailed discussions on their operational principles and characteristics can be found in recent review articles [53-56]. Only the basics will be discussed here and special emphasis will be placed on their optical properties.

The diagram of a typical lead-salt semiconductor diode laser is shown in Figure 2 [57]. If current is applied across the p-n junction of the diode, electrons from the n-type material, and holes from the p-type material are simultaneously injected into the junction region and the electron-hole recombination occurs. This recombination process emits photons with a wavelength corresponding approximately to the semiconductor energy bandgap. Since the active region is contained in the polished end faces of the semiconductor crystal, which serves as an optical resonator, laser action thus can occur. The laser emission occurs at a wavelength λ_m determined approximately by the Fabry-Perot equation:

$$m\lambda_m = 2\,nl$$

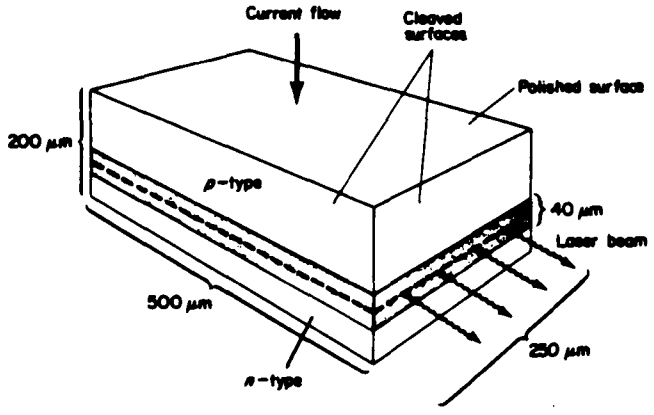

Figure 2. Diagram of a typical lead-salt semiconductor diode laser. The dashed line shows the position of the p-n junction; the radiation is emitted from an area 40 x 250 μm [57].

where n is the refractive index, l the cavity length and m the number of half-waves within the crystal cavity. At a certain applied current the laser radiation contains several longitudinal modes. Figure 3 shows the emission power-spectrum from a typical lead-salt diode laser [54], as recorded by a grating spectrometer having a resolution of about 0.1 cm^{-1}. The laser linewidth is narrower than 3×10^{-5} cm^{-1}. As shown in Figure 3, the diode laser is emitting radiation in five modes approximately 1.5 cm^{-1} apart under the specified operation conditions. The amount of separation agrees with the calculation based on a cavity length of 0.4 mm and an effective refractive index of about 6 [58].

The operation temperatures of the diode lasers are typically a few decades degrees Kelvin. Therefore, it is necessary to employ liquid helium as coolant or use a helium refrigerator to cool down the laser. The linewidth of this laser emission is extremely narrow. Hinkley and Freed [59] reported its Lorentzian linewidth as narrow as 54 KHz (1.8×10^{-6} cm^{-1}) by heterodyning a $Pb_{0.88}Sn_{0.12}Te$ laser, operating cw at 10.6 μm, with a stabilized single frequency CO_2 gas laser. The linewidth was found to vary inversely with power. Typical output power of a diode laser is less than 1 mw in cw. Efforts have been made to improve the power level, and will be discussed later in this chapter. A property of diode lasers that is different from other types of lasers is their exceptionally large ($\approx$ f/1) beam divergence, which is due to the diffraction effects caused by the small gain region. Therefore, focusing optics are required for the use of diode lasers.

Frequency tuning of the diode laser is achieved by change of chemical composition, temperature, pressure, injection current and

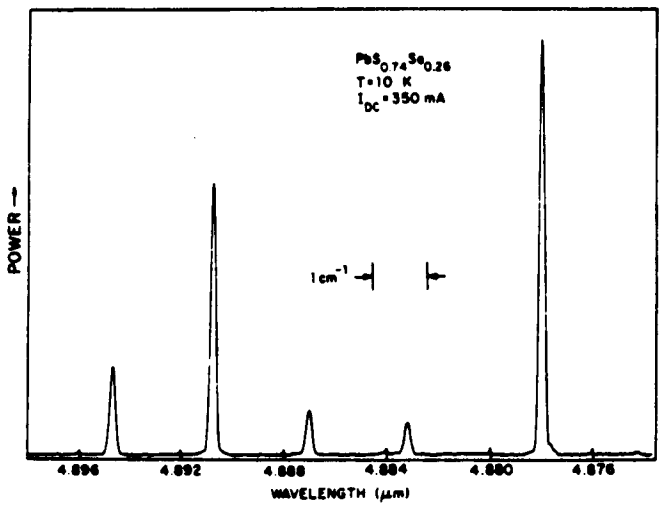

Figure 3. Emission power spectrum from a $PbS_{0.74}Se_{0.26}$ diode laser at a constant current of 350 ± 5 mA. The laser linewidth is less than 3×10^{-1} cm^{-1}; the spectrometer resolution is approximately 0.1 cm^{-1} [54].

magnetic field. The chemical composition of these semiconductor diodes can be adjusted to control their bandgaps, and hence the spontaneous emission frequency of diode lasers. The spontaneous emission frequency (ν_s) is approximately a linear function of the alloy composition factor x:

$$\nu_s \approx \nu_o + \delta x$$

where ν_o and δ are composition parameters. Therefore, the laser frequency can be coarsely tuned by adjusting the composition factor x. Finer tuning can be done by changing the temperature [60], applied pressure [61] or magnetic field [62] which affect the refractive index and/or the energy bandgap. However, continuous fine tuning by directly changing the temperature of the overall semiconductor crystal during a scan is not practical. Instead, it is much easier to change temperature by current tuning [63]. The heat dissipation (I^2R) caused by the injection current raises the temperature in the junction region of the semiconductor. This not only increases the energy gap and hence the emitted photon frequency, but also changes the effective cavity length through the change of the refractive index.

If during tuning, the spontaneous emission wavelength closely follows that of the laser emission, then continuous laser tuning over the entire range of spontaneous tuning can be achieved. But for the usual tuning mechanism as mentioned above, the laser frequency does not follow the spontaneous emission; thus, the continuous tuning range up to a few cm^{-1} wide is usually separated by discontinuous jumps. Typical current tuning rates are 1-30 cm^{-1}/A, with continuous tuning range of

1-3 cm^{-1} in a single mode. An example of current tuning curve is shown in Figure 4 [54]. Continuous tuning range with current tuning is usually wider than that of magnetic tuning which is typically only from 0.1 cm^{-1} to 0.4 cm^{-1}. Since the wider continuous coverage is very important to spectroscopic work, the current tuning has been used almost exclusively for this purpose. Pressure tuning can be used for discrete tuning. It provides a wider tuning range and does not sacrifice the high resolution capability of the lasers [64]. Combination of pressure tuning and current tuning enables one to use only a few laser crystals to cover the whole mid-IR region. However, extreme caution must be taken to prevent the laser crystals from crushing under the pressure. One thing noteworthy is that all these tuning rates are nonlinear [54]. Therefore their calibration has to be done carefully before the quantitative spectroscopy can be performed.

B. Limitations and Recent Advances on the Diode Laser Technology

In the past, wider application of the diode lasers had been limited by the relatively small cw output power (typically less than 1 mW) and the need of operating at cryogenic temperature (usually $\leq$ 77 K). The former limits the use of diode lasers in photoacoustic detection, saturation spectroscopy and as a local oscillator for heterodyne detection. The latter not only has limited the total tuning range of the diode laser, but also has actually posed economic problems for practical applications. In addition, the requirement of using a monochromator to eliminate the unwanted modes cuts off a significant portion of the

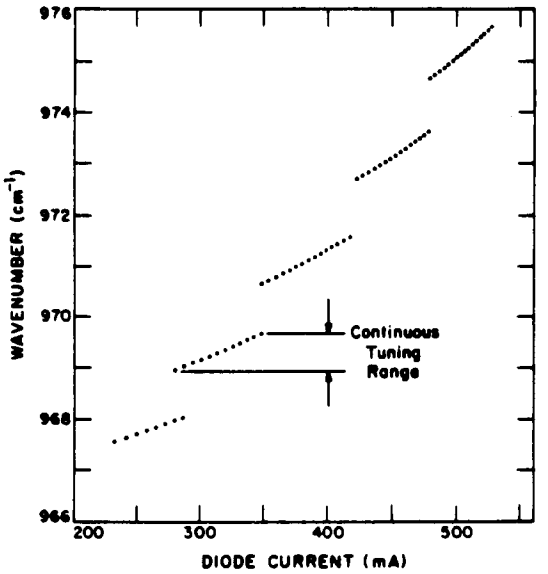

Figure 4. Current-tuning curve for a $Pb_{0.88}Sn_{0.12}Te$ diode laser operating cw in a liquid-helium-cooled dewar. The tuning is continuous within each of the five modes. The data points indicate peaks in transmission of the laser radiation through a Ge etalon having a free spectral range of 1.955 GHz used for relative frequency calibration [54].

already weak output power in a multimode beam. However, single mode laser emission is most desired for certain applications. Also desired are wider total tuning range so that only a few diodes are needed to cover the whole mid-infrared region, and wider continuous tuning range so that the high resolution spectroscopy can benefit most from it. Recent researches on the diode laser technology have made significant progress in both increasing the power level and achieving cw operation at higher temperatures. Along with this progress is the improved beam pattern and wider tuning range.

The optical quality of end mirror is one of the major factors which limits the output power of the lasers [65]. It is improved by polishing rather than cleaving to form reflecting end faces of the laser cavity. For some $Pb_{1-x}Sn_xTe$ crystals an order of magnitude higher laser output has been obtained with polished end faces. The use of reflective coatings on the back mirror further improves the diode performance.

A typical diode laser with its p-n junction extending across the entire width of the crystal, as shown in Figure 2, often operates in parasitic bounce modes due to the high refractive index of the crystal materials. This results in poor beam patterns and low efficiency. These bounce modes can be avoided by stripe geometry [60,66]. A diode laser with stripe geometry has a p-n junction confined in a region of 20-100 μm wide and 500 μm long with SiO_2 or MgF_2 on both sides of the active region. SiO_2 and MgF_2 have a lower refractive index than that of the diode material, and thus suppressed the bounce modes. With this geometry, the diode has been observed to essentially operate in a single

fundamental spatial transverse mode. The combination of stripe geometry and polished end mirrors on the fabrication of a PbS laser has made it possible to operate at 4.2 K with a cw output power as high as 370 mW with more than 50 mW in a single mode [67]. This represents the highest power ever observed from lead-salt diode lasers so far.

Stripe geometry diode lasers with heterostructure have been observed to operate at higher temperature (above 77 K in cw) and thus increase the total tuning range of the laser. The first single heterostructure (SH) $Pb_{1-x}Sn_xTe$ diode laser was reported in 1973 with cw operation up to approximately 65 K [68]. Recently, laser emission of $PbS_{1-x}Se_x$ SH diode at 130 K with mW single-ended output power in cw mode and an average tuning range of about 300 cm^{-1} have been reported [69]. $Pb_{1-x}Sn_xSe$ SH laser operating at 95 K with 3.9 mW output power and 300 cm^{-1} tuning range has been achieved [69].

Double heterostructure (DH) further improves the operation temperature of diode lasers in cw [70-73]. Groves et al. [72] fabricated a $Pb_{0.88}Sn_{0.12}Te$-PbTe stripe geometry DH laser by liquid phase epitaxy. This laser was reported to operate from 10.5 μm at 12 K to 8.2 μm at 80 K, with cw power of several mW. This is a total tuning range of nearly 280 cm^{-1}, about a factor of 10 over conventional homojunction $Pb_{1-x}SnTe$ lasers. Another such laser diode grown by molecular-beam epitaxy [7] has performed laser emission up to 114 K in cw with even wider tuning range extending from 15.9 to 8.54 μm (540 cm^{-1}). The total output power was only at the 100 μW level. However, it was predicted that tens of mW can be achieved with a modified package design and improved mounting techniques. By hot-wall molecular-beam epitaxial

method, Preier et al. [73] have fabricated PbS-PbSe DH laser with cw operation of several hundred μm up to 120 K with tuning range of 360 cm^{-1}. Pulsed operation at 5.5 μm has been achieved at temperature up to 230 K [74].

Frequency selectivity can be improved by fabricating a grating in the surface of the active region using photoresist and etching techniques. Such lasers, called distributed feedback (DFB) lasers, will operate in a single mode for a large variation in diode current and heat-sink temperature. DFB lasers made from $Pb_{1-x}Sn_xTe$ diodes with double heterostructure stripe geometry have been reported to offer extraordinary wide continuous tuning range and to be able to operate at both pulsed and cw modes at temperature up to 50 K with continuous current tuning of mode frequency up to 7 cm^{-1} [75].

However, these devices can only be tuned in this narrow range. No wide range coarse tuning is possible. If a certain tuning range has to be adjusted, very high precision in choosing the proper grating spacing and composition of the active region has to be fulfilled. Today, only laboratory samples exist. Only time will tell whether these devices can be fully developed to be put into practical uses.

Recently, Walpole et al. [75], Lo [76, 77] and Partin and Lo [78] have been trying to make some homostructure diode lasers with compatible performances as those of heterostructure. The idea was to fabricate lasers from single crystals having a graded charge carrier concentration. Since a gradient in carrier concentration produces a gradient in the index of refraction, the photons generated in the active region tend to be confined there. This improved photon confinement should result in a reduction in

absorption coefficient and hence lead to higher temperature operation. The photon confinement in these devices is not as good as in DH laser, but it does have another advantage of being more stable to thermal cycling [79]. Homostructure $Pb_{1-x}Sn_xTe$ diode lasers have been reported to lase single-mode with single-ended output power up to 0.9 mW and a cw tuning range of 216 cm^{-1}, over a temperature range from 11 K to 61 K [76]. The same group of scientists also fabricated homostructure $PbS_{1-x}Se_x$ diodes operating up to 90 K in cw modes with tuning range of 350 cm^{-1} [77] and PbTe diodes operating up to 85 K in cw modes with tuning range of 280 cm^{-1} and cw output power of 3.5 mW [78]. After comparing these homosturucture and heterostructure lasers, Lo et al. [76] concluded that, by using a simple diffusion process, one can make a homostructure laser that is capable of operating at high temperatures just like most heterostructure lasers reported so far.

Another important factor affecting the practical uses of diode lasers is their long term stability, which is excellent if they are kept at low temperature. Stability problems occur because of temperature cycling and interdiffusion effects at room temperature. Interdiffusion can be avoided if no direct contact of the lead salts with In, the main diffusant, exists. Cycling stability over more than 100 temperature cycles has been obtained recently by replacing MgF_2 or SiO_2 by anodic oxides as masking materials of stripe geometry and by choosing packages which maintain constant heat transfer properties [56].

C. Calibration of Diode Laser Frequency

Tunable diode lasers have been successfully applied to high resolution spectroscopy and to pollution monitoring. The characteristic of these lasers makes them ideally suited for such applications is their very narrow linewidths ($10^{-6}cm^{-1}$). Naturally, to take advantage of the monochromaticity, reliable means of spectral calibration must be available. This is particularly important since the various methods of tuning for these lasers all result in nonlinear tuning rates. To complicate matters, the diode junctions usually go through unpredictable and irreversible changes each time they are cycled through the operating (cryogenic) temperatures. This makes it necessary to perform spectral calibration each time they are used, even if the operating temperature is identical.

The calibration scheme consists of two parts. One is the establishment of absolute frequency standards. The other is the calibration of the laser tuning rate relative to these standards.

The simplest procedure to calibrate the absolute absorption line positions is to use a monochromator or interferometer to measure the laser frequency. This is quite straightforward for the diode lasers because the monochromator is used to select the desired mode and is part of the experimental setup. However, this device can provide an accuracy of only about $\pm$ 0.01 cm^{-1} at best. It is not sufficient for high resolution analysis.

A better procedure is to calibrate against a simple gaseous molecule contained in an absorption cell at low pressure, provided that (a)

its absorption lines have been well-studied to the necessary accuracy and (b) they are close enough to each other (≤ 0.5 cm^{-1}). The latter ensures that at least one standard line will be seen in the continuous tuning range. Cole [80] has compiled for IUPAC the line positions of some simple molecules to be used as calibration standards with an absolute accuracy of 5×10^{-3} to 10^{-4} cm^{-1} over the region 1-4350 cm^{-1}. However, this compilation was intended for the calibration of grating spectrometers. The accuracy of these line positions is not comparable with the resolution of diode lasers. And the lines are often not closely spaced as desired for laser spectroscopy. McClatchey et al. [81] and Rothman et al. [82] compiled line parameters of H_2O, CO_2, CO, N_2O, CH_4, O_2, O_3, NH_3, SO_2, NO and NO_2 for atmospheric absorption. Some of these data are known with high accuracy and can be used as calibration standards.

Recently, Knoll et al. [83] have used the best available molecular constants to calculate transition frequencies in the ν_2 bands of CO_2 (622 to 717 cm^{-1}) and HCN (564 to 858 cm^{-1}). They then measured HCN p(15) relative to the adjacent CO_2 Q(14) and Q(16) lines using an etalon for tuning rate calibration and found an agreement to within 0.0008 cm^{-1}. This is still not sufficient for ultra-high resolution purpose. Therefore, new measurements are needed to reap the full benefit of the available spectral resolution capability.

Lately, C_2H_4 has been suggested as a calibration gas near 10.5 μm and OCS for 5.8, 9.5 and 11.6 μm [84-87]. Part of the ν_7 band of C_2H_4 has been recorded, and frequency splittings between individual transitions are reproducible to ± 0.008 cm^{-1} or better [84]. However, due to lack

of appropriate techniques for precise absolute frequency calibration, no absolute frequency was reported. On the other hand, some OCS lines near 9.5 μm have been measured to an estimated accuracy of ± 2 MHz by heterodyne technique [86]. Molecular constants were determined from experimental data. Wavenumbers, frequencies, and intensities of spectral lines of this band from 1025 cm^{-1} to 1074 cm^{-1} then were calculated and tabulated with uncertainty of ± 2 MHz for immediate use as reference standards. The 11.6 and 5.8 μm bands were studied similarly [87]. Line parameters in 815-892 cm^{-1} and 1662-1738 cm^{-1} regions were also tabulated.

The absolute frequency can also be calibrated against some gas laser frequencies that are known accurately. These lines can be introduced into the spectrum by inserting a high-voltage gain cell into the laser beam. The best known laser frequencies are those measured by frequency-mixing techniques, relative to the cesium-beam primary frequency standard. Lines in CO_2 laser band from 903-1099 cm^{-1} have been measured to ± 25 KHz or 8.3×10^{-7} cm^{-1} [88]. Methane-stabilized laser lines at 3.39 μm have been calibrated to within 43 KHz or 1.4×10^{-6} cm^{-1} and CO_2-stabilized laser lines at 10.17 μm to within 16 KHz or 5.5×10^{-7} cm^{-1} [89]. In the regions where these lines are available, they provide very accurate calibration standards.

Other laser frequencies calibrated against these best-known laser frequencies have uncertainties of a few MHz. CO_2 isotope laser lines have been measured to an accuracy of better than $10^{-4} cm^{-1}$ by comparing with a $^{12}C^{16}O_2$ reference laser [90,91]. CO laser lines have been measured with

an uncertainty of about $\pm$ 5 MHz, or 1.5 x 10^{-4} cm^{-1} [92]. They should be useful in the 5-7 μm region as secondary frequency standards.

In addition to the absolute frequency standards, the tuning rate relative to these standards has to be calibrated in order to measure the positions of the absorption lines of interest. There are many ways to do this. The most convenient and widely used approach is to use a reference Fabry-Perot interferometer [93,94], i.e., an etalon to produce relative frequency marker. Both solid germanium etalons and air-spaced etalons have been used for this purpose. When a solid etalon is used, the temperature must be stabilized to avoid changes in pathlength. Air-spaced etalon is much more stable against the temperature variation [93]. However, air-spaced etalon requires a much longer physical length to achieve a reasonably small free spectral range because of its low index of refraction. Because small changes in the angle of incidence of the laser beam on the etalon can affect the fringe spacing and thus cause calibration error, air-spaced etalon is therefore more susceptible to this type of error. A two-beam system which allows the simultaneous measurement of a gas spectrum and the etalon trace is desirable because the diode laser sometimes drifts in temperature, and consequently wavenumber, between one spectral scan and the next. Nevertheless, if the etalon is placed after the monochromator, the motion of the image of the diode laser at exit slit changes the angle of incidence onto the etalon, thus causes the error mentioned earlier [95]. To solve this problem, Chraplyvy [96] designed a dual-beam, single-detector system with the etalon located before the monochromator. But this design resulted in a 75% power loss at the detector. Jennings [94] constructed

a system which has the advantage of the Chaplyvy's design but with less power loss. Besides, the etalon must be calibrated against some other reference since a measurement of the physical thickness is insufficient in accuracy. Reddy et al. [93] have calibrated an air-spaced etalon with ν_2 lines of HCN. The relatively low output powers of the diode lasers prevent the use of highly reflective coatings on the etalons, and the finesse is generally poor. One can not expect an accuracy of better than $10^{-3}cm^{-1}$ for this calibration scheme.

A second approach is to make use of two or more known spectral lines of other molecules to establish a wavelength scale [83]. These spectral lines, if present in sufficient numbers and evenly distributed over the tuning range of the laser, serve as markers. But this is possible only near well-studied molecular bands, such as those of CO, CO_2, and N_2O. The most accurate variation is to perform heterodyne measurements in conjunction with an infrared molecular laser [87,97,98]. In this technique, spectrum analyzer is used to measure the beat frequency between the tunable laser and a gas laser with well-studied line positions such as a CO_2 or a CO laser. Accuracy as high as $10^{-4}cm^{-1}$ has been achieved. However, its applications have in the past been seriously limited by the requirement that the absorption lines usually have to be adjacent to a molecular laser line to $\pm$ 0.1 cm^{-1}. In the 10 μm region, CO_2 laser has been employed to the heterodyne technique. Lately, line position measurements within $\pm$ 6.5 GHz, near each CO_2 laser line, have been reported [97]. The use of HgCdTe varactor photodiode in the detection of beats up to 61 GHz has been developed with two CO_2 lasers [99]. This method has been applied to detect beats between a CO_2 laser

and a diode laser [98] and difference frequency up to 17 GHz has been observed. Also, a 54 GHz beat-note has been detected in an InSb hot-carrier diode mixer [100]. It is believed that these recent advances will significantly increase the applications of heterodyne technique.

The third approach is to rely on known molecular profiles to determine the tuning rate of the laser. Blum et al. [101] and Nill et al. [102] calibrated the tuning rate by measuring the magnetic field increment required to tune individual laser modes through the known Doppler widths of absorption lines of low-pressure gases. To apply this calibration method, care must be taken to insure that pressure broadening is negligible, that there is no fine structure of the absorption line which can add to its width, and that the absorption at line center can be accurately determined. The prior attempts [101,102] depended on the two-point calibration of the Doppler width of the absorption line and the assumption of a constant tuning rate over the region of interest. The uncertainty in the location of the half-maximum point on a sloping baseline plus experimental errors due to a typically noisy signal severely limit the accuracy. The calibration method to be developed in this research work is based on a much more sophisticated version of the third approach. It involves the fitting of the entire absorption line to a Voigt profile using the least-squares criterion. Reliability can be significantly increased as will be shown later.

D. The Use of Diode Lasers in the Monitoring of Gaseous Air Pollutants

The use of diode lasers in monitoring gaseous air pollutants includes the line-parameter study, which has shown to be important for the monitoring schemes [103], and also the analysis of pollutants.

As a basis for later atmospheric measurements, the study of line parameters of many pollutant gases in the infrared region has been made with various tunable IR lasers, mostly with diode lasers. While the line positions have been studied more extensively, the line intensities have been studied much less and absolute line intensities only in a few cases. McDowell [104] and Hinkley et al. [54] have summarized the results of previous research. Table 2 lists the works done before 1975 with various tunable infrared lasers [54]. Table 3 summarizes the works after 1975 with tunable diode lasers only [105-127].

The application of diode lasers in the analysis of gaseous air pollutants includes point sampling, in situ monitoring and long path monitoring. Each has its advantages and its particular usefulness. Their sensitivities are usually comparable with those of other methods or better.

Point sampling measurements can be made either at ambient pressure, or at reduced pressure for high specificity [128-131]. For the detection by the transmission technique, a multireflection long-path cell can be used to achieve a better sensitivity [37,132,133]. This has been done for source sampling, such as vehicle exhaust sampling and stack gas sampling, of ethylene and sulfur dioxide [37,134]. HCN, CH_4, C_2H_6 and water vapor in cigarette smoke have also been measured [129,131]. However,

Table 2. Molecular spectroscopy with tunable infrared lasers before 1975 [54]

Measurement	Molecule	Wavelength [μm]	Laser[a]
Absorption line spectra	HCl	1.2, 3.3	OPO, TDL
	HBr	1.9	OPO
	CO	2.4, 4.7	OPO, TDL
	CH_3F	3.4	ZTG
	C_2H_6	3.4	ZTG
	CH_4	3.4, 6.5	ZTG, TDL
	H_2CO	3.6	ZTG, TDL
	CO_2	4.2	TDL
	CS_2	4.6	TDL
	O_3	4.7	TDL
	NO	5.4	TDL, SFRL
	H_2O	5.3, 6.3	SFRL, TDL
	NO_2	6.2	TDL
	SO_2	8.7	TDL
	NH_3	8.7, 10.5, 11.8	TDL, SFRL
	C_2H_4	10.5	TDL
	SF_6	10.5	TDL, HPG
	C_2H_3Cl	10.5	TPM

[a]OPO: optical parametric oscillator

TDL: tunable diode laser

ZTG: Zeeman-tuned gas laser

SFRL: spin-flip Raman laser

HPG: high pressure gas laser

TPM: two-photon mixer

Table 2. (Continued)

Measurement	Molecule	Wavelength [μm]	Laser
Pressure broadening	CO	4.7	TDL
	H_2O	5.3	TDL
	SO_2	8.7	TDL
	NH_3	10.5	TDL
	CO_2	5.3	TPM
Collisional narrowing	H_2O	5.3	TDL
Nuclear hyperfine structure	CH_4	3.4	PTG
	NO	5.4	TDL
Lambda-doubling	NO	5.4	TDL, SFRL
Zeeman splitting	CH_4	3.4	PTG
	NO	5.4	TDL
	CH_4	3.4	ZTG
	H_2CO	3.4	ZTG
	HDCO	3.4	ZTG
Stark splitting	NH_2D	10.5	TDL
	CH_3Cl	10.6	TPM
	CH_3Br	10.6	TPM
Band analysis	SO_2	8.7	TDL
	SF_6	10.5	HPG, TDL
Laser gain lineshape	CO	5.3	TDL
	CO_2	10.6	TPM
Isotope lines	$C^{12.13}O^{16}$	4.2	TDL
	$N^{14.15}O^{16}$	5.4	TDL

Table 3. Line parameter study with tunable diode lasers after 1975

Molecule	λ (μm)	line intensity or abs. coeff.	line position	line width	pressure broadening	Band analysis spectrum	ref
HNO_3	11.3	x	x		x		41
H_2O	8.3				x		105
	10-15	x	x	x	x		106
H_2SO_4	8.3	x					107
	8.2,11.3					x	108
CH_4	7.9-8.3	x					94,109
CH_3F	8.4		x				110
	9-10					x	111
CH_3I	11.8		x				112
$CFCl_3$	11.6	x	x				113
CF_2Cl_2	10.8	x	x		x		113
CO_2	15	x		x	x		114,115
	16.2	x	x	x	x		116
$^{14}C^{16}O_2$	4.5	x	x				117,118
$^{12}C_2H_2$	13.7		x	x		x	119,120
$^{12}C^{13}CH_2$	13.7		x	x		x	119,120
$^{13}C_2H_2$	13.7		x	x		x	119,120
C_2D_4	4.5		x				121
ClO	11.8					x	122
NH_3	10.6		x				123,124
	8.3-12.5	x				x	125
	8.5-10.4					x	126
	8.4	x					127
	10.6	x				x	49
O_3	9.6		x				128
SF_6	10.5					x	122
SO_2	8.2						

the detection of ambient air sample may require very long optical paths because of the low concentrations of trace gases present in the air. It appears that the photoacoustic detection may suit this particular application better [135] (to be discussed later). Nevertheless, Reid et al. [132,133] have achieved a detection limit of less than 1 ppb for the ambient detection of SO_2, O_3, H_2O, CO_2, N_2O, NH_3 and PAN. And El-Sherbiny et al. [128] have demonstrated 0.5 ppb detection limit of ozone.

In situ monitoring performs the measurements in real time. It does not involve the taking of a sample for "off-line" analysis. This not only avoids the problems associated with sampling of reactive gases but also has the ability to measure the instantaneous changes of the interested gases. Both the vehicle exhaust monitoring (e.g. C_2H_4 monitoring) and stack gas monitoring (e.g. SO_2 monitoring) have been performed successfully by using tunable diode lasers [37,136].

Long-path atmospheric monitoring measures the total integrated pollutant concentration over the optical path which is important for regional modeling. It has the advantage of increasing sensitivity with range and the disadvantage of being double ended. Some works have been done in this application area [137-139] and concentrations of trace gases (e.g. SO_2, CO, NO, C_2H_4, H_2O) as low as ppb can be detected over pathlengths of hundreds meters to a few kilometers.

E. Techniques Applied to the Detection of Resonant Absorption

The applications of the diode laser in monitoring gaseous air pollutants are usually based on resonance absorption of laser radiation. The techniques for the detection of these resonance absorption signal can be divided into three classes: direct transmitted photon detection, photoacoustic detection and heterodyne detection. The heterodyne detection will not be reviewed here because it is not related to any subject of this research work. The other two will be discussed next with emphasis on photoacoustic detection, which is the subject of the fourth chapter.

1. Direct transmitted photon detection

This is the most commonly used detection method among the three. It involves direct conversion of incident photons to charge carriers by various detection device such as thermal detectors, photoconductive detectors and photovoltaic detectors. This detection technique has been used in all the three application areas mentioned above. It is not necessary to have high laser power to achieve high sensitivity because it is the difference between incident and transmitted power that is being measured. However, it is also this difference measurement scheme that limits the minimum detectable concentration of this detection technique.

Some efforts have been made to improve signal-to-noise ratio (S/N), and thus to lower the detection limit for the direct photon detection. Derivative techniques were the most studied ones. A small sinusoidal or a square waveform current was superimposed on the current ramp to

provide the wavelength modulation and thus to obtain the derivative spectrum. It was found that for long path monitoring this technique considerably reduced the noise caused by atmospheric turbulance and by scattering from aerosol. Ku et al. [138] have measured changes in transmission of 0.3% for pathlengths up to a few hundred meters at atmospheric pressure, using a derivative/ratio technique. A detection limit of carbon monoxide of 5 ppb over 0.61 km path has been obtained. This system was modified later by Chaney et al. [140] through the stabilization of laser frequency and the limitation of laser output to a single mode. Sensitivity variations of 0.7% were observed. Recently, Reid et al. [132,133] were able to detect absorption as small as 0.001% in a multipass cell of pathlength 100 meter at reduced gas pressure of around 10 torr, using a second-harmonic technique. This technique enabled them to measure absorption coefficients as low as $10^{-9}cm^{-1}$. SO_2 concentration was measured in the low ppb range and other gases having stronger IR absorption than SO_2(e.g. O_3, CO_2, NO, CO, CH_4, and NH_3) were measured down to much less than 1 ppb.

2. Photoacoustic detection

Photoacoustic spectroscopy (PAS) (also called optoacoustic spectroscopy) provides a highly sensitive method for the detection of molecules in the ambient air [141-143]. PAS detection instrument consisting of radiation source, modulator and acoustic detector (e.g. microphone) is often called spectrophone. The detected photoacoustic signal is proportional to both the power of the incident radiation and the concentration of the absorbing species. The high power lasers thus are preferred for

low detection limits (For the laser power information, refer to the introduction chapter).

Continuously tunable SFR laser has been used in conjunction with the photoacoustic spectroscopic technique to detect gaseous molecules to ppb level [135,144-146]. Kreuzer and Patel [135] detected NO in vehicle exhaust and ambient air samples to a detection limit of 10 ppb. Patel et al. [144,145] and Burkhardt et al. [146] launched a balloon-borne SFR laser-spectrophone detection system to monitor NO and H_2O in the stratosphere. The power of the SFR laser used in these system was in the order of 50 mW which was about two orders of magnitude of that of tunable diode lasers. In addition to the SFR lasers, the discretely tunable lasers such as He-Ne, CO, CO_2 and DF lasers, have been employed to detect a variety of pollutant gases for their operational simplicity and/or their higher power [147-155]. Because of the low power of the diode lasers, there has been only one study done on PAS technique with this type of lasers [152]. A detection limit of 50 ppm was achieved for carbon monoxide in nitrogen using a double-pass cell, with a 96 μW diode laser source.

The ultimate detectable PAS signal is limited by noise in the transducer preamplifier and noise caused by Brownian motion of the molecules [153,154]. In addition to these two sources of noise, there are background signals in a PAS cell due to window absorption and absorption in the wings of spectral lines of other species. Moreover, there may be noise in the measured data due to laser power fluctuations and amplifier gain variations. These background signals are the major

limitation upon the ability of the PAS technique to detect very weak absorptions. Some attempts have been made to reduce the background signal due to window absorption. They include (a) the use of a resonant cell with light beam chopped at a certain rate to produce the natural acoustic modes within the cell, and nodes near the windows [149-150, 155-157]; (b) the use of a differential system consisting of two cells in series, with a common window [151]; and (c) the modulation of either the laser frequency or the spectral frequency of the absorption line to be monitored by Stark or Zeeman effect [158-160]. Besides, the PAS signal can be enhanced by use of a multipass cell [150,161]. A comprehensive treatment of the entire subject of PAS detector design and evaluation has been published by Rosengren [154], and a comparison of resonant vs. nonresonant spectrophones has been prepared by Dewey [162].

A differential cell consists of two chambers placed end to end with a bore in between and a window on the bore. The balanced window heating in the two cells reduces the background signal. Absorption measurements are made by filling one chamber with a test gas mixture (with a nonabsorbing gas), and the second chamber the nonabsorbing gas only. The pressure difference between the two cells then is measured. This differential signal represents the absorption coefficient of the test gas. Using a differential spectrophone operating at 1-Hz chopping frequency, and integration time to 2 minutes, Deaton et al. [151] reduced the background signal to a value which corresponds to $3.3 \times 10^{-9} cm^{-1}$ per watt of laser power. This development permits not only the detection of gases such as ethylene in concentrations approaching 0.02 ppb with fixed-frequency gas lasers, but also the use of lower power tunable semi-

conductor diode laser for PAS detection in the low ppb level.

Stark and Zeeman modulation can also be used to reduce the PAS background signal. In these modulation modes, the radiation beam is not chopped by mechanical chopper but modulated by Stark or Zeeman effect (i.e. the spectral line of the absorbing species is shifted in and out of the laser frequency by applying an electric or magnetic field onto the species respectively.) These techniques provide a new degree of discrimination between molecules whose absorption spectra overlap but exhibit different Stark or Zeeman effect. Discrimination will also be enhanced between signals due to near-resonant weak absorptions and signals due to the wings of a strong absorption line. Since the laser beam is incident on the cell consistently and unmodulated, the window surface absorption should be constant with the laser intensity and therefore will not contribute to the detected signal with the phase-sensitive detection devices. Both the acoustical noise and the photon scattering due to the mechanical chopper will also be eliminated because no chopper is used in this technique. Bonczyk and Ultee [158] and Kaldor et al. [159] used a magnetic field to Zeeman-modulate the frequency of an NO transition and detection limit of a few ppm was obtained. Kavaya et al. [163] investigated the use of Stark modulation for PAS detection. Results showed that the background signal obtained by operating in this mode is 500 times less than that obtained by operating the same PAS detector in the conventional chopped radiation mode. The S/N was found greater in the Stark mode than in the chopped mode for pressures below 500 torr. The minimum detectable absorption strength was $1 \times 10^{-7} cm^{-1}$ per watt of laser power. If a continuous tunable laser is employed,

one can eliminate PAS background signal effectively by wavelength modulation of the radiation source. Because window surface absorption is independent of wavelength, no ac signal would be produced and detected if the source intensity is constant. Dewey [164] developed a simple theoretical model for wavelength modulation in PAS technique including derivative spectroscopy and wide modulation spectroscopy. Patel et al. [144] have demonstrated the usefulness of the latter in which the wavelength was substantially modulated relative to the center of the gas absorption line. Derivative spectroscopy, on the other hand, will be the subject of the fourth chapter of this thesis.

The acoustically resonant cell was first introduced by Dewey [149] and has been studied quite extensively since then. It not only accumulates acoustic energy in a standing wave to amplify the pressure signal, but also reduces the window absorption background signal by locating the acoustic nodes on the windows. Moreover, it provides a means for the continuous monitoring of the air sample (to be explained later). Kritchman et al. [166] analyzed the ultimate detectivity of ideal PAS cell and gave rigorous mathematical expressions for both signal and noise for a one-dimensional cell. They also constructed a longitudinal resonant cell and found minimum detectable concentration of ethylene in nitrogen as low as 0.3 ppb per watt of CO_2 laser power for 1-Hz detection bandwidth. The multipass resonant cylindrical cell is judged as one of the most promising designs for practical applications [150,165] and is expected to have a detection limit of sub-part-per-billion per watt of laser power. Since the PAS signal is proportional to the beam power, it is a natural extension to place the cell inside the

laser optical cavity to result in multipass in the cell and at the same time to take advantage of the higher laser power in the cavity. Shtrikman and Slatkine [161] did this with a CO_2 laser and resonant spectrophone and reported an improvement of sensitivity. Their system could operate in two modes: with windows or without windows. The windowless spectrophone permits continuous sampling, which would be desirable for ambient air monitoring, by introducing a slow flow of air through the cell, Absence of windows solves power loss problem due to the window reflection, yet it can greatly degrade the resonant quality of the cell. Thus, a cell with acoustic nodes on its ends, in which the holes will constitute a minimal perturbation, is necessary. Nevertheless, the sensitivity of the windowless system is still worse than that of the system with windows on the cell. Shtrikman's windowless system was reported to have detection limit below 10^{-7} cm^{-1} for 1-Hz bandwidth detection and was expected to reach $3 \times 10^{-10} cm^{-1}$ by the reduction of the laser internal losses. Recently, another intracavity resonant spectrophone was used in conjunction with a DF laser of subwatt power and showed a detection limit of $7 \times 10^{-9} cm^{-1}$ for S/N of 1 [167]. However, it is noteworthy to mention that the gain on S/N by using the resonant cell is usually not as great as it may seem. First of all, the volume of a resonant cell is considerably greater in general than that of a nonresonant cell. Thus, it requires more energy to heat up the same concentration of gases in order to obtain the same amount of pressure change. Secondly, the PAS signal intensity is proportional to 1/f where f is the modulation frequency of the laser beam. With the typical size of a resonant cell, the natural acoustic resonant frequency is

usually over 1 KHz while the nonresonant cell can use a frequency of only a few Hz to retain its highest obtainable signal. As a matter of fact, the most sensitive measurement reported to date was done with a carefully designed nonresonant cell employing six miniature microphones [168]. Its minimum detectable absorption was 10^{-10} cm^{-1} per watt of laser power.

In view of the information reviewed here, we decided to tackle two of the existing problems associated with the use of tunable diode lasers in the analysis of gaseous air pollutants. The first one is the calibration of diode laser scan rate. An internal calibration scheme is developed based on the third approach of calibration methods, as discussed earlier. The linewidths, line positions and other line parameters can then be determined through this calibration scheme. The new internal calibration method is much more reliable than the old one and is simple enough to be performed on a daily basis. The second one is to apply the photoacoustic spectroscopy to the detection of gaseous air pollutants by the use of tunable diode lasers. Since the photoacoustic sensitivity is proportional to the power of light source employed, the use of diode lasers in this detection technique presents a challenge. Ammonia was chosen here as sample gas because of its importance in the air pollution. The details of these two sets of experiments will be discussed in the following two chapters.

III. INFRARED LINEWIDTH AND LINE POSITION MEASUREMENTS BY INTERNAL CALIBRATION METHOD

A. Background and Theory

There are three fundamental properties of an isolated spectral line. They are its center wavelength, intensity and shape. The tunable infrared laser technology has made very little impact on the absolute wavelength calibration, but it offers the capabilities of direct measurements of line intensity and line shape. The key to these is the laser's narrow linewidth and tunability.

In the research work presented in this chapter, the line shape was used as a tool for calibrating the tuning rate of tunable diode lasers. If a proper reference standard can be found, the absolute frequency of the line of interest can then be obtained. This internal calibration scheme also has found its use in the study of pressure broadening effect. In addition, if desirable, the absolute line intensity can also be obtained from line parameters derived from line shape studies. In the following few pages the principles of this internal calibration scheme will be presented in detail.

The spectral line shapes can be divided into two categories: homogeneous line shape and inhomogeneous line shape. Inhomogeneous line shape is caused by inhomogeneous broadening. This type of broadening permits different molecules undergoing the same nominal transition to absorb radiation corresponding to this transition at slightly different frequencies due to the small differences in the environment of each

molecule. The most familiar example of this type of broadening mechanism is Doppler broadening which is caused by the thermal motion of the molecules. The molecules emitting light of frequency ν may move towards or away from the observer with velocity v. According to the Doppler effect, the radiation frequencies received by the observer then are different in each case as ($\nu + d\nu$) and ($\nu - d\nu$) respectively, where $d\nu = \nu(1 - \frac{v}{c})$ (c is the speed of light in vacuum). With molecules moving in all directions and various velocities, the observed line shape is therefore broadened and has the shape of a probability distribution curve, that is, Gaussian shape:

$$k(\nu) = \frac{2S(\ln 2)^{\frac{1}{2}}}{\pi^{\frac{1}{2}}\Delta\nu_D} \quad \text{Exp} \left[- \frac{4(\nu - \nu_o)^2 \ln 2}{(\Delta\nu_D)^2} \right] \tag{3.1}$$

where S is the integrated intensity, ν_o is the center frequency, $k(\nu)$ is the absorption coefficient at frequency ν and $\Delta\nu_D$ is the Doppler line width (full width at half maximum (FWHM)). $\Delta\nu_D$ is given by the expression

$$\Delta\nu_D = 7.162 \times 10^{-7} \nu_o \sqrt{T/M} \text{ cm}^{-1} \tag{3.2}$$

where T is the absolute temperature and M is the molecular weight.

On the other hand, the broadening mechanism, which permits each molecule to absorb radiation over the entire line width, is known as homogeneous broadening. This type of broadening is characteristic of any system with an exponentially decaying dipole correlation function, such as natural broadening, saturation broadening, and collision broadening. Therefore, it is really a reflection of the Heisenberg uncertainty principle. The decay process prevents the molecule from remaining in a specified energy state for a period longer than Δt, where Δt is the

lifetime of the molecular decay process, and the line width is $1/\Delta t$. In the natural broadening, the natural linewidth exists because any molecule in its excited state has finite lifetime, which leads to an uncertainty in the energy level of the excited state as required by the uncertainty principle. Thus, the frequency ν_o for a transition between levels E_i and E_j is no longer given uniquely by $\nu_o = (E_i - E_j)/h$ and the line has a finite width.

A homogeneous spectral line always has a Lorentzian shape. As for the collision broadening, it is given by the expression

$$k(\nu) = \frac{S}{2\pi} \frac{\Delta\nu_L}{(\nu - \nu_o)^2 + (\Delta\nu_L/2)^2} \tag{3.3}$$

where $\Delta\nu_L$ is the Lorentzian broadening linewidth (FWHM). $k(\nu)$, S, and ν_o are as before.

Collision broadening (also called pressure broadening) is caused by the intermolecular collisions of the gas molecules. The foreign-gas broadening is usually much less than self-broadening. The relationships between the Lorentzian width and the collisions which cause it are complex. More detailed treatment of this subject can be found in some monographs [169].

The value of various types of linewidths depends on the contributing broadening mechanisms. Natural linewidth is the ultimate linewidth of any spectral line. In the infrared range, the natural linewidth is usually in the order of 10^{-5} to 10^{-6} cm^{-1}. At low pressures (a few torrs), Doppler effect dominates the line broadening mechanisms and the linewidth is generally determined by the Doppler width which has a typical value of 10^{-3} cm^{-1}. When the pressure is increased, the line shape and linewidth

are no longer solely determined by Doppler effect, but are also affected by pressure broadening which eventually becomes a dominant factor at higher pressures (e.g. a few tens of torrs). The pressure broadening linewidth increases with increased gas pressure and is dependent upon temperature and nature of the gas. At the pressure of 1 atm, it typically ranges from 0.5 cm^{-1} to 0.05 cm^{-1}. At intermediate gas pressures, neither Doppler broadening nor pressure broadening dominates. The line shape is represented by Voigt profile [170] which is formed by the convolution of Gaussian and Lorentzian line shapes. Some spectra have been measured in this regime, but no careful studies using tunable lasers have been made. The Voigt profile is very complex and cannot be evaluated in closed form. However, some approximate forms have been studied and detailed numerical tables have been given [171].

Some mathematical procedures for approximating Voigt profile have also been investigated. In this research work, an efficient procedure proposed by Kielkopf [172] was adopted to generate the Voigt profile. When the Doppler width totally dominated at low gas pressure, the Lorentzian width could be assumed to be negligible when compared to the Doppler width. The experimental Doppler width then was determined by least-squares method through successive fitting to the Voigt profile. The same principle can be applied to the determination of Lorentzian width when both pressure broadening and Doppler broadening contribute to the spectral linewidth at intermediate pressure. Here, the experimentally determined Doppler width cannot be assumed to be negligible when compared to the Lorentzian width. Since the Doppler width can be calculated with sufficient accuracy with equation 3.2, the experimental Doppler width then was taken to fit

the calculated Doppler width to obtain the tuning rate of the diode laser. After the tuning rate was obtained, it was used to calibrate the pressure broadening linewidth and thus enabled us to study the pressure broadening coefficient introduced by self-broadening and/or foreign-gas-broadening. In addition, it also enabled us to calculate the absolute frequency of the line center if a reference standard frequency was available.

B. Experimental

1. Experimental components

The components used in this work are summarized in Table 4. The details of some important components are given as follows.

a. Vacuum and gas transfer system The schematic diagram of vacuum and gas transfer system used in this work is shown in Figure 5. In order to hold liquid helium to a reasonable amount of time, the cryostat must be pumped down to at least as low as 10^{-5} torr prior to a run. The pumping process was accomplished in two steps, first with a mechanical pump, and followed with an oil diffusion pump. The pressure of the system was measured with an ion gauge located between diffusion pump and cold trap. The system was designed so that during the second pumping stage the oil diffusion pump kept pumping the cryostat while the rest of the vacuum line (separated by valve V1) can be used for gas transfer.

Prior to the transfer of gas into the gas cell, the gas transfer system was pumped down with the mechanical pump A, then valve V2 was closed to stop pumping. Gas samples were introduced from gas inlets A, B, or C. The gas pressure could be measured with a mercury manometer shown on the left side of Figure 5 or capacitance manometers attached on the gas cell.

Table 4. Experimental components for the study of internal calibration

Component	Model No.	Manufacturer
Cryostat	0-2-250 +0-7M-H	Andonian, Waltham, MA.
Diode laser package A	TDL	Arthur D. Little, Cambridge, MA.
Diode laser package B	SDL-30	Laser Analytics, Bedford, MA.
Power supply for diode laser	------	Home made
Regulated DC power supply	6226B	Hewlett-Packard, Santa Clara, CA.
Monochromator	E-1	Perkin Elmer, Norwalk, CT.
Tuning fork	L2C	Bulova, Woodside, NY.
HgCdTe detector	DMSL 45	Infrared Associates, New Brunswick, NJ.
Lock-in amplifier	9503	Ortec, Oakridge, TN.
A/D converter	ADC-ER12B	DATEL, Mansfield, MA.
Paper tape punch	3444	Digital Product, San Pedro, CA.
X-Y recorder	7001A	Moseley, San Diego, CA.
Capacitance manometer	221	MKS Instruments, Burlington, MA.

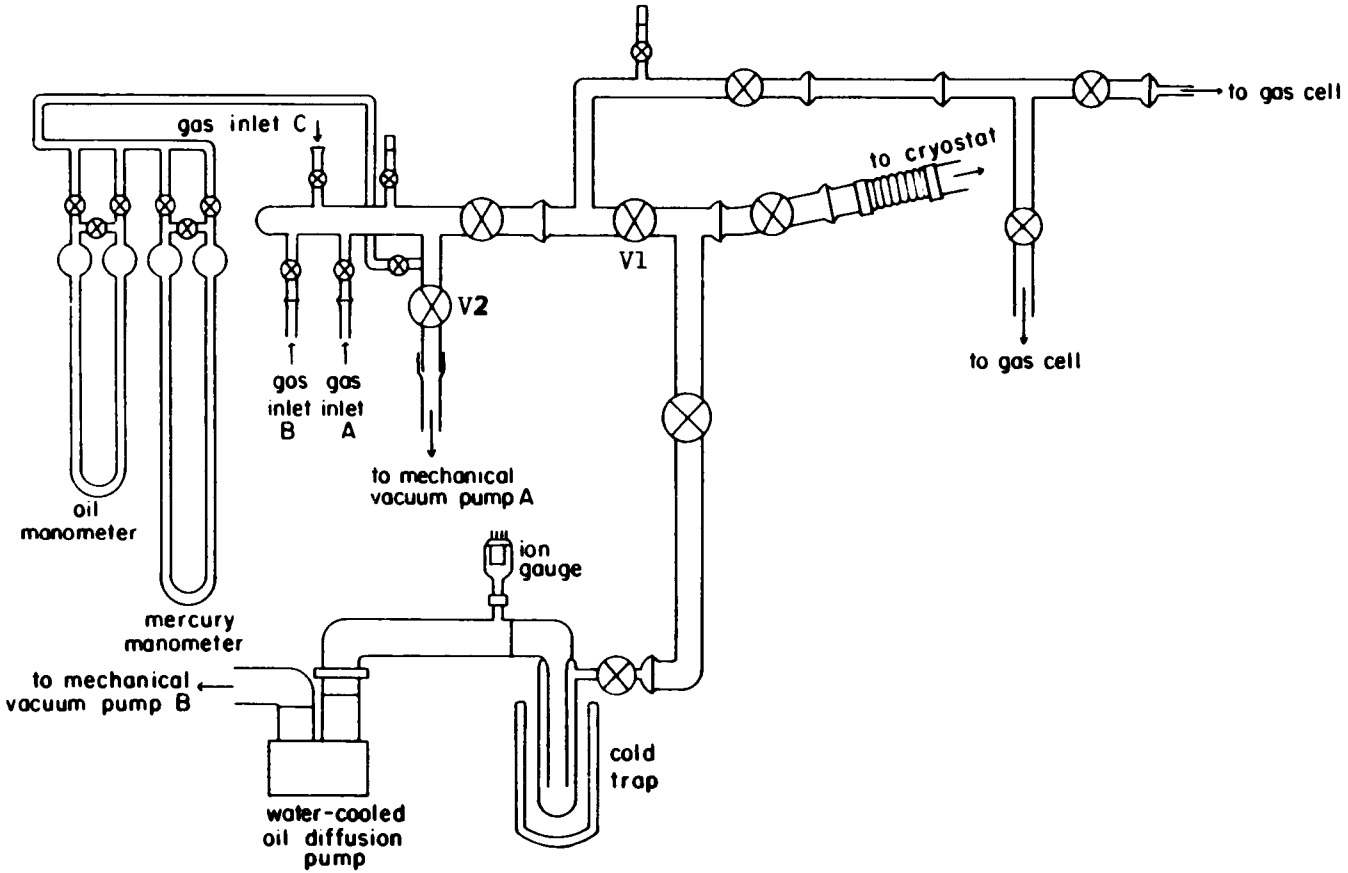

Figure 5. Vacuum and gas transfer system.

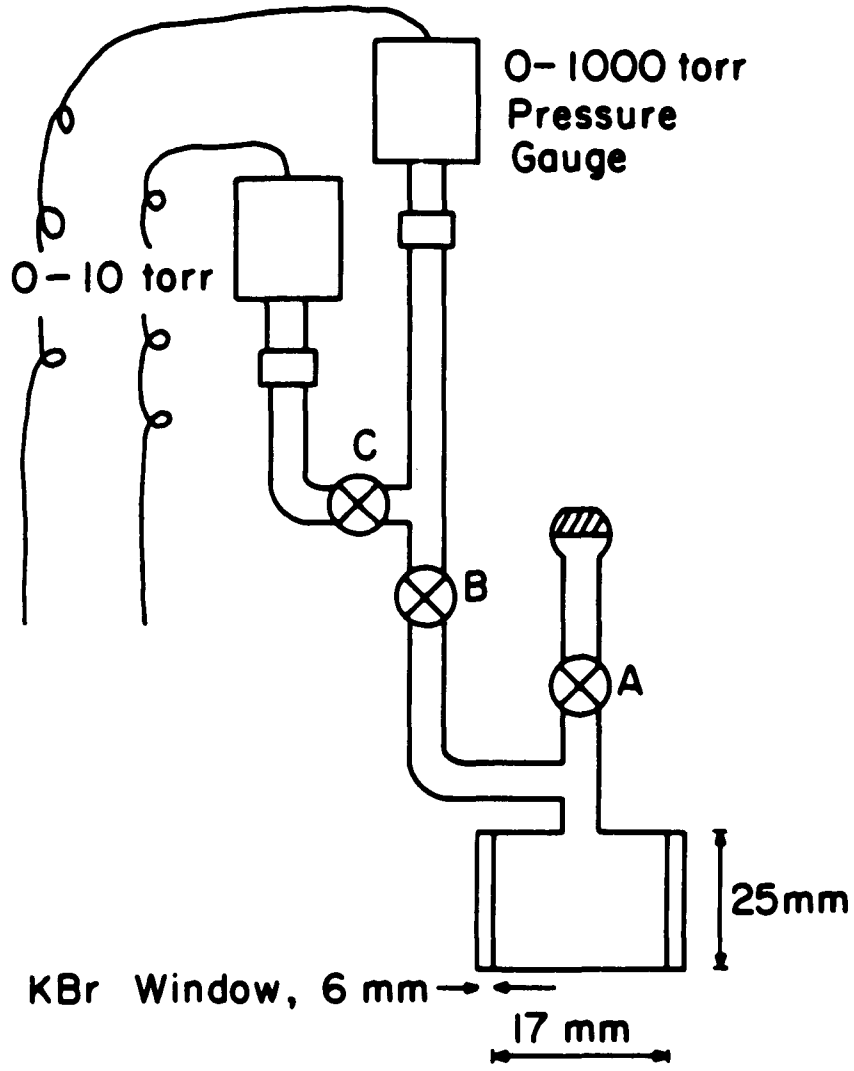

Figure 6. The design of gas cell used in the study of pressure broadening of NH_3.

The gas cell (Figure 6) was designed so that two capacitance manometers can be mounted, one for low pressure ($\leq$ 10 torr) and the other for higher pressure ($\leq$ 1000 torr). It was imperative to have the manometers attached as close to the cell as possible to ensure the accurate measurements of sample pressures. After the cell was filled with gas sample, valve A was closed. Before taking the spectrum, the sample was allowed to sit for 10 minutes to reach equilibrium.

b. Components of laser system

1) Laser package The heart of a diode laser spectrometer is the tunable diode laser crystal. The commercially available laser crystals are usually mounted in packages. Two different laser packages, as shown in Figure 7, have been purchased from two manufacturers. The laser package A has both the top contact and base contact made of brass. A ceramic spacer is placed in the center of the package to separate the contacts. One laser contact is made directly to the base contact with a cold solder joint and the other laser contact is a cold soldered gold wire which extends from the laser to the top contact. Electrical contact to the laser is made with negative lead attached to the top. The laser package was mounted to the heat sink with a set screw. The laser package B is made of gold coated copper. It is specially designed to provide bilateral heat flow from both contact regions of the laser crystal. It can be easily mounted to a heat sink by using its two mounting holes shown in Figure 7. The top contact is attached to the negative lead of the current supply and the base contact to the positive lead as in the package A.

The cooling of the laser is by thermal conductivity through the base. Any design for holding this package onto the cold head of the cryogenic

Figure 7. Laser packages used in this work. A is manufactured by Arthur D. Little. B is manufactured by Laser Analytics. All dimensions are in inches.

Laser package A:

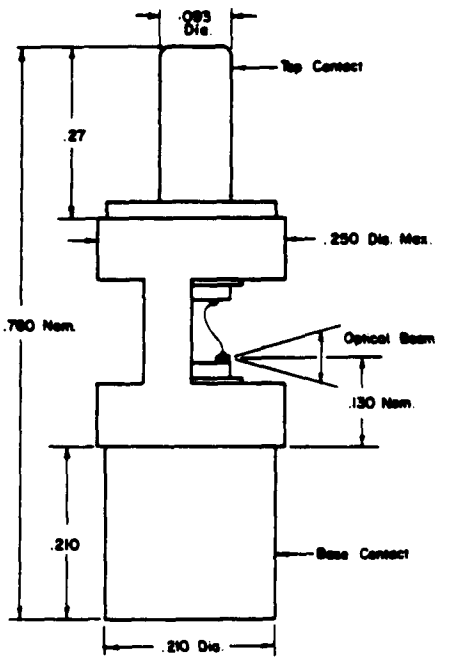

Laser package B:

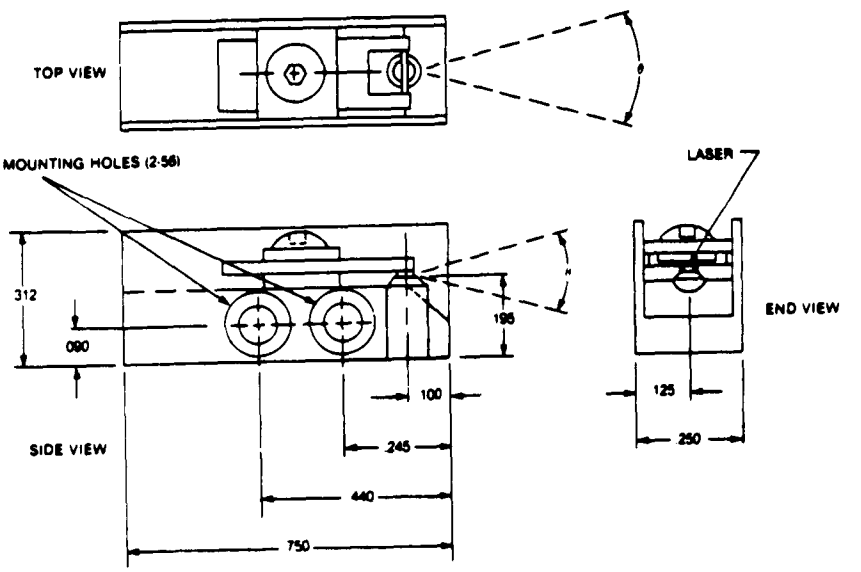

system must be of excellent contact to reduce electrical and thermal resistance. The laser package mount, also serving as a heat sink, must have a mass big enough to ensure a stable temperature of the laser crystal.

2) Cryostat and laser mount The cryostat used to mount and cool down the diode laser is a commercial cryostat manufactured by Andonian, as shown in Figure 8. Two types of laser-package mounts, also shown in Figure 8, have been designed to hold the two different laser packages. Both mounts are made of oxygen-free copper and the packages are hold in place with set screws. The mounts then are bolted to the cold head of the cryostat with an indium gasket between the two to ensure good thermal contact. The cryostat is facilitated with a 20-ohm heater around the cold head to provide temperature variation when needed. The throttle valve on the cryostat enables us to adjust liquid helium flow rate to the cold head, which in turn controls the laser temperature. The front window of the cryostat is a BaF_2 flat which is chosen because of the low solubility of BaF_2 in atmospheric moisture. The rear window is merely a piece of flat pyrex glass. The cryostat and laser were usually cooled down to liquid nitrogen temperature the day before and subsequently cooled to liquid helium temperature immediately prior to a run. Detailed procedures are described in Appendix A.

3) Laser current supply The regulated laser current supply (Figure 9) is a modification of a previous design [173]. The operational procedure is also described in Appendix A.

The circuit at the bottom of Figure 9 is a voltage ramp generator. The ramp time is made variable from about five seconds to eighteen minutes with the variable resistors in the circuit. The voltage ramp generated

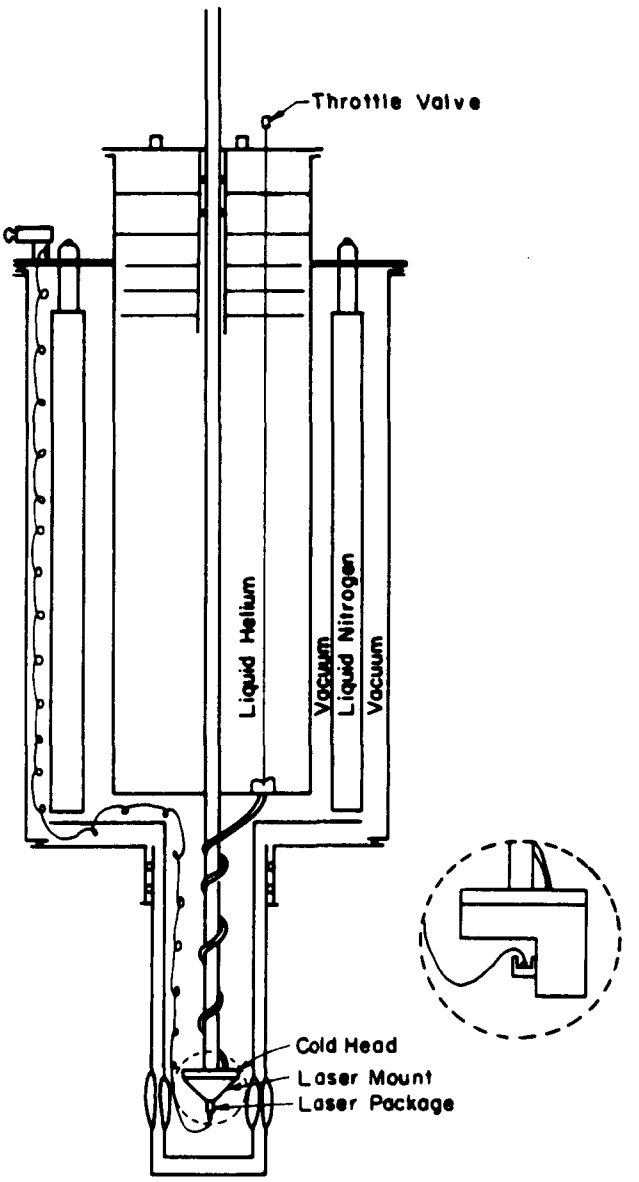

Figure 8. Liquid helium cryostat and laser mounts.

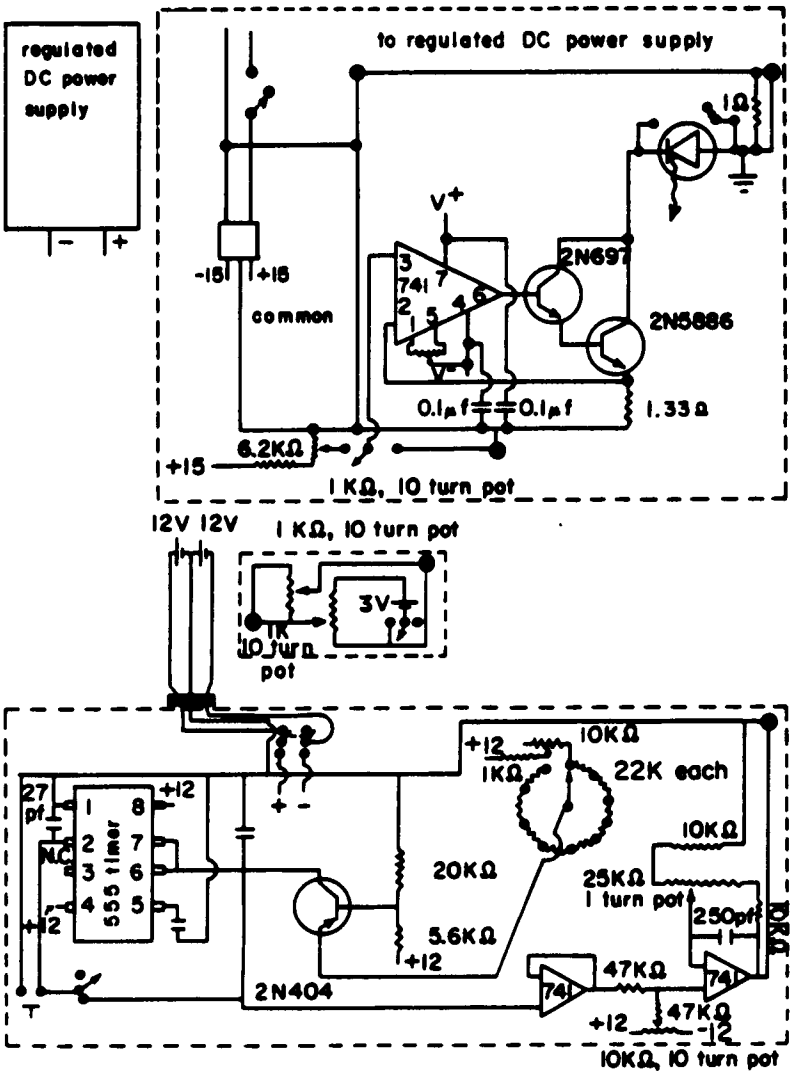

Figure 9. Power supply system for the tunable semiconductor diode laser.

from this circuit is fed into a DC offset circuit (in the center of Figure 9) which contains two voltage dividers. The first one provides any voltage from 0 to 3 volts. The second voltage divider adds the voltage ramp from the ramp generator to the voltage provided by the first voltage divider circuit. The voltage ramp coming out of the DC offset circuit then is sent into the circuit, shown at the top of Figure 9, which provides the current for the semiconductor diode laser.

2. Diode laser spectrometer setup for conventional IR spectroscopy

The diode laser spectrometer used in this work is of conventional design as shown in Figure 10. Its operational procedures are also included in Appendix A. Laser crystals of stripe geometry of the type $Pb_{1-x}Sn_xSe$ were used. Cooling was provided by a liquid helium cryostat (Figure 8) and a temperature of about 4 K was used throughout. Radiation from the laser was collected by a BaF_2 lens of 63.5 mm diameter and 76 mm focal length and was collimated onto a gold coated concave mirror of 108 mm diameter and 550 mm focal length. The mirror focused the radiation at the entrance slit (12 mm x 0.2 mm) of an infrared monochromator operating in the double pass mode at a dispersion of 0.97 cm^{-1}/mm. The slit width was set at 200 μ to 300 μ depending upon the mode pattern. The mode center was read from the monochromater. A Bulova tuning fork light chopper with 1/2 inch by 1/4 inch vanes was placed adjacent to the slit to modulate the radiation at 1 KHz. A gas cell, 2.5 cm diameter and 2 cm long, fitted with KBr windows was placed at the exit slit of the monochromator. The laser radiation was collected after the gas cell and focused by a NaCl lens of 35 mm diameter and 70 mm focal length onto a photoconductive HgCdTe infrared detector. The reference signal from the chopper and the signal

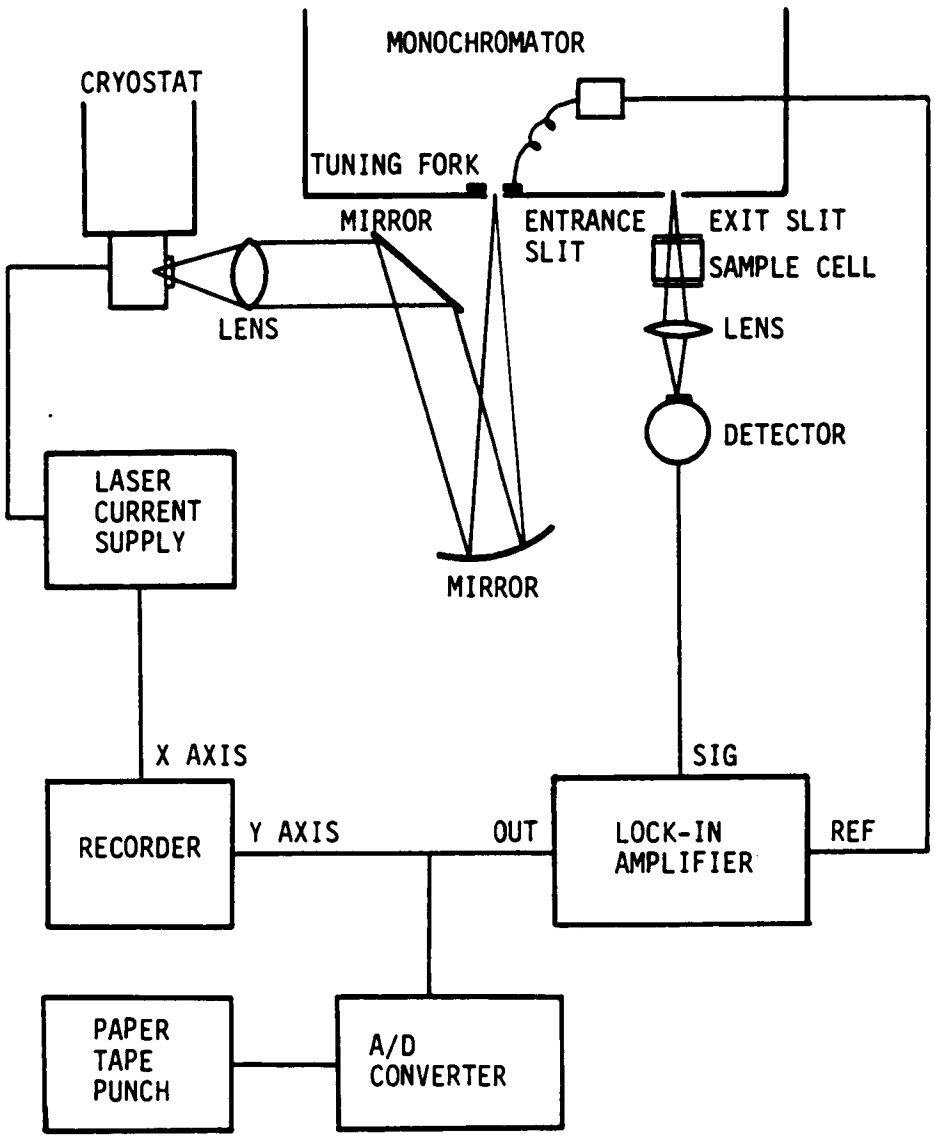

Figure 10. Diode laser spectrometer setup for conventional IR spectroscopy.

from the detector were analyzed by a lock-in amplifier. The laser was powered by a current ramp, which also controlled the x-axis of an X-Y recorder. The Y-axis then displayed the laser intensity as registered on the lock-in amplifier.

To handle the large amount of data generated, the output from the lock-in amplifier was simultaneously digitized by an A/D converter at 1 second interval during the laser scan, and recorded by a paper-tape punch for eventual computer analysis. Since the internal calibration scheme was used here, it was not necessary to determine the exact current ramp, as long as the same ramp was used throughout. The intensity data taken every second established an arbitrary horizontal scale. The zero intensity level was recorded at the end of each laser scan by blocking the laser beam.

Reagent grade gases (Scientific Gas Product, S. Plainfield, NJ) were used without further purification. Pressures were determined by factory calibrated capacitance manometers. Data analysis was performed on a CDC 7600 computer of Lawrence Laboratory facility (Berkeley, CA) and digitized spectra were plotted on a National Advanced System AS/6 computer (National Advanced System, Mountain View, CA) and IBM 1627 plotter (IBM, White Plain, NY).

3. Data analysis

The digitized data punched on paper tape were read off with a computer program by the AS/6 computer and plotted by the IBM 1627 plotter. The data then were analyzed by the CDC 7600 computer with a second program to obtain the linewidths and other line parameters of the best-fit Voigt profile. The so-obtained parameters were taken to the AS/6 computer and the plotter again for the plotting of both the best-fit Voigt profile and the experi-

mental spectrum with a third program for easy comparison of their agreement. The three computer programs are listed in Appendix B.

To analyze the spectrum, the laser intensity, the transmitted intensity (I) and the zero intensity line (which was generated by blocking laser beam) were required. Since the laser intensity was not uniform over the scan, it was necessary to generate a reference intensity level in the region of the absorption line by a polynomial best-fit covering the points immediately adjacent to the absorption line. The actual absorption profile was then determined by normalizing the transmitted intensity (I) of each experimental point to this reference intensity (I_o). Normalized Voigt profile (in transmittance) were generated by an efficient mathematical procedure [172] for a number of trial values of line center (ν_o), Doppler width ($\Delta\nu_D$) and Lorentzian width ($\Delta\nu_L$). To provide for errors in determining the transmittance at the absorption peak, that value was also varied in the trials. The generated Voigt profiles were then compared to the experimental profiles point by point. Best-fit was determined by the least-squared deviation summed over all experimental points.

C. Results and Discussion

1. Pressure broadening of NH_3

The internal calibration scheme is ideally suited for linewidth measurements since the scan rate (tuning rate) at the exact position of the spectral line can be accurately measured. NH_3 is an important air pollutant and makes an interesting case because of its low molecular weight and large collisional cross section, both of which lead to substantial pressure broadening. So there has been a number of theoretical [174,175] and experi-

mental [54,125] studies on this subject as expected.

NH_3 line aP (4,2) at 852.75 cm^{-1} was chosen for a demonstration of the simplicity and reliability of this internal calibration on its application to the pressure broadening study because it is a well isolated spectral line and has a reasonably strong absorption. Both self-broadening and nitrogen-broadening of this line were studied. All the data were taken in the same day to reduce the variation of laser frequency and tuning rate due to the temperature cycling and instability of the laser. The results of the study as well as the identification of the NH_3 line are presented as follows.

a. Identification of NH_3 line The NH_3 line was easily identified as aP (4,2) at 852.75 cm^{-1} by comparison of monochromator setting and literature values of peak positions [175]. This line was the only one in the mode of 852.82 cm^{-1} which was read from a calibrated monochromator operating at a spectral width of 0.3 cm^{-1}. According to literature [175], the line positions adjacent to this value with reasonably strong absorption were 851.34, 852.75 and 853.58 cm^{-1}. The aP (4,2) line could thus be unmistakenly identified.

b. Self-broadening of NH_3 Self-broadening spectra were taken with various NH_3 pressures in a random order to avoid systematic errors. In order to assure significant absorption for spectral fitting, the lowest pressure used was 0.55 torr, which was expected to be low enough to show "pure" Doppler width [54] (It was found out later to have nonnegligible Lorentzian width). The highest pressure used was 3.05 torr, above which the absorption line was saturated.

Under the assumption that Lorentzian width was negligible at pressures

up to 0.75 torr, the experimental Doppler half-width was obtained by the above described process for data analysis. However, it was noted that the fitting was not good (first approximation). The so-obtained Doppler half-width then was used to calculate Lorentzian half-widths at higher pressures. Surprisingly, the plot of NH_3 pressure vs. Lorentzian half-width (HWHM) showed that the best-fit line of the experimental data to the linear equation $Y = aX + b$ was not passing the neighborhood of the origin as it should if the above assumption is valid. Instead, this best-fit line intercepted the Y axis at a negative value (See Appendix C for the calculation of a least-squares fitting line and the standard deviation of its slope). This was an indication of the existence of Lorentzian half-width at low pressures ($\leq$ 0.75 torr) and that the experimental half-width (assumed to be purely Doppler) actually have nonnegligible contribution from the Lorentzian width. This explains the poor fitting of experimental line shape to Voigt profile. Fortunately, the Doppler half-width could be derived from the best-fit Voigt profile independent of the Lorentzian half-widths, and accurate calibration was still possible. However, the utilization of an approximation approach was necessary in order to efficiently extract the true Doppler half-width. The slope of the best-fit line for the plot of NH_3 pressure vs. Lorentzian half-widths (i.e. the pressure broadening coefficient) from the first approximation was used to calculate Lorentzian half-widths which in turn were used in the Voigt profile to obtain Doppler half-widths of the second approximation at low pressures. The second-approximation Lorentzian half-widths were calculated from these second-approximation Doppler half-widths, they were then used to obtain second-approximation pressure broadening coefficient. The same procedure

was repeated until the difference between the slopes of two successive approximations was less than the uncertainty of the slopes. The Doppler half-widths of the fourth approximation calculated for the six NH_3 pressures between 0.55 torr and 0.75 torr were in good agreement to each other with a standard deviation of ± 1.0 MHz. This value was higher than the estimated accuracy of the individual fitting (± 0.3 MHz). Possible reasons for this would be the errors introduced by the approximation approach and the minor variation of the diode temperature.

For the scan rate calibration, only those scans with low NH_3 pressures were used since the spectral fitting is less sensitive to the Doppler component at high pressures, and thus the reliability deteriorates. The same scan rate was assumed for the studies at higher pressures which were all performed in rapid succession. All the half-widths obtained from the fitting to Voigt profile were of the same arbitrary unit and were calibrated with the true Doppler width which is 76.525 MHz calculated from equation 3.2 with $T = 297.1^{o}K$, $M = 17.03$ gram and $\nu_o = 852.75\ cm^{-1}$. At this point, one should realize that the Doppler width obtained by this Voigt profile generating procedure [172] is not the true Doppler width, but a factor of $1/\sqrt{\ln 2}$ of that value.

Figure 11 shows the excellent fitting of experimental spectral lines to Voigt profile at various pressures. The results of the fourth approximation are tabulated in Table 5 and are used to obtain Figure 12 where the Lorentzian half-width is plotted as a function of NH_3 pressure. It can be seen that the best-fit line passes the origin. The least-squares fit to the points in Figure 12 gives a self-broadening coefficient (full width) of 26.2 ± 0.4 MHz/torr and a correlation coefficient of 0.9981. This is

Figure 11. Computer plotted spectra of self-broadening of NH_3 line at 852.7 cm^{-1}. + represents experimental data. Solid lines over experimental data represent best-fit Voigt profiles. Solid lines under the NH_3 peaks represent 4th degree polynomial best-fit base lines.

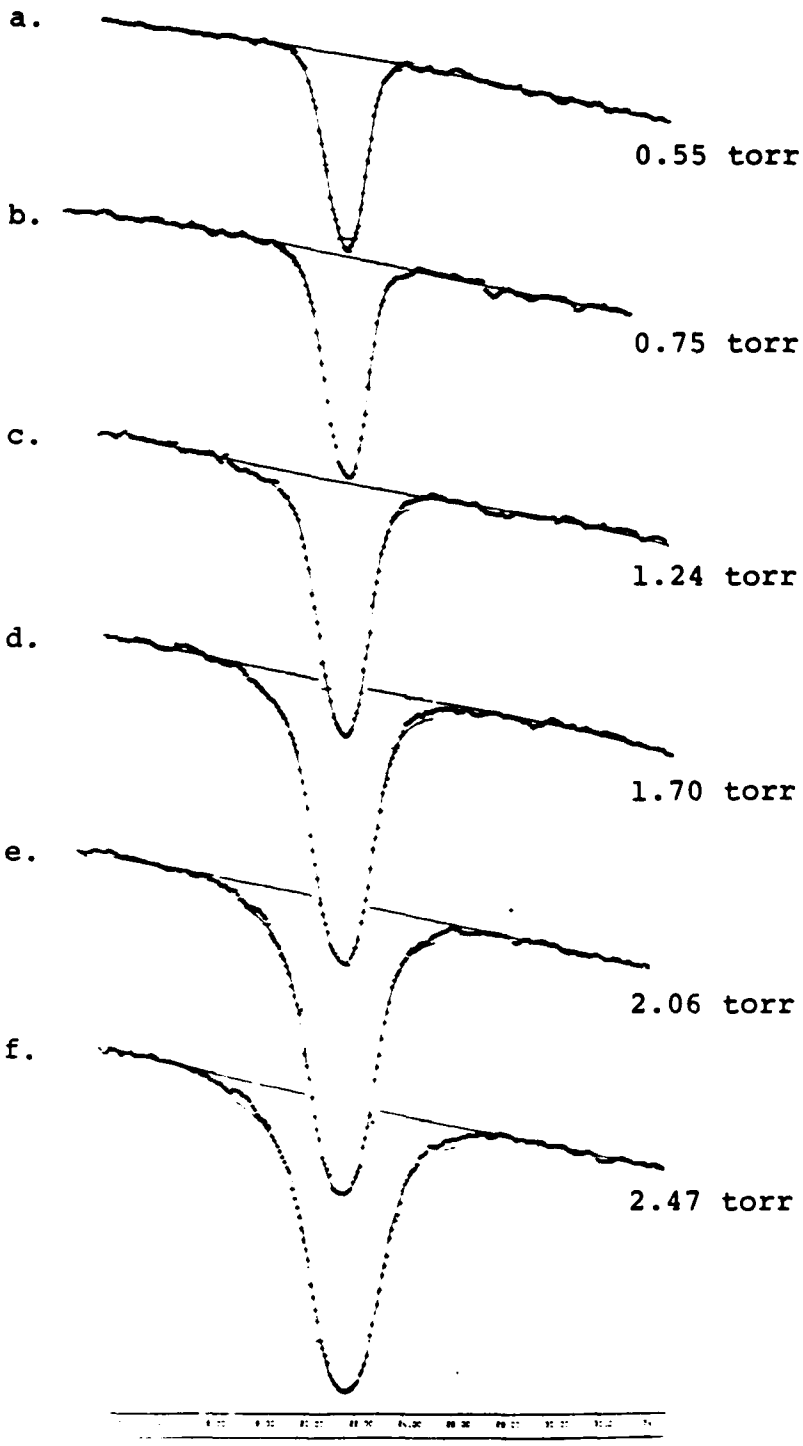
a.
0.55 torr
b.
0.75 torr
c.
1.24 torr
d.
1.70 torr
e.
2.06 torr
f.
2.47 torr

Table 5. Spectral data of self-broadened NH_3 line at 852.7 cm^{-1}

P_{NH_3} [a]	A [b]	W_D [c]	W_L [d]	Least-Squared Deviation
.550	.434	46.727	7.27	8.871×10^{-5}
.611	.514	46.713	8.08	9.607×10^{-4}
.606	.445	45.306	8.01	6.647×10^{-5}
.614	.467	45.898	8.12	8.815×10^{-5}
.729	.544	45.672	9.64	9.911×10^{-5}
.754	.557	45.430	9.97	6.020×10^{-5}
.893	.682		12.04	9.617×10^{-5}
.956	.664		12.85	1.044×10^{-4}
1.17	.793		15.31	9.991×10^{-5}
1.24	.872		16.96	1.626×10^{-5}
1.24	.770		16.18	1.553×10^{-4}
1.25	.786		16.92	1.114×10^{-4}
1.33	.899		18.55	9.597×10^{-5}
1.36	.951		16.88	2.612×10^{-4}
1.70	.975		23.10	1.807×10^{-4}
1.72	.970		22.52	2.188×10^{-4}
2.06	1.082		27.48	1.664×10^{-4}
2.06	1.058		28.02	1.756×10^{-4}
2.41	1.260		30.96	1.699×10^{-4}
2.47	1.185		32.22	3.588×10^{-4}
3.05	1.425		38.62	3.960×10^{-4}

[a] P_{NH_3}: NH_3 pressure in torr.

[b] A: Absorbance at the line center.

[c] W_D: Doppler half-width in MHz.

[d] W_L: Lorentzian half-width in MHz.

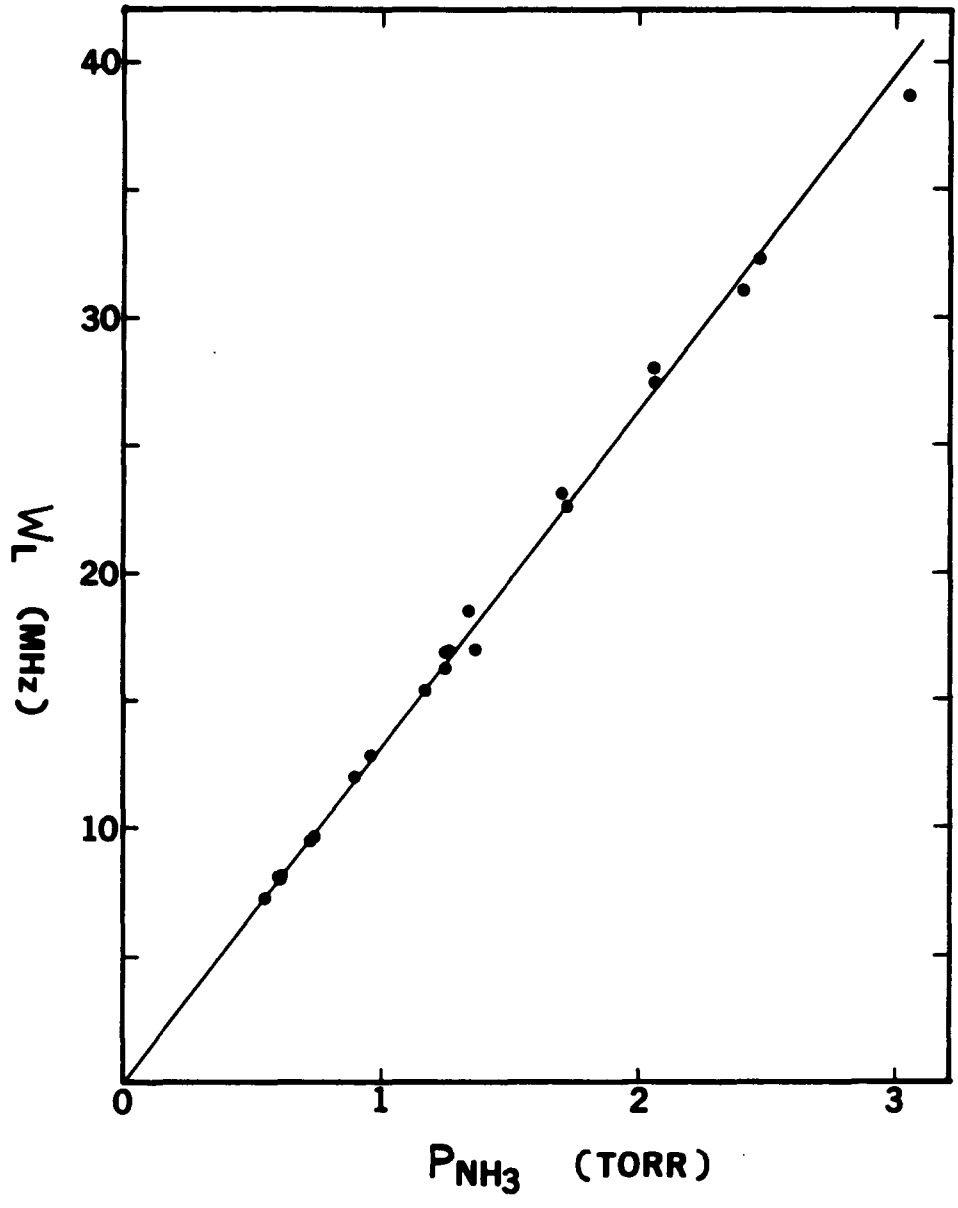

Figure 12. Self-broadened linewidths of NH_3 at 852.7 cm^{-1} using internal calibration. P_{NH_3} is NH_3 pressure and W_L is Lorentzian width (HWHM). Slope = 13.1 $\pm$0.2 MHz/torr. Correlation coefficient = 0.9981.

to be compared to the published value of 25 MHz/torr [174]. Since the cross section changes with specific vibration-rotation lines, the comparison only shows that the values are in the same general range. Naturally, because our value was obtained with internal calibration, the accuracy is expected to be higher. In addition, the accuracy of the internal calibration scheme should be even better if the very low pressure (e.g. 0.05 torr) was used to attain "pure" Doppler width instead of taking approximation approach to extract it. This can be done by simply lengthening the gas cell. However, to study the self-broadening effect of this NH_3 line, the gas cell should still be short to avoid saturation of the absorption at very low pressure.

c. Nitrogen-broadening of NH_3 In the nitrogen-broadening study of NH_3 line at 852.75 cm^{-1}, the NH_3 pressure was kept within the range of values in Table 5 and was measured for each scan. The data points were again taken in a random order, and interposed among the calibration and self-broadening data points. The highest total pressure used was 64.5 torr with nitrogen pressure at 62.3 torr, and NH_3 pressure at 3.05 torr. Above this pressure the line shape was broadened so much that it was difficult to be analyzed with sufficient accuracy. Figure 13 shows the good fitting of experimental spectral lines to Voigt profile at various pressures. Table 6 lists the spectral data of this nitrogen-broadened NH_3 line. A value for the Lorentzian component could be obtained from the best-fit Voigt profile, and must be corrected for the self-broadening of NH_3 (obtained above) before being plotted. This correction can be easily made by the subtraction of self-broadening Lorentzian component from the total Lorentzian width since the pressure-broadening effects caused by more than one species are

Figure 13. Computer plotted spectra of N_2-broadening of NH_3 line (852.75 cm^{-1}) at various N_2 pressures. NH_3 pressure is fixed to 0.894 torr.

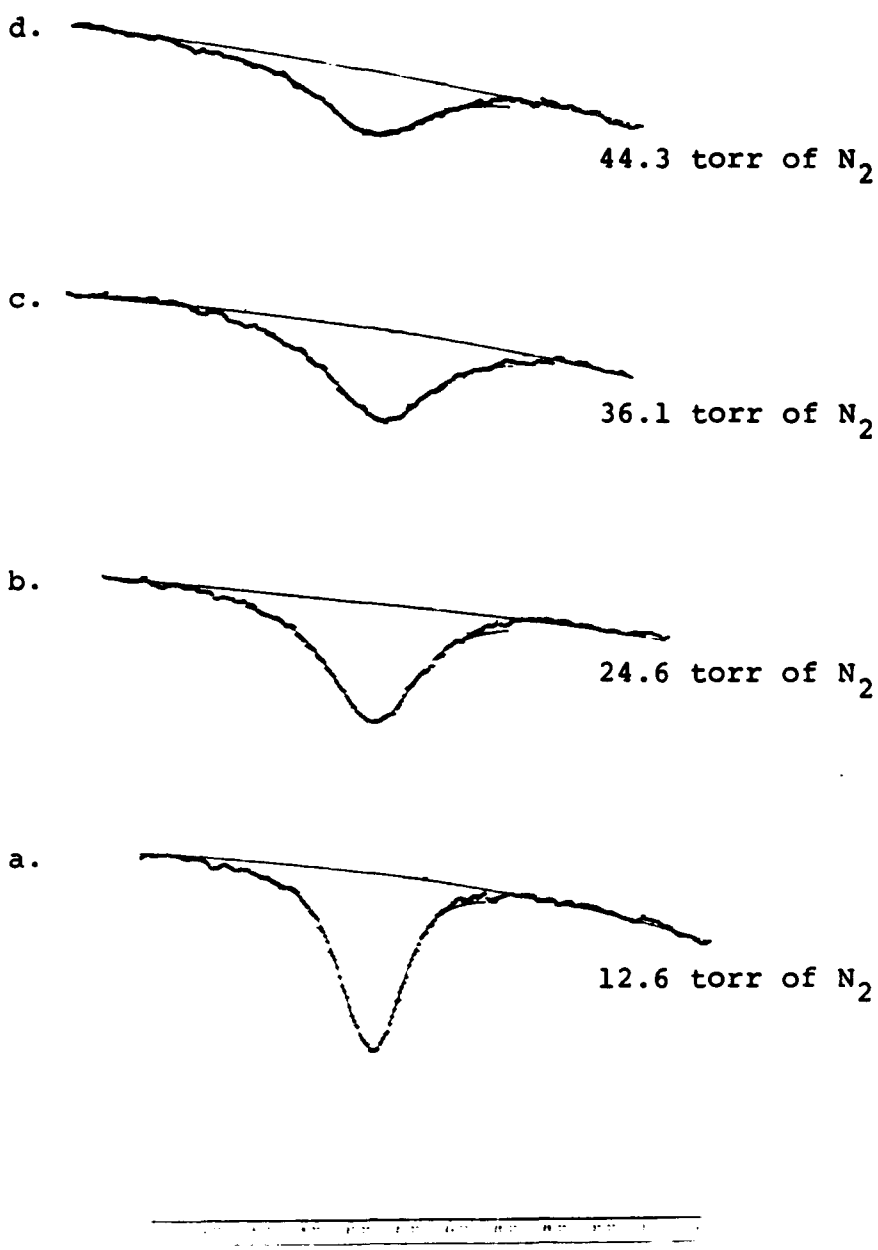
d.
44.3 torr of N_2
c.
36.1 torr of N_2
b.
24.6 torr of N_2
a.
12.6 torr of N_2

Table 6. Spectral data of N_2-broadened NH_3 line at 852.7 cm^{-1}

P_{NH_3}[a]	P_{N_2}[b]	A[c]	W_L[d]	Least-Squared Deviation
0.62	6.68	0.299	23.28	2.364×10^{-4}
	6.68	0.297	24.52	8.009×10^{-5}
	29.6	0.101	75.41	7.837×10^{-5}
	29.6	0.117	68.47	1.007×10^{-4}
	40.3	0.064	105.95	6.531×10^{-5}
	40.3	0.076	97.15	5.462×10^{-5}
0.89	12.6	0.311	40.84	7.933×10^{-5}
	12.4	0.347	37.49	1.822×10^{-4}
	24.7	0.195	75.93	1.346×10^{-4}
	24.6	0.208	79.11	1.037×10^{-4}
	36.1	0.124	107.16	1.328×10^{-4}
	36.1	0.154	104.08	5.257×10^{-5}
	44.3	0.097	108.38	7.617×10^{-5}
	44.3	0.119	108.38	7.894×10^{-5}

[a] P_{NH_3}: NH_3 Pressure in torr.

[b] P_{N_2}: N_2 pressure in torr.

[c] A: Absorbance at line center.

[d] W_L: Lorentzian half-width in MHz, corrected for the self-broadening of NH_3.

Table 6. (Continued)

P_{NH_3}	P_{N_2}	A	W_L	Least-Squared Deviation
1.16	2.80	0.624	10.60	7.717×10^{-5}
	2.78	0.624	9.137	1.010×10^{-4}
	9.14	0.425	29.76	8.142×10^{-5}
	9.13	0.420	27.81	1.185×10^{-4}
	18.4	0.277	50.55	1.390×10^{-4}
	18.3	0.280	55.00	1.408×10^{-4}
	31.0	0.182	82.53	1.497×10^{-4}
	39.7	0.129	103.92	7.145×10^{-5}
	39.7	0.146	104.43	8.544×10^{-5}
	48.9	0.097	124.19	7.885×10^{-5}
	48.9	0.104	123.29	1.413×10^{-4}
3.05	46.5	0.220	117.66	2.020×10^{-4}
	46.4	0.306	122.44	1.171×10^{-4}
	46.2	0.327	128.36	1.194×10^{-4}
	62.3	0.202	150.43	1.171×10^{-4}
	62.3	0.236	161.68	1.564×10^{-4}

additive. Figure 14 shows the nitrogen pressure vs. the corrected nitrogen-broadened Lorentzian half-width. The least-squares fit gives a nitrogen-broadening coefficient (full width) of 5.2 ± 0.1 MHz/torr and a correlation coefficient of 0.9907. This compares with the published value of 6.3 MHz/torr for another line. The slightly larger scatter, when compared with above self-broadening study, in the data here reflects the difficulty in preparing well-defined mixtures of the two gases, and the larger uncertainties in the Voigt fitting when the broadened line degraded the choice of the reference intensity I_o. The latter can probably be improved by a double-beam arrangement. Still, the internal calibration method increases the accuracy of the measurements.

2. Line positions of SO_2

Since SO_2 is one of the very important gaseous pollutants, there has been a number of experimental [63,176] as well as theoretical [177] studies on the band near 1130 cm^{-1}. The abundance of well-resolved vibration-rotation lines in this region presents a good test for our calibration scheme. 0.4 torr of SO_2 and 3.0 torr of N_2O were used in two gas cells placed in series in the light path for this study. The raw data were actually taken a few years back by Rex Morris with another laser diode. The resulting intensities over the laser scan are shown in Figure 15 as the triangular points, the level at the far right represents the zero intensity level. The baseline (reference intensity) at each absorption peak was determined by polynomial best fit of the neighboring points, and was plotted as a solid line under the SO_2 peaks (1 through 5). The best-fit Voigt profiles are also plotted as solid lines over the experimental points. As is shown in Figure 15, the fit in each case is extremely good. In fact,

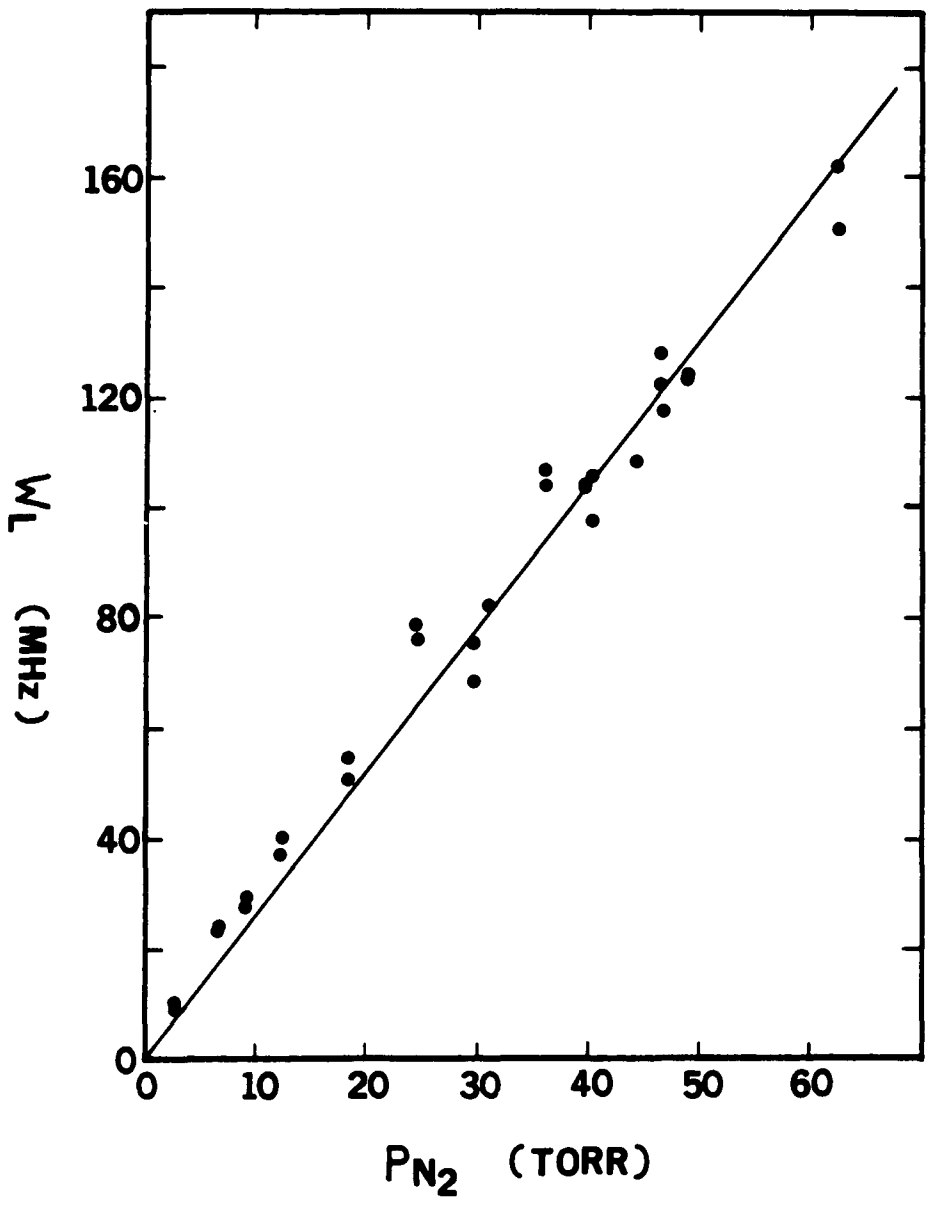

Figure 14. Broadening of NH_3 line (at 852.7 cm^{-1}) by N_2 using internal calibration. P_{N_2} is nitrogen pressure and W_L is Lorentzian width (HWHM). Slope = 2.6 $\pm$ 0.05 MHz/torr. Correlation coefficient = 0.9907.

Figure 15. Calibration of SO_2 line positions by N_2O reference lines. 1-5, SO_2 lines; A, N_2O line at 1180.052 cm^{-1}; B, N_2O line at 1180.206 cm^{-1}. Spectral fitting is described in text.

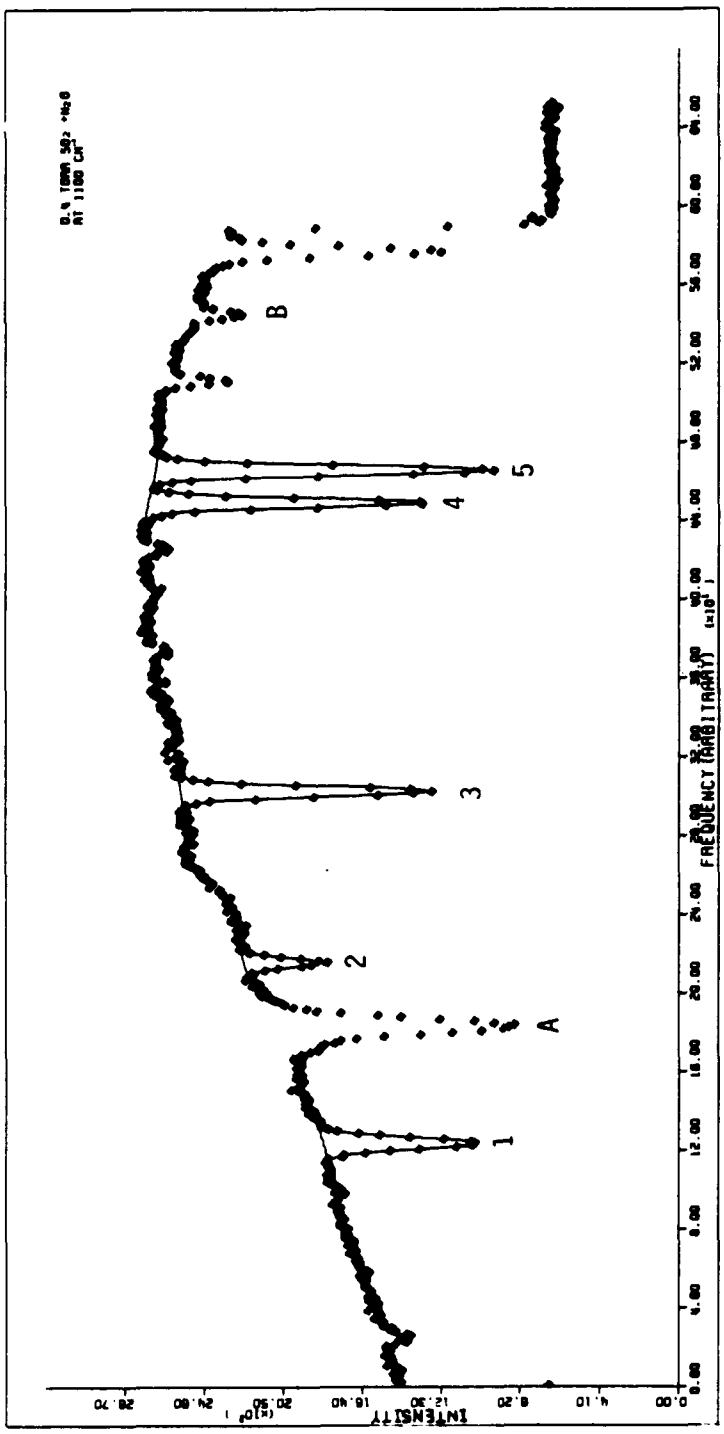
INTENSITY
FREQUENCY (ARBITRARY)
A
B
1
2
3
4
5

the average standard deviation of each experimental point from the best-fit Voigt profile is of the order of 0.01 transmittance units. The two N_2O peaks were also fitted to Voigt profiles to locate the exact line centers, which were then used as an absolute calibration.

The Doppler widths of the SO_2 lines are calculated to be 54.533 MHz be utilizing equation 3.2 with T = 298 K, ν_o = 1180.052 cm^{-1} and M = 64.063 grams. To a first approximation, ν_o was considered a constant over the narrow spectral range of the laser scan. The values of $\Delta\nu_D$, in arbitrary units, obtained from the fitted Voigt profiles were then used to determine the scan rate at each line position. These scan rates were then fitted to a 4th degree polynomial to establish the scan rates at all points in the scan. Table 7 lists the scan rate ($\Delta\nu_D/2b$) at each peak in computer unit where $\Delta\nu_D$ is the calculated Doppler width in MHz and b is the measured Doppler half-width in computer units. The change of scan rates makes a smooth curve as shown in Figure 16. The two circled dots represent data that are extrapolated from the smooth curve and all the 7 points were used for the polynomial fitting. The extrapolation is quite necessary if a good fitting to the experimental points is to be obtained.

The absolute positions are available for the N_2O lines A and B as 1180.052 cm^{-1} and 1180.206 cm^{-1} respectively [81]. The N_2O line center at 1180.052 cm^{-1} was determined with less uncertainty in these scans, so it was used exclusively for absolute calibration. The other N_2O line position served as a check of the goodness of the calibration, and was found to lie within the precision of the experiment. The positions of the SO_2 lines are determined from the scan rates as well as the absolute calibration line, i.e. 1180.052 cm^{-1} line of N_2O, by the equation:

Table 7. Peak centers and scan rates at SO_2 and N_2O line centers around 1180 cm^{-1} in computer units

Peak No.	Peak Center[a] (Computer Unit)	Scan Rate (Computer Unit)
1	123.87	10.05
2	216.11	11.18
3	302.91	11.65
4	449.36	12.72
5	466.06	12.79
A	183.25	
B	545.17	

[a]Peak center here actually only represents the current applied to the laser. It is not a linear function of the real frequency.

Figure 16. Laser frequencies in computer units vs. scan rates in computer units. Dots represent experimental data. Dots in circles represent extrapolated data. Solid line represent the best-fit fourth polynomial curve. Notice that laser frequency in computer unit is not a linear function of the real frequency.

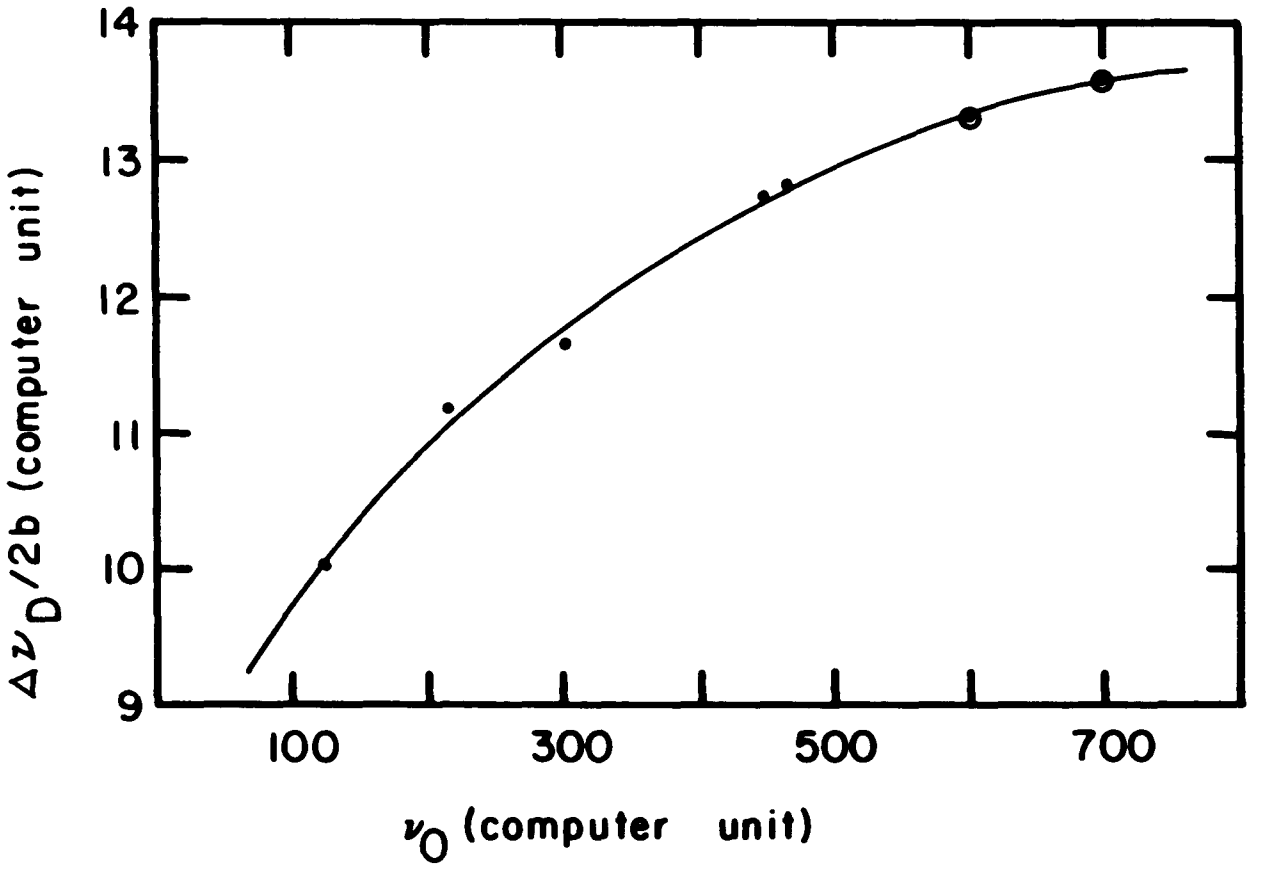
14
13
12
11
10
9
100
300
500
700
$\Delta\nu_D/2b$ (computer unit)
ν_0 (computer unit)

$$\Delta\nu = \int_{x_1}^{x_2} (\text{scan rate})\, dx$$

where scan rate = $\Delta\nu_D/2b = a_0 + a_1x + a_2x^2 + a_3x^3 + a_4x^4$.

Here x_1 is the position of 1180.052 cm^{-1} line of N_2O in computer unit, x_2 is the position of the unknown line of SO_2 in computer unit, and $\Delta\nu$ is the frequency difference between the N_2O line and the unknown line. The results obtained along with the calibrated scan rates are shown in Table 8. Figure 17 exhibits the calibrated scan rate as a function of laser frequency. The error associated with the determination of the number of computer units that corresponds to the individual SO_2 Doppler widths has been estimated to be ± 0.5%, or ± 0.3 MHz, i.e., approaching the resolution of the laser. Naturally, the uncertainty in MHz for the calibration of absolute frequency is dependent upon how far the line being calibrated is from the reference line. Lines closer to the reference can be calibrated more accurately. Because of the small error by this calibration scheme, the main uncertainty in Table 8 is dependent upon the accuracy the tabulated values of the two N_2O lines and the interpolation of the scan rate. Since reference lines can in principle be traceable to frequency standards, the uncertainty is not a limiting factor in this calibration scheme.

It should be noted that even at 0.4 torr of SO_2, the contribution of self-broadening of the spectral line cannot be neglected. The use of a Voigt profile fitting once again eliminates the need for any assumption concerning this contribution, and the Doppler contribution can be independently determined as in the study of pressure broadening of NH_3. Naturally, the gas pressure still should be low to improve the accuracy in determining the Doppler contribution. The pressure of N_2O was chosen so

Table 8. Calibrated peak centers and scan rates of SO_2 absorption lines at 1180 cm^{-1}

Peak No.[a]	Peak Center Position (cm^{-1})	Scan Rate[b] (cm^{-1}/point)
1	1180.035	6.70×10^{-4}
2	1180.068	7.46×10^{-4}
3	1180.101	7.77×10^{-4}
4	1180.160	8.48×10^{-4}
5	1180.168	8.53×10^{-4}

[a]Numbers correspond to the labels in Figure 15.

[b]Scan rate is determined as the spectral separation for consecutive data points in Figure 15.

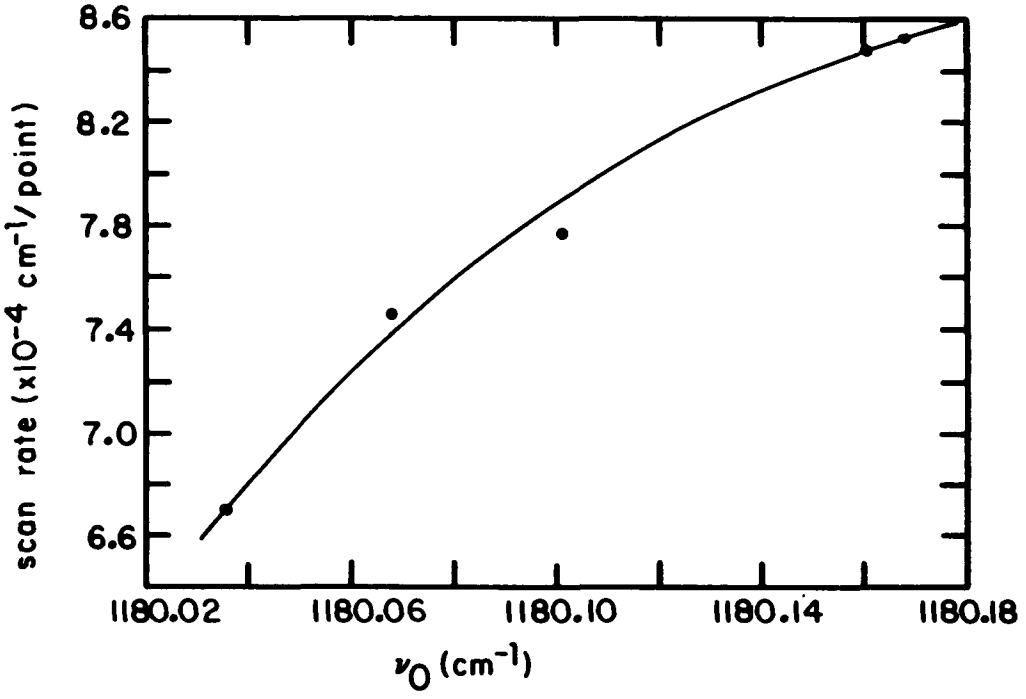

Figure 17. Calibrated scan rates as a function of laser frequency.

that the weaker line, B, showed enough absorption for satisfactory fitting. The contribution from self-broadening is much larger in this latter case. However, the location of the line center, which is the only information used, can be determined accurately for each N_2O line. The scan rate at the two N_2O lines can still be determined, but these are not used in the calibration because of the larger errors expected. The internal calibration has two advantages. First, any molecule, including the one of interest, can be used for the calibration. For systems with complex absorption bands, which in general are the ones of most interest at very high resolution, the internal calibration scheme works best because of the abundance of calibration points. Secondly, very high precision can be attained by this calibration scheme because of the sharp, Doppler-limited profiles while the broad, sinusoidal shape calibration trace produced by a typical etalon is difficult to have its peak defined to a high accuracy. For comparison, a typical commercial air-spaced etalon has a fringe spacing of 0.015 cm^{-1} (450 MHz). Assuming typical finesse, the etalon peak can only be located to an accuracy of ± 90 MHz at best. This is definitely inferior to the present scheme, which for line pairs separated by the order of the Doppler width, can be reliable to ± 0.3 MHz, simply because calibration peaks are sharper and can be much closer spaced than etalon peak. In addition, when an etalon calibration is employed, it is usually assumed a constant scan rate within the fringe. This is obviously not a good assumption for this particular kind of laser since the change of scan rate is as large as 5% in the worst case (near peak 1 and 2) for one fringe spacing.

D. Conclusion

In this chapter we have demonstrated a simple and reliable internal calibration scheme, based on the same line of interest, for the linewidth measurements, and for the determination of absolute line positions in conjunction with at least one reference line. It presented only less than ± 2% of uncertainty in pressure broadening study whereas ± 10% was a quite typical value in previous studies. As to the determination of absolute line position, this calibration scheme is the only one comparable in accuracy to heterodyne method, which is accurate to 10^{-4} cm^{-1}. The accuracy of this internal calibration can be expected to be further improved if sufficiently low pressures are used to obtain Doppler widths and if the diode laser temperature is controlled more precisely. Since the heterodyne method seriously suffers from the fact that the line of interest has to be adjacent to the gas laser line to 0.1 cm^{-1}, the internal calibration scheme therefore can be considered superior to the heterodyne method in this respect. If a minicomputer is interfaced to the laser spectrometer, the calibration can be done in essentially real time. Extension of the same concept to the calibration of tunable visible lasers should be equally reliable.

IV. PHOTOACOUSTIC DETECTION OF GASEOUS AIR POLLUTANTS

A. Background and Theory

The photoacoustic effect in both gaseous and non-gaseous matter was discovered in the nineteenth century and was first reported in 1880 by Alexander Graham Bell [178]. But evidently it was regarded as a curiosity of no practical value and soon was forgotten. It lay completely dormant for nearly 50 years until the advent of the microphone. Since then it has been used for many years mainly in nondispersive-type IR gas analyzers [179]. However, between 1950 and 1970 the photoacoustic gas analyzer employing a conventional light source gave way to the more sensitive gas chromatography. And the photoacoustic spectrometer was overtaken by the more versatile infrared spectrometer. During this period, the photoacoustic effect was primarily employed to study vibrational lifetime and other aspects of radiationless deexcitation in gases. The advent of the laser provided a major impetus to photoacoustic spectroscopy in the early of 1970s, and once again photoacoustic gas analyzers and spectrometers found exciting uses [141,149,165].

A simple physical description of the photoacoustic effect can be given by considering the following experiment. A cylindrical tube is filled with a gas mixture to be analyzed. Optical radiation containing wavelengths that can be absorbed by the gas is directed along the axis of the tube. Infrared absorption produces excited vibrational-rotational states in the absorbing molecules, and the absorption of ultraviolet radiation produces excited electronic states. Collisions between the excited molecules and

the background gas increase the translational energy and hence the pressure of the sample. The incoming radiation is modulated so that an acoustic signal is produced. A sensitive microphone connected to the wall of the chamber can be used to detect this variation in pressure. Such an instrumental setup consisting of radiation source, modulator and acoustical detector is often called spectrophone.

Roessler and Foxvog [180] have derived a very simple theory for the photoacoustic signal, which assumes a uniform pressure rise and neglects thermal and viscous losses at the cell walls. The photoacoustic signal, V, derived by this theory is expressed as

$$V = \frac{RW}{L}[1 - EXP(-\alpha CL)] \qquad (4.1)$$

where W is the incident optical power, L is the cell length, C is the sample concentration, α is the absorption coefficient, and R is the cell responsivity. The cell responsivity is given by

$$R = \frac{(\bar{\gamma} - 1)SL2\sqrt{2}}{\pi\omega V}$$

where S is the microphone sensitivity (mV/Pa), ω is the angular modulation frequency, V is the cell volume, and $\bar{\gamma}$ is the ratio of specific heats of the sample.

However, the pressure dependence of the photoacoustic signal was not included by equation (4.1) and requires a more sophisticated treatment. Wake and Amer [181] have derived an equation to describe the pressure dependence of the PAS signal of a mixture of absorbing and nonabsorbing gases, based on the equation derived by Kerr and Atwood [141] for the total pressure rise in PAS detection. There were several assumptions made in this derivation. First of all, the cell was assumed long and thin, so heat loss

through the end windows was small compared with heat loss to the walls. Secondly, the laser beam was assumed to have a Gaussian intensity distribution and cylindrical symmetry. Thirdly, an assumption of $\beta(P_0) \ll 1$ was made, where $\beta(P_0)$ was gas absorptivity at pressure P_0. When the exciting light is approximately square-wave modulated, the first harmonic lock-in amplifier output is derived as

$$V = S(P_0,\bar{\gamma},T)\beta(P_0)\frac{W}{L}\frac{P_0}{4\pi\bar{k}T}\sum_m \frac{D_m \exp(i\theta_m)}{[1 + (\omega^2 a^4/\bar{\alpha}^2\,\xi_m^4)^{\frac{1}{2}}]} \qquad (4.2)$$

where $\beta(P_0)\,\frac{W}{L}$ is power absorbed per unit length, P_0 and T are the equilibrium pressure and temperature within the cell, respectively; a is the radius of the cell, $\bar{k}$ is the effective thermal conductivity and $\bar{\alpha}$ is the effective thermal diffusivity of the mixture; ξ_m is the mth root of the zeroth order Bessel function $J_0(\xi) = 0$, $D_m(b)$ are numerically calculated coefficients which depend on b, the ratio of the Gaussian beam waist to cell radius; $S(P_0,\bar{\gamma},T)$ is the sensitivity of the microphone, and $\tan\theta_m = (\omega a^2/\bar{\alpha}\,\xi_m^2)^{-1}$. Here the dependence of the microphone sensitivity on P_0, $\bar{\gamma}$ and T is given by

$$S(P_0,\bar{\gamma},T) = S_{rated}\frac{1 + B}{1 + B(P_0\bar{\gamma}T_{STP}/P_{atm}\gamma_{air}T)}$$

where $B \cong 1$, $\bar{\gamma} = (\bar{C}_v + R)/\bar{C}_v$; $\bar{C}_v = x_i C_{pi} + (1 - x_i)C_{pj} - R$, and x_i is the molar fraction of i, the optically absorbing gas; the nonabsorbing gas is denoted by j. This equation indicates that the sensitivity of the microphone increases as the pressure decreases.

Figure 18 shows the experimental curves and theoretical curves predicted by equation (4.2) for CH_4 at a pressure of 10 torr in various nonabsorbing gases. The total pressure giving optimum PAS signal is dependent upon

Figure 18. Photoacoustic signal as a function of pressure for 10 torr CH_4 in various nonabsorbing gases. Solid lines are the theoretical predictions of equation 4.2. Modulation frequency is 50 Hz [181].

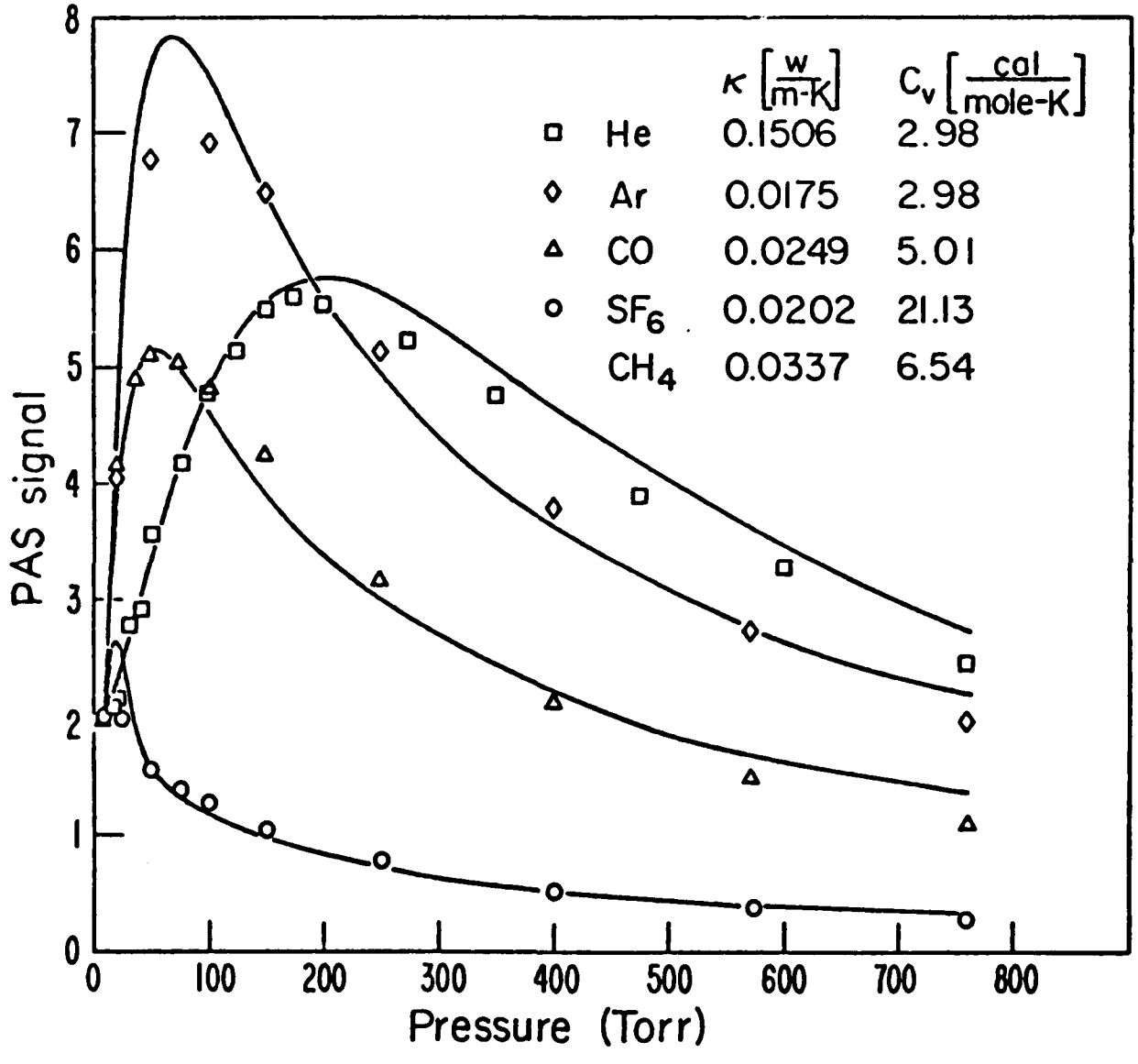
PAS signal
Pressure (Torr)
κ [w/m-K]
Cv [cal/mole-K]
He 0.1506 2.98
Ar 0.0175 2.98
CO 0.0249 5.01
SF6 0.0202 21.13
CH4 0.0337 6.54
0
1
2
3
4
5
6
7
8
0
100
200
300
400
500
600
700
800

the properties of the absorbing gases and nonabsorbing gases. However, all these curves exhibit a similar pattern for the PAS signal: first increasing, reaching a maximum value, and then decreasing. The PAS signal is also a function of modulation frequency. As shown in Figure 19, lower modulation frequency generates higher PAS signal. Since an optimum pressure exists for each modulation frequency, analytical detection based on photoacoustic spectroscopy should be performed at that pressure to achieve a better signal.

As shown in the theory, the photoacoustic signal is directly proportional to the amount of power absorbed. This in turn is related to the intensity and monochromaticity of the incident light and to the concentration of the absorbing species in the photoacoustic cell. Since lasers offer the most intense power to date, it is natural to employ them as excitation sources for PAS detection. In addition, lasers possess other advantages like monochromaticity, and collimation. While high monochromaticity offers high specificity which is required by multicomponent analysis, high degree of collimation allows the exciting energy to be focused on a small sample volume.

Besides the concern of signal intensity, noise level also must be considered in order to achieve good signal-to-noise ratio, which in turn determines the detectability of the PAS system. The ultimate detectable PAS signal is limited by noise in the transducer preamplifier and noise caused by Brownian motion of the molecules [153,154]. However, the most serious limitation to high detectability of gaseous PAS systems to date has been the background signal that is due to the photoacoustic signal from absorption of the optical beam in the cell windows, and to a lesser degree

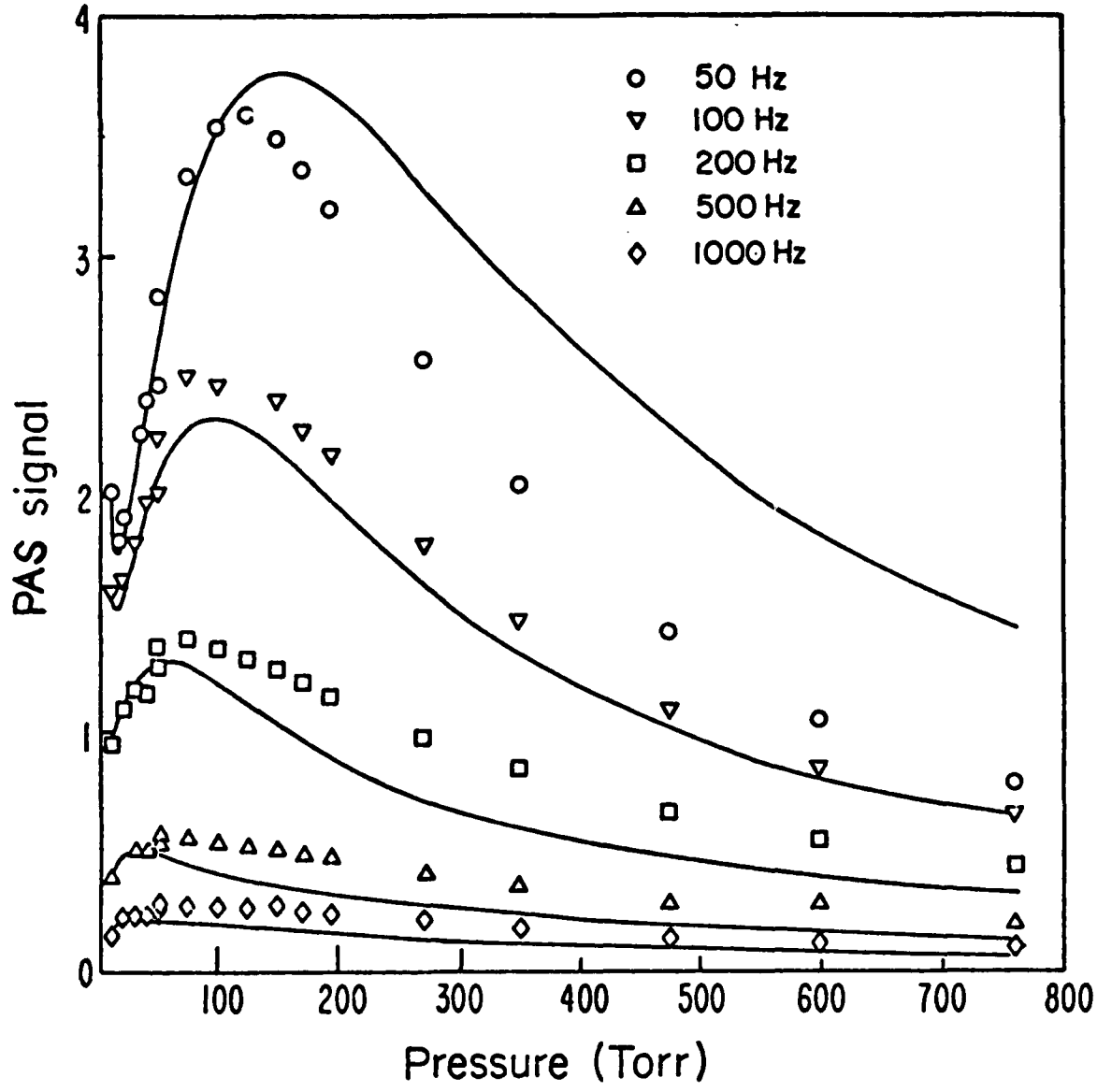

Figure 19. Photoacoustic signal as a function of modulation frequency for 10 torr CH_4 in H_2. Solid lines are the theoretical predictions of [4.2 [181].

from absorption of scattered radiation by the cell walls. There are several methods to diminish the effects of window heating: (a) using a differential cell design [151], (b) using a resonant cell [155-157]; (c) increasing the cell chamber length to reduce window background signal as compared to the gas signal; and (d) Stark- or Zeeman-modulating either the laser frequency or the spectral frequency of the absorption line [158-160].

An alternative of method (d) is to wavelength-modulate the radiation source if a continuously tunable laser is employed. Background signal due to window heating is proportional to the light intensity which is essentially constant with the small change of wavelength. Therefore, this background signal is kept as a DC signal while the true photoacoustic signal produced by the absorbing gas is modulated by wavelength modulation. By use of a phase-sensitive detection device, the DC signal is rejected and only the true PAS signal is detected. While PAS detection with high power lasers certainly benefits most from wavelength modulation, the detection utilizing weaker power lasers as diode lasers should also profit from it. However, it is important in the latter case to have both electronic noise and acoustic noise low so that these noises would not dominate the window heating background signal. Otherwise, there will not be any significant reduction on total noise.

In this work, photoacoustic detection technique is employed to the detection of NH_3, an important gaseous air pollutant. Ambient acoustic noise and building vibration noise are minimized by an isolation design. Wavelength modulation is used to reduce the window-heating background signal. The detection limit of this PAS system is examined through the

detection of NH_3 in our work.

B. Experimental

The components used in this study are listed in Table 9. Some components, such as laser packages, cryostat, laser mounts and vacuum and gas transfer system overlap those used in the study of internal calibration and will not be repeated here. Described below are the components which are essential in this experiment.

1. Photoacoustic cell and detector

The detector used in this work for the photoacoustic signal detection is a Knowles Electronics BT-1759 miniature electret microphone with a built-in FET preamplifier. The dimensions, wiring and sensitivity curve of this microphone are shown in Figure 20. It has an overall response of 10 mV/Pa, and a broad-band rms noise level of about 6.5 μV. The frequency response is flat between 100 Hz and 3 KHz. By using a lock-in amplifier tuned to the chopping frequency, the microphone noise level (which potentially represents the limit of detectivity of the system) can be reduced dramatically. The output impedance of this microphone is from 2000 to 6000 ohms (3500 ohms nominal). It should be matched with the input impedance of the lock-in amplifier to minimize the electronic noise.

The photoacoustic cell used in this experiment is shown in Figure 21. It is an acoustically nonresonant cell made of pyrex glass, with a cavity of 25 mm long and 10 mm in diameter, and is fitted with two KCl windows. The microphone was mounted to the bottom of the plug of a glass joint which was attached to the middle of the cell. When the plug was inserted into

Table 9. Experimental components for photoacoustic detection

Component	Model No.	Manufacturer
Cryostat	0-2-250+0-7M-H	Andonian, Waltham, MA
Diode laser	SDL-30	Laser Analytics, Bedford, MA
Power supply for diode supply	------	Home made
Regulated DC power supply	6226B	Hewlett-Packard, Santa Clara,CA
Monochromator	E-1	Perkin-Elmer, Norwalk, CT
Mechanical chopper	7503	Rofin, Newton Upper Falls, MA
Microphone	BT-1759	Knowles Electronics, Franklin Park, IL
Thermopile	11650	Eppley Laboratory, Newport, RI
Microvoltmeter	155	Keithley Instruments, Cleveland, OH
HgCdTe detector	DMSL 45	Infrared Associates, New Brunswick, NJ
Lock-in amplifier A	HR-8 (type C Preamplifier)	Princeton Applied Research Princeton, NJ
Lock-in amplifier B	9503	Ortec, Oakridge, TN
X-Y recorder	7001A	Moseley, San Diego, CA
Chart recorder	B5117-5I	Houston Instrument, Austin, TX
Oscilloscope	7904	Tektronix, Beaverton, OR
Capacitance manometer	221	MKS Instruments, Cleveland, OH

Figure 20. The dimensions, wiring and sensitivity curve of the Knowles BT-1759 electret microphone.

A. Dimensions and wiring

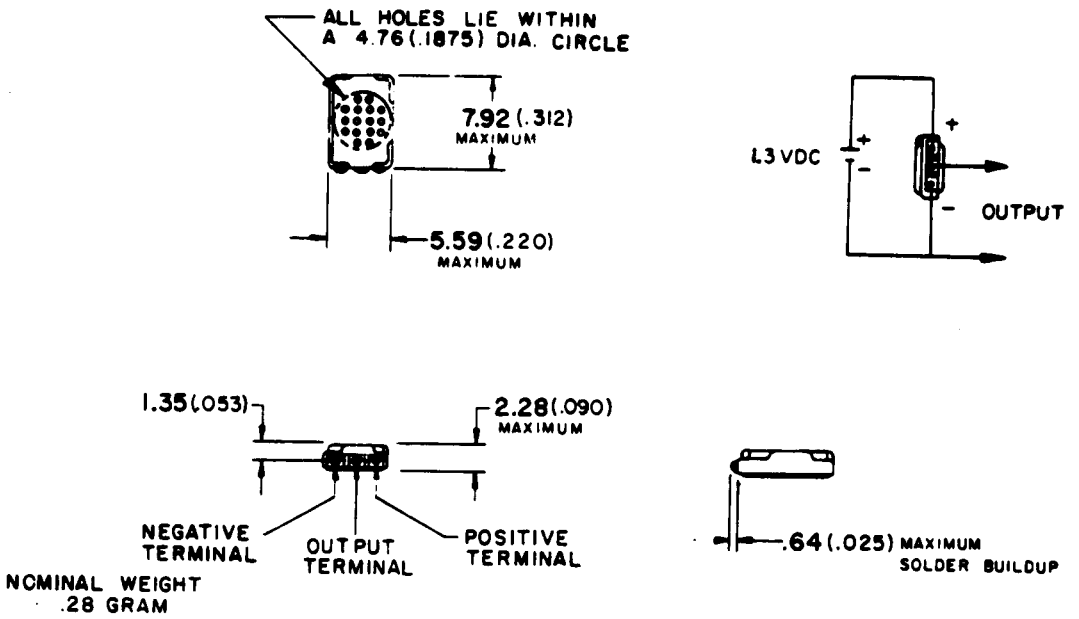

DIMENSIONS IN MILLIMETERS (INCHES)

B. Sensitivity curve

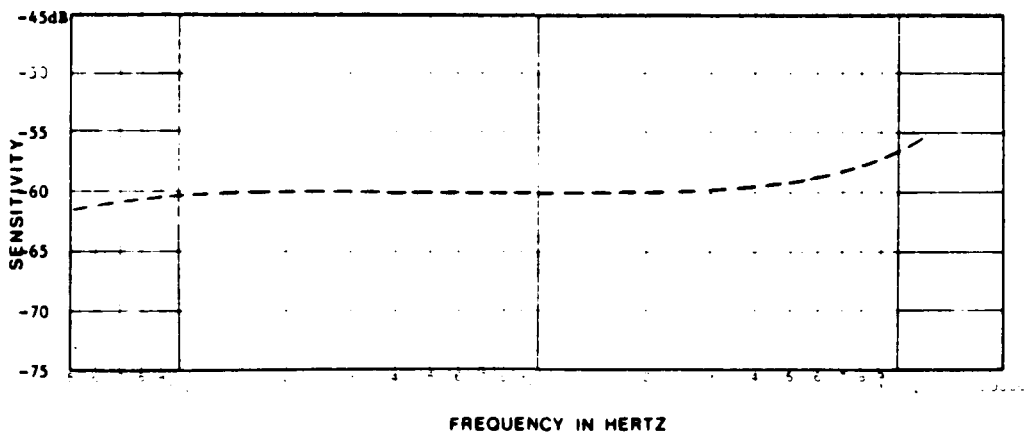

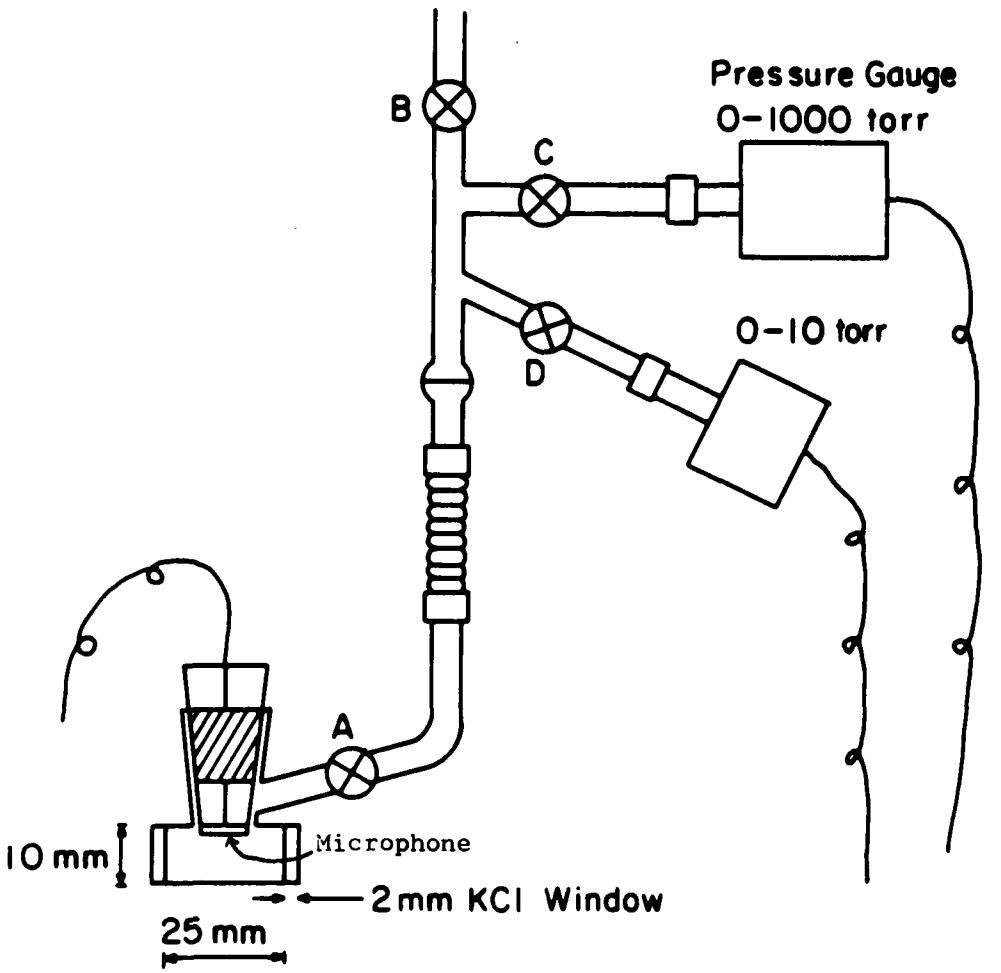

Figure 21. The design of photoacoustic cell with microphone.

the receptacle, the microphone was then flush with the inner wall of the PAS cell and its position was midway between the cell ends. The cell was designed so that two capacitance manometers, one for low pressure and the other for higher pressure can be mounted simultaneously. During the recording of the photoacoustic spectrum, valve A was kept closed. This was to minimize the acoustic noise from vacuum pumps and ambient sources. For sound and vibration isolation, the cell was mounted on a lead block, surrounded by thick rubber foam and acoustical shielding board for acoustical shielding, and enclosed in a wooden box resting on layers of rubber foam and wood.

2. Laser current supply for wavelength modulation of tunable diode lasers

In the wavelength-modulated PAS detection system, it is necessary for the diode laser current supply to have a small AC current superimposed on a current ramp. In doing so, we imposed a small change on the applied current, and the wavelength of the diode lasers varied accordingly. The power supply used in this system is a modification of the circuit used in the Chapter 3.

In the modified portion of the current supply, as shown in Figure 22, a small square wave is added to the voltage ramp which is the output from the ramp offset circuit shown in Figure 9. The heart of this circuit is a 555 integrated circuit timer which is wired to generate a square wave with a frequency of 108.7 Hz. The square wave is forward to a voltage divider to obtain a desired voltage adjustable from 0 mV to 66 mV by a 10-ohm potentiometer. This adjustable square wave and the voltage ramp from the ramp offset circuit are then summed by a 741 operational amplifier. The resulted voltage ramp which now carries a small square wave is fed into the

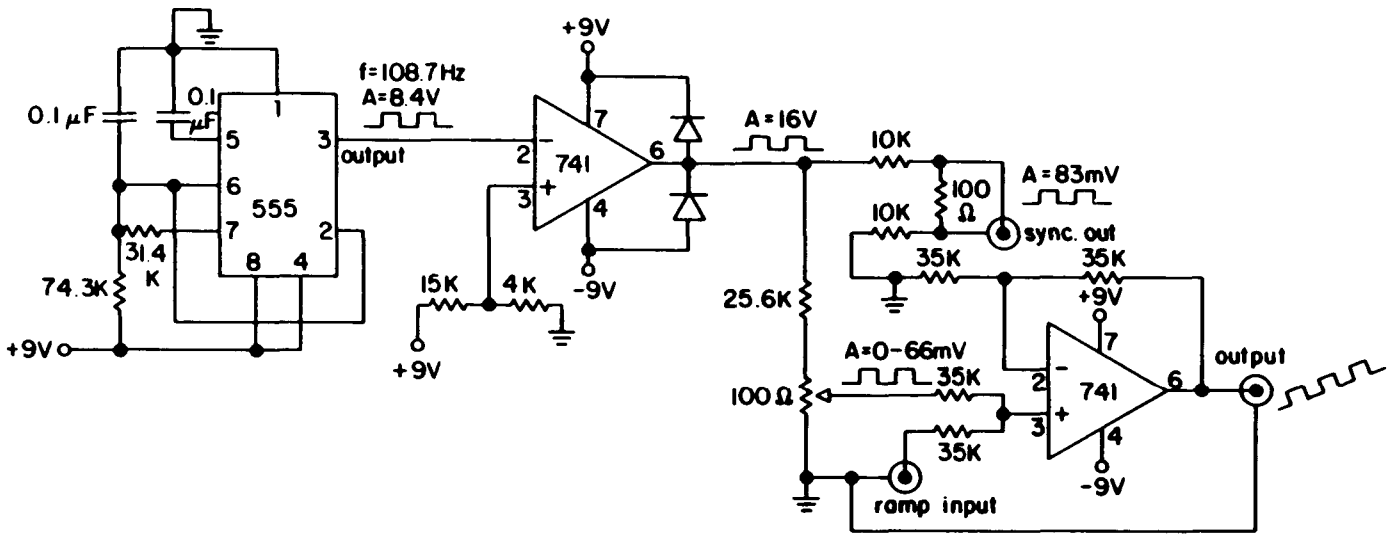

Figure 22. Modified portion of laser current supply for wavelength-modulated PAS detection.

upper circuit of Figure 9 to provide current ramp to diode lasers. A synchronous output of 83 mV is drawn from the circuit of Figure 20 to provide reference input for the phase-sensitive detection device, i.e. lock-in amplifier in this work.

3. Spectrophone setups

Two spectrophone setups were used in this work. Their schematic diagrams and descriptions are given below.

a. Spectrophone setup I This setup, as shown in Figure 23, is used for normal photoacoustic (PAS) detection. This type of arrangement facilitates both PAS detection and IR detection so that both kinds of spectra can be taken either simultaneously or independently for comparison. The laser crystal and laser current supply used here are the same ones described in the internal calibration section. Cooling was provided by the same liquid helium cryostat and again a temperature of about 4 K was used throughout this work. Radiation from the laser collected by a KCl lens of 50.8 mm diameter and 63 mm focal length and focused at the center of the PAS cell. A mechanical light chopper operating at acoustic frequency was placed in front of the PAS cell to modulate the laser beam intensity and thus generate the acoustic signal. A Knowles Electronics model BT-1759 miniature microphone (sensitivity 10 mV/Pa) with a built-in FET preamplifier was located midway between the cell ends to detect the photoacoustic signal. The reference signal from the chopper and the signal from the detector were then analyzed by an Ortec 9503 lock-in amplifier. An X-Y recorder was employed to display the photoacoustic signal intensity (Y-axis) as a function of laser current (X-axis). Also, the radiation

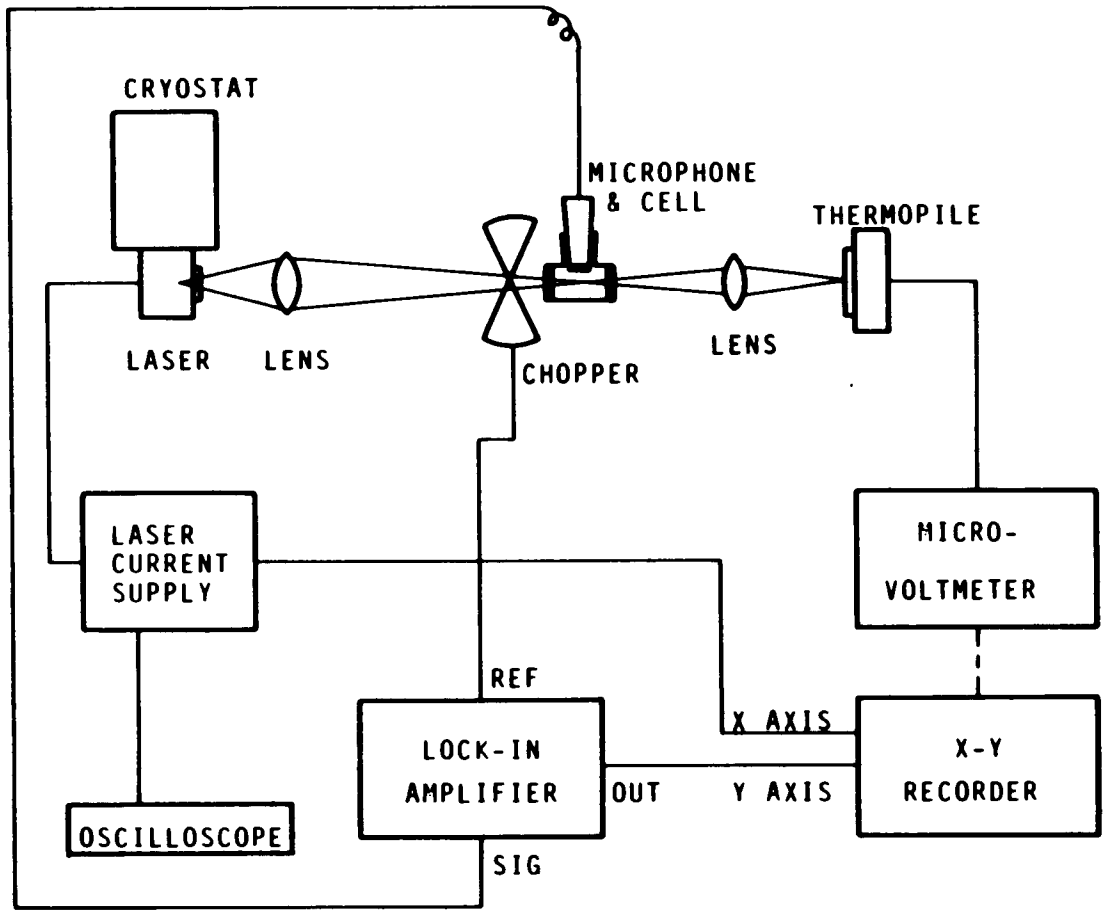

Figure 23. Spectrophone setup I.

transmitted through the PAS cell was focused onto a thermopile by a NaCl lens of 35 mm diameter and 70 mm focal length. The IR signal generated by the thermopile was then measured by a micro-voltmeter as a function of laser current and recorded on the X-Y recorder.

b. Spectrophone setup II The spectrophone setup II, as shown in Figure 24, can be used for either normal PAS detection or wavelength-modulated PAS detection. In normal PAS detection, the mechanical chopper serves as the light intensity modulator and also provides the reference signal for lock-in amplifier. In the wavelength-modulated PAS detection, the wavelength modulation is provided by the current output of laser power supply through the square wave, which by the way of synchronous output also serves as the reference signal for lock-in amplifier. In this case, the mechanical chopping is off but the chopper is left in place to avoid disturbing the whole system. Radiation from the laser was focused at the PAS cell by the KCl lens as in the spectrophone setup I. The PAS signal was again detected by the BT-1759 microphone and was displayed on the X-Y recorder as registered on the PAR HR-8 lock-in amplifier. But this time, radiation transmitted through the PAS cell was not detected by a thermopile. Instead, it was collected by a gold coated concave mirror of 108 mm diameter and 550 mm focal length. A NaCl lens of 35 mm diameter and 70 mm focal length then focused the radiation at the entrance slit of an infrared monochromator operating in the double pass mode at a dispersion of 0.97 cm^{-1}/mm. The laser radiation was again collected after the exit slit of the monochromator and focused onto a photoconductive HgCdTe infrared detector by a second gold coated concave mirror of .42 mm diameter and 67 mm focal length. The infrared signal was measured by a second lock-

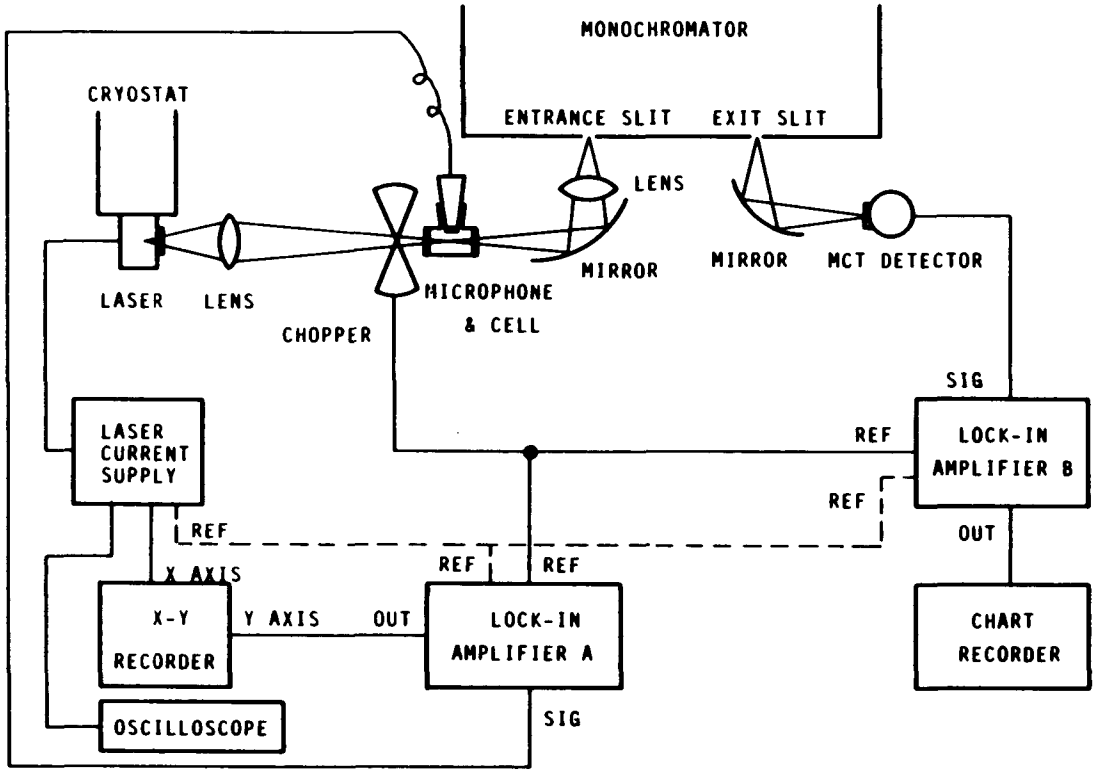

Figure 24. Spectrophone setup II.

in amplifier (Ortec 9503) and was recorded on a chart recorder. An oscilloscope connected to the laser current supply was used to display the current waveform applied to the laser.

C. Results and Discussion

1. Detection of normal photoacoustic signal

Figure 25 was taken with the spectrophone setup I, and shows the transmitted power and normal photoacoustic signal vs. diode injection current for NH_3 at a pressure of 598 torr. Dotted curve, a, represents the total output power of the diode laser with several modes emitting simultaneously. The relative strengths and spectral frequencies of those modes vary with diode injection current and temperature. Trace b shows the transmitted power through the gas cell, measured by thermopile and trace c shows the photoacoustic signal measured by microphone and lock-in amplifier. After comparing trace b with c, it is obvious that photoacoustic signal appears wherever there is an absorption. As would be expected from theory, an increase in absorption leads to an enhanced photoacoustic signal, naturally the peaks of photoacoustic signal coincide with the region with least transmitted power.

Figure 26 shows the effect of total pressure on photoacoustic spectra, and the photoacoustic signal strength as a function of total pressure is shown in Figure 27. By visual inspection, it is evident that the lone peak on the right end of the spectrum in Figure 26 should be the best one to choose for analytical purposes because it not only is well-separated from other peaks, but also has the strongest intensity. Also clear is that even

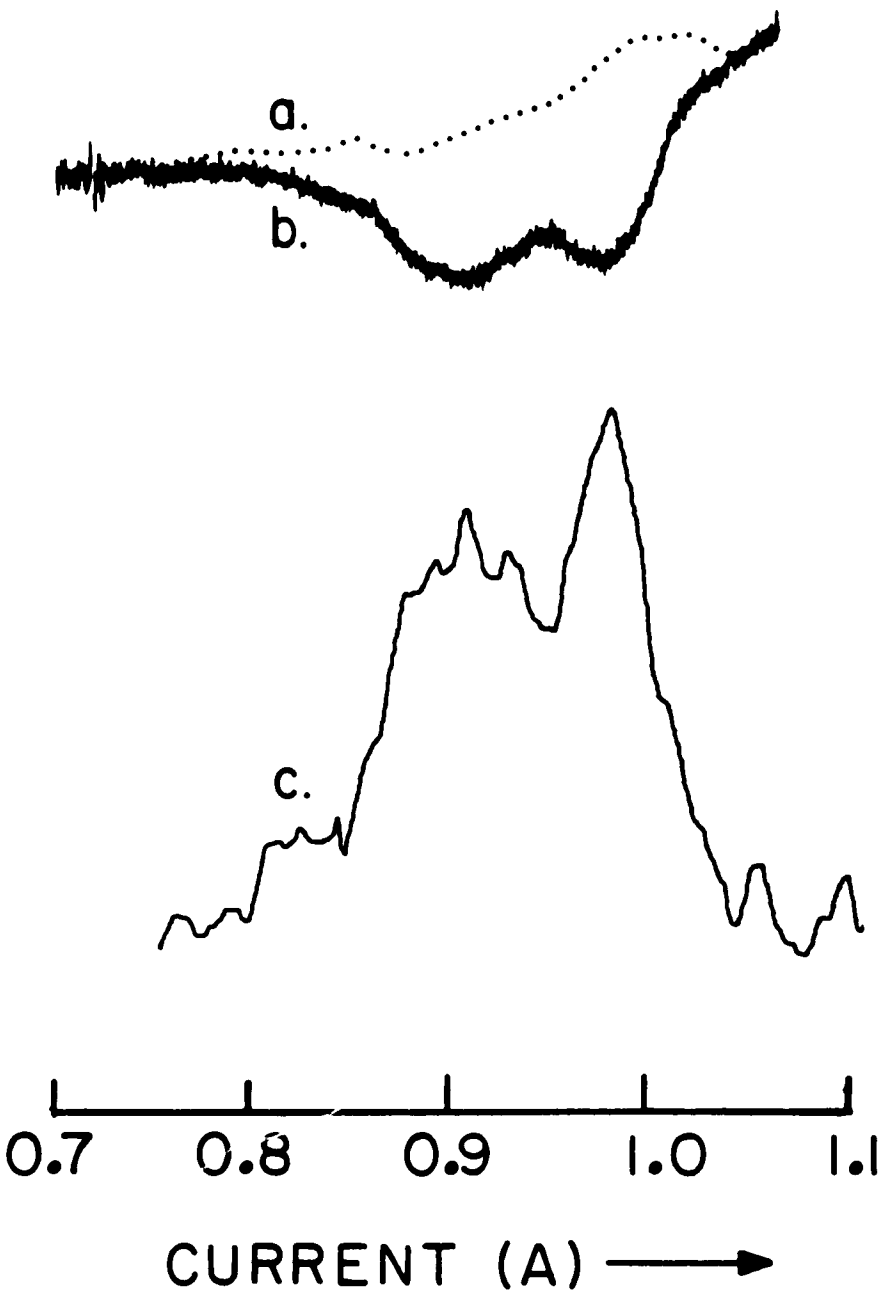

Figure 25. Transmitted power (b) and normal photoacoustic signal (c) vs. diode injection current for 598 torr of NH_3. Also shown is laser power spectrum (a).

Figure 26. The effect of total pressure on photoacoustic spectra of NH_3 in air. Abscissas represent frequencies (arbitrary unit), ordinates represent PAS signals. (arbitrary unit) Partial pressure of NH_3 is fixed to 4.2 torr while the total pressure is varied as follows: a, 4.2 torr; b, 9.5 torr; c, 14.1 torr; d, 18.8 torr; e, 28.6 torr; f, 41.3 torr; g, 60.4 torr; h, 88.1 torr; i, 167.5 torr; j, 478.6 torr.

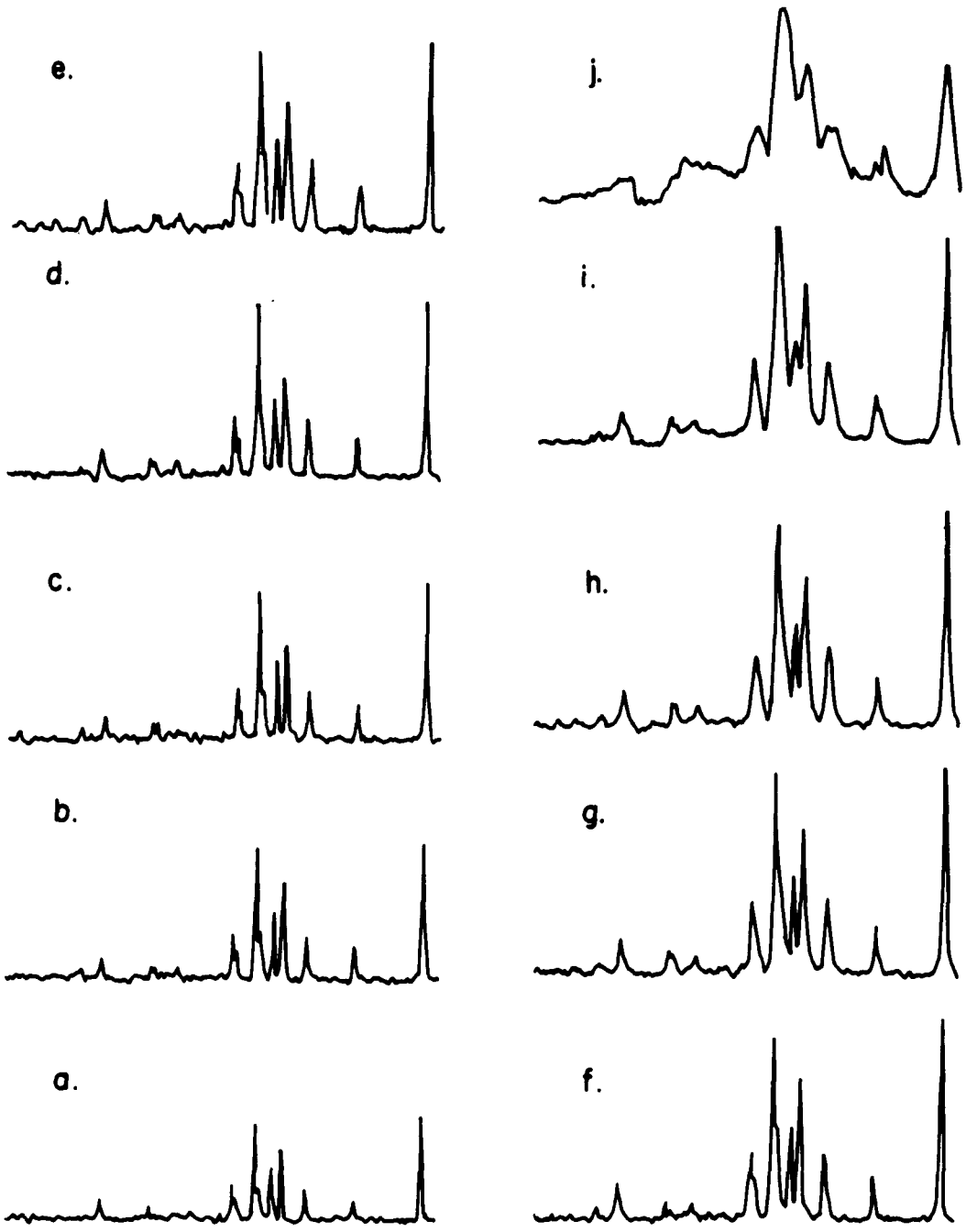
e.
j.
d.
i.
c.
h.
b.
g.
a.
f.

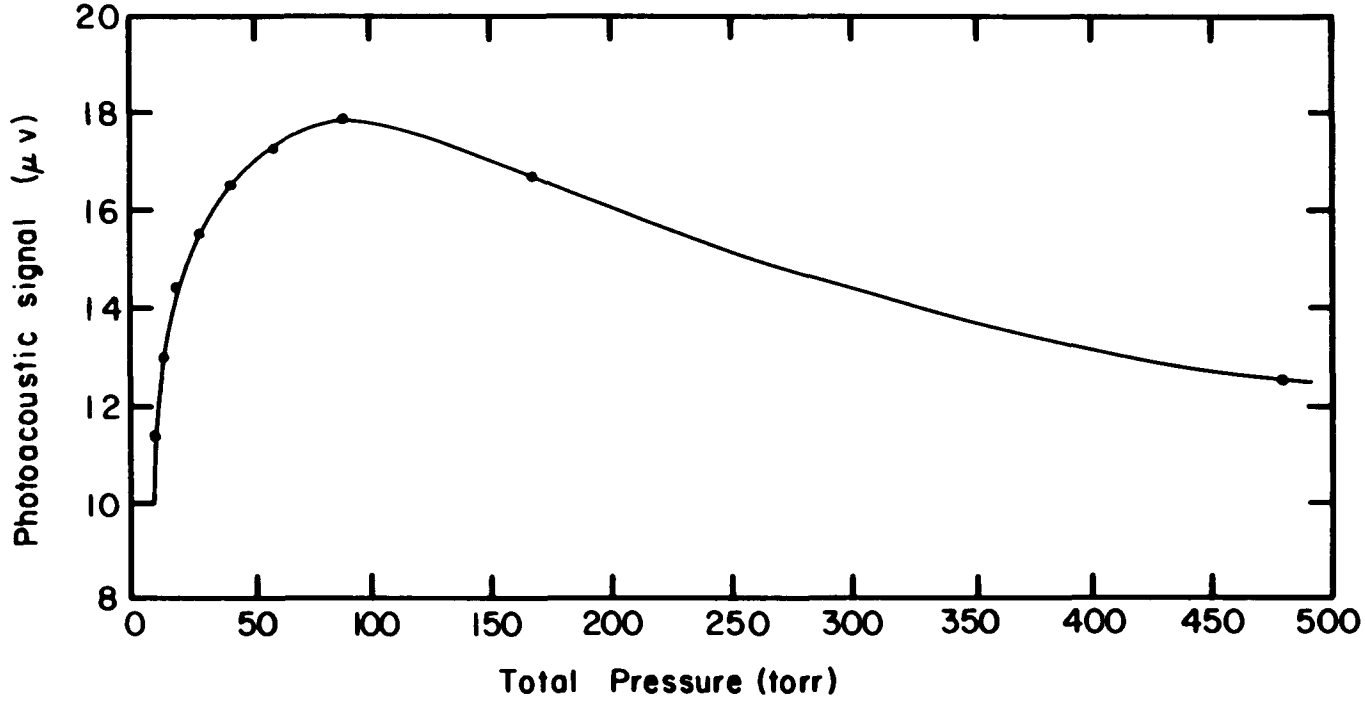

Figure 27. Photoacoustic signal as a function of total pressure for NH_3 line at 872.59 cm^{-1} with 4.2 torr of NH_3 in air.

at total pressure of about 30 torr to 40 torr, peak intensity is not compromised while the resolution is still quite sufficient to provide high selectivity for multicomponent analysis.

2. Identification of absorption lines

The identification of seven strong photoacoustic peaks (peak number 2 through 8), observed at injection current from 0.970 amperes to 1.221 amperes (as shown in Figure 28), was established through two stages: (a) sorting out the photoacoustic peaks caused by different diode laser modes; (b) comparing experimental infrared spectra with literature data of line centers and line intensities.

In the first stage, infrared spectra in different modes, as shown in Figure 29, were taken by the spectrophone setup II right after the recording of Figure 28. Current applied to the diode laser at the peak centers was measured for spectra in both Figure 28 and 29. These current values obtained for the two types of spectra then were used to identify these peaks since peaks shown in Figure 29 must correspond to those shown in Figure 28 with the same values of injection current. Peak number 2 through 8 were identified accordingly.

In the second stage of identification, diode laser infrared spectra of the four modes were compared with literature data [125,175,182] which are shown in Table 10. Figure 30 shows an FTIR spectrum of NH_3 (12 torr) taken by a FTIR spectrometer (IBM IR/98, Bruker, Karlsruhe, West Germany) with resolution of 0.06 cm^{-1}. The peak positions obtained by FTIR are also listed in Table 10. In the infrared spectra a, b, and c, monochromator spectral width was only 0.2 cm^{-1}; therefore, the peaks shown

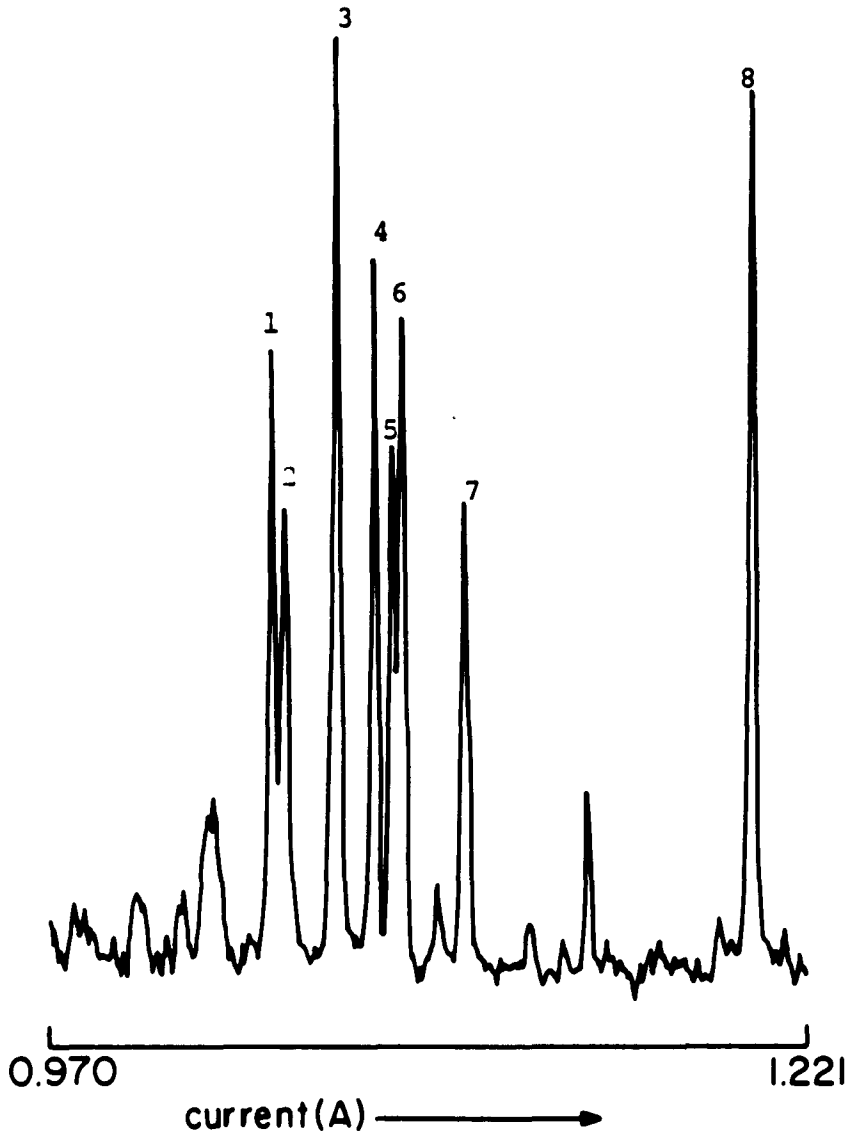

Figure 28. Photoacoustic spectrum of 2 torr NH_3 in 18 torr air around 870 cm^{-1}. peak 2: 867.517 cm^{-1}; peak 3: 867.717 cm^{-1}; peak 4: 867.870 cm^{-1}; peak 5: 867.967 cm^{-1}; peak 6: 868.001 cm^{-1}; peak 7: 871.753 cm^{-1}; peak 8: 872.589 cm^{-1}.

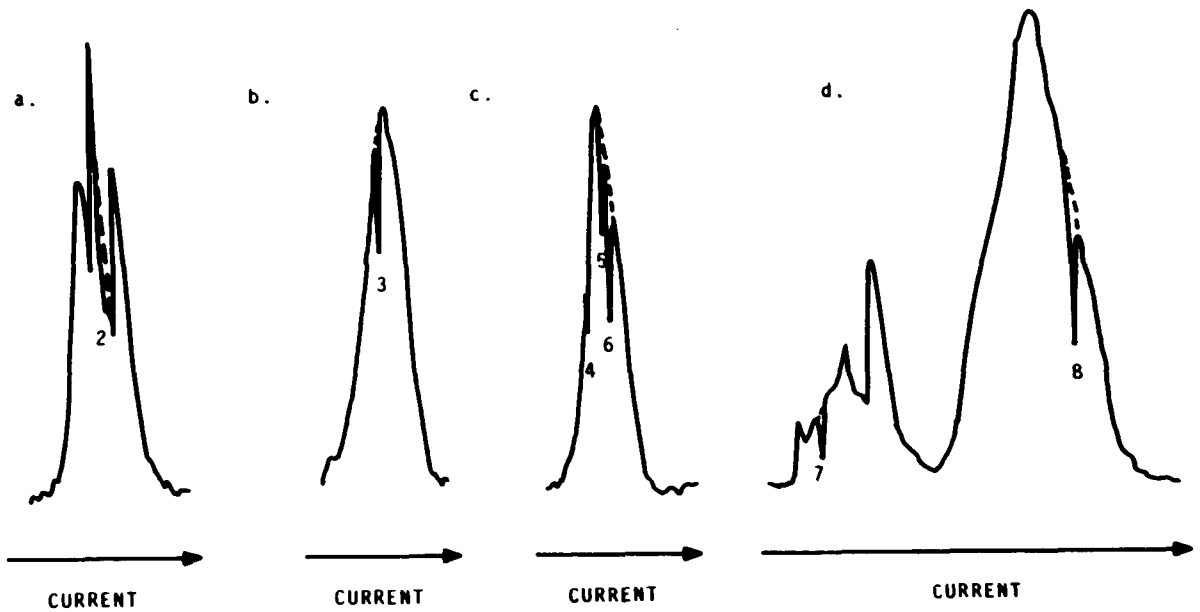

Figure 29. Diode laser infrared spectra of 2 torr NH_3 in 18 torr air in modes around 870 cm^{-1}. a, mode center at 867.52 cm^{-1}; b, mode center at 867.77 cm^{-1}; c, mode center at 868.02 cm^{-1}; d, mode center at 872.23 cm^{-1}. Spectra a, b and c are taken with monochromator spectral width of 0.2 cm^{-1}. Spectrum d is taken with that of 0.7 cm^{-1}. Number 2 through 8 correspond to peak numbers in Figure 28.

Table 10. Line centers and line intensities of NH_3 absorption around 870 cm^{-1}

Peak No.[a]	Transition	Line Frequency (cm^{-1})				Line Intensity ($cm^{-2}atm^{-1}$)		
		Cappellani and Restelli [125]	Curtis [182]	Taylor [175]	FTIR[b]	Cappellani and Restelli [125]	Taylor [175]	FTIR[c]
2	sP(5,4)	867.5173	867.5173	867.502	867.58	0.94	0.94	6
3	sP(5,3)	867.7177	867.7175	867.744	867.80	2.7	2.94	3
4	sP(5,2)	867.8706	867.8825	867.923	867.95	1.6	1.76	5
5	sP(5,1)	867.9672	867.9799	868.032	868.07	1.8	1.91	1
6	sP(5,0)	868.0012		868.069		4.0	3.90	
7	sP(3,2)			871.753	871.82		1.68	4
8	sP(3,1)			872.589	872.66		2.54	2

[a] Peak numbers correspond to those in Figure 28 and 29.

[b] FTIR spectrum were taken by IBM IR/98.

[c] Line intensities were not obtained but justified in the order of relative strength. Strongest peak is marked 1, weakest one is marked 6. Smaller number indicates stronger peak intensity.

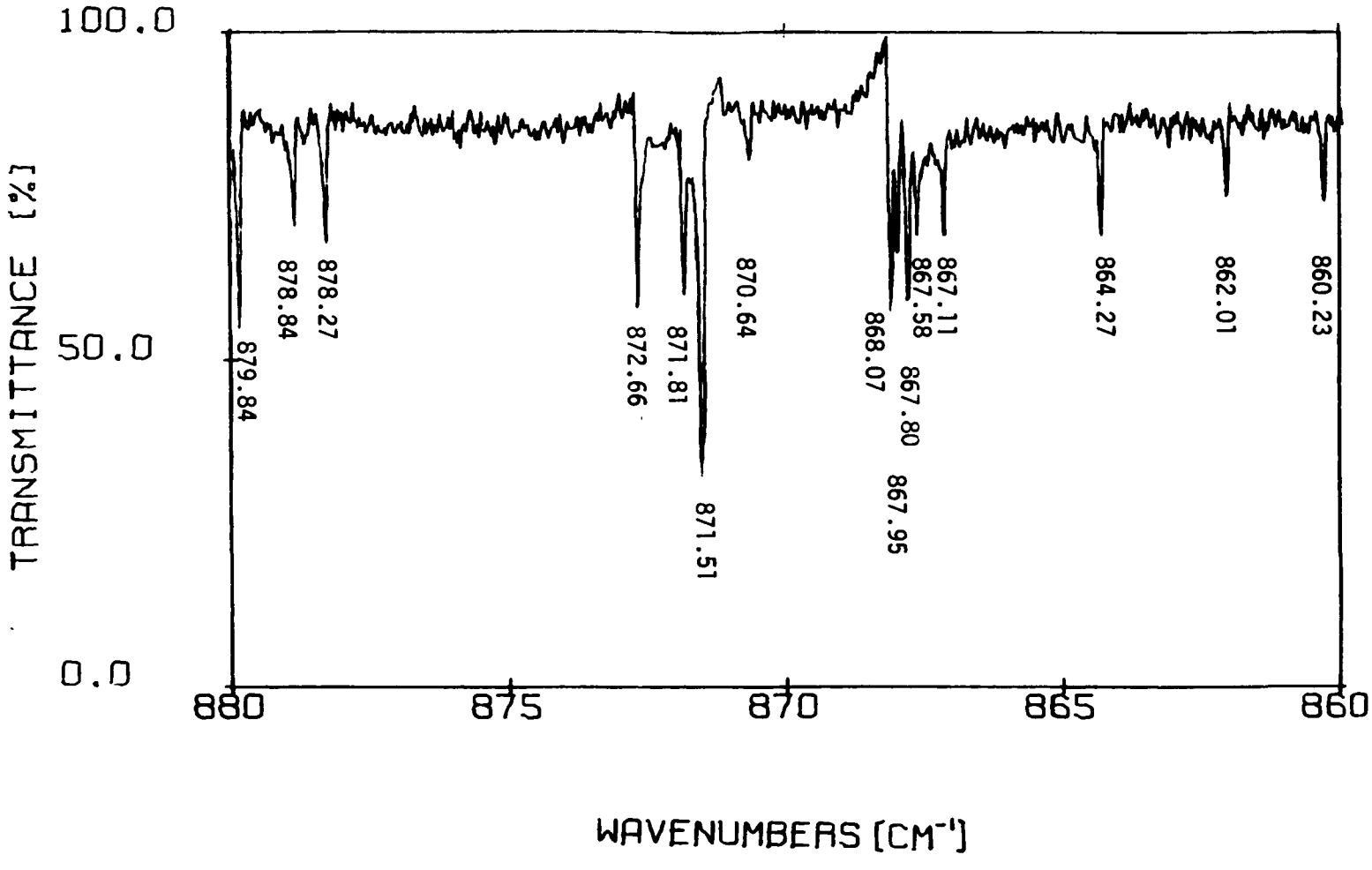

Figure 30. FTIR spectrum of 12 torr NH_3 between 860 cm^{-1} to 880 cm^{-1}. Cell length = 2 cm, resolution = 0.06 cm^{-1}.

in these modes could be identified easily by comparing mode center with literature values of peak positions. Spectrum d had a monochromator spectral width of 0.7 cm^{-1} and the mode center was at 872.23 cm^{-1}, therefore peak 7 and peak 8 must have line position on opposite sides of 872.23 cm^{-1} and have a separation of about 0.7 cm^{-1}. The peaks 2 through 8 were identified accordingly as sP(5,4) at 867.571 cm^{-1}, sP(5,3) at 867.717 cm^{-1}, sP(5,2) at 867.870 cm^{-1}, sP(5,1) at 867.967 cm^{-1}, sP(5,0) at 868.001 cm^{-1}, sP(3,2) at 871.753 cm^{-1} and sP(3,1) at 872.589 cm^{-1}. The sP(3,1) line at 872.589 cm^{-1} was chosen for this study because of its high intensity and freedom from interference.

3. Selection of modulation frequency

Since both photoacoustic signal and noise are affected by modulation frequency, the modulation frequency, f, should be selected carefully to attain the best signal-to-noise ratio.

The photoacoustic noise was studied with spectrophone setup II without the laser irradiation. The gas cell was filled with 48 torr of air. In order to avoid the mechanical vibration caused by the mechanical chopper, a WAVETEK Model 162 function generator (WAVETEK, San Diego, CA), instead of the chopper, was used to provide the reference signal for the lock-in amplifier. The main sources of noise in this case are ambient acoustic noise, ambient vibrational noise and electronic noise. The noise spectrum of noise vs. 1/f as shown in Figure 31, shows approximately a linear relationship between the two.

Wake and Amer [181] have studied the effect of modulation frequency on photoacoustic signal. A plot of photoacoustic signal as a function

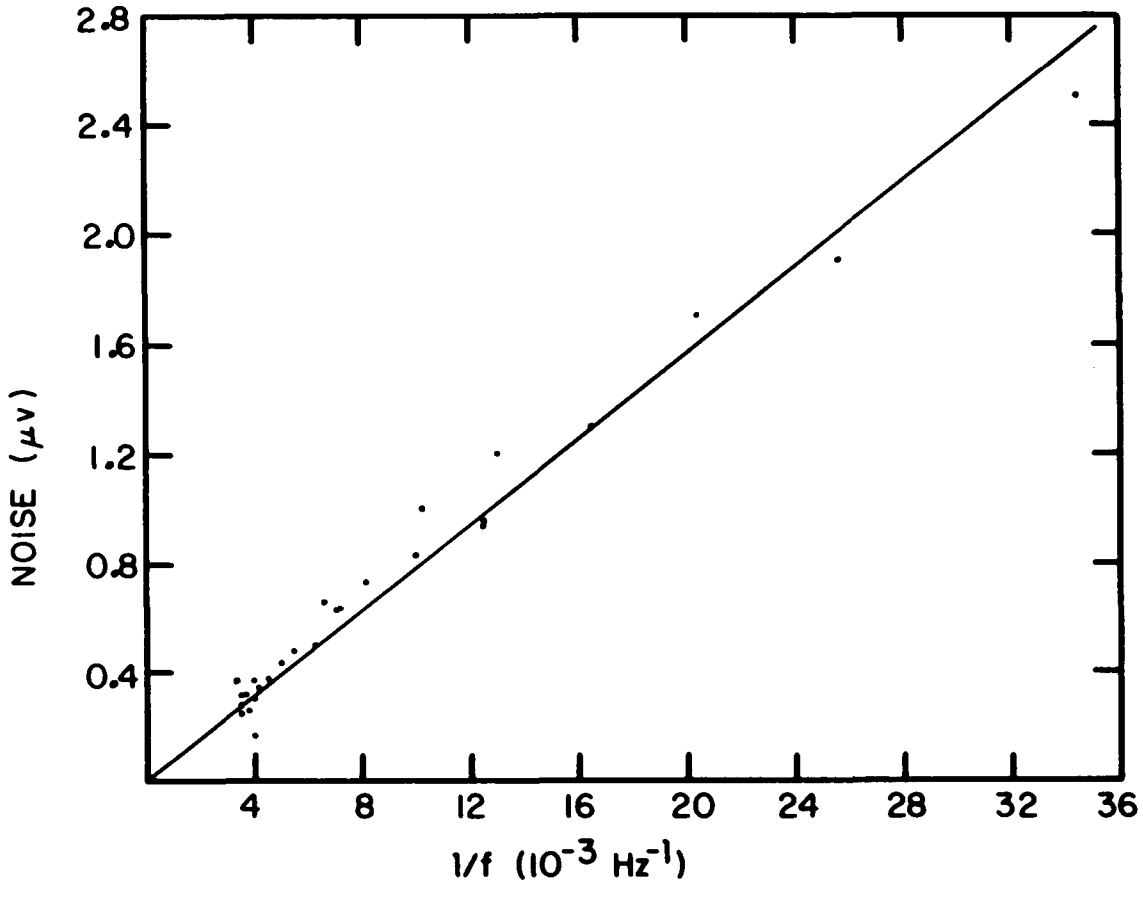

Figure 31. Photoacoustic noise as a function of inverse frequency. Dots represent experimental data. Solid line represents the best-fit line of these data. Slope = 0.0783, correlation coefficient = 0.9895.

of 1/f, derived from their study, is shown in Figure 32. It is seen from this figure that these functions vary with total pressure in the gas cell. Below about 100 Hz of modulation frequency, the signal is no longer a linear function of 1/f for total pressures of 50 torr and 100 torr, but curved downward with the increase of 1/f. This implies that one should not use a frequency of less than 100 Hz for the photoacoustic detection at total pressure of 100 torr or less. One should notice that the figure, 100 Hz, should vary with the absorbing gas (CH_4 in this case and NH_3 in our system) and the nonabsorbing gas (H_2 in this case and air or nitrogen in our system). When frequency of higher than 100 Hz is used, both signal and noise are linear function of 1/f, and thus the signal-to-noise ratio is a constant for all those frequencies. Based on the above discussion, modulation frequency of 109 Hz was used throughout our experiments of photoacoustic detection.

4. Wavelength-modulated photoacoustic detection

a. Comparison of wavelength-modulated photoacoustic spectrum with normal photoacoustic spectrum A comparison of wavelength-modulated photoacoustic spectrum with normal photoacoustic spectrum is shown in Figure 33. Both spectra were taken by the spectrophone setup II equiped with PAR HR-8 lock-in amplifier. However, in the normal spectrum the mechanical chopper was used for intensity modulation while in the wavelength-modulated spectrum the new current supply, described earlier in this chapter, was employed for the wavelength modulation. In Figure 33, the signal-to-noise ratio of wavelength-modulated photoacoustic signal was obviously better than that of normal photoacoustic signal. About a

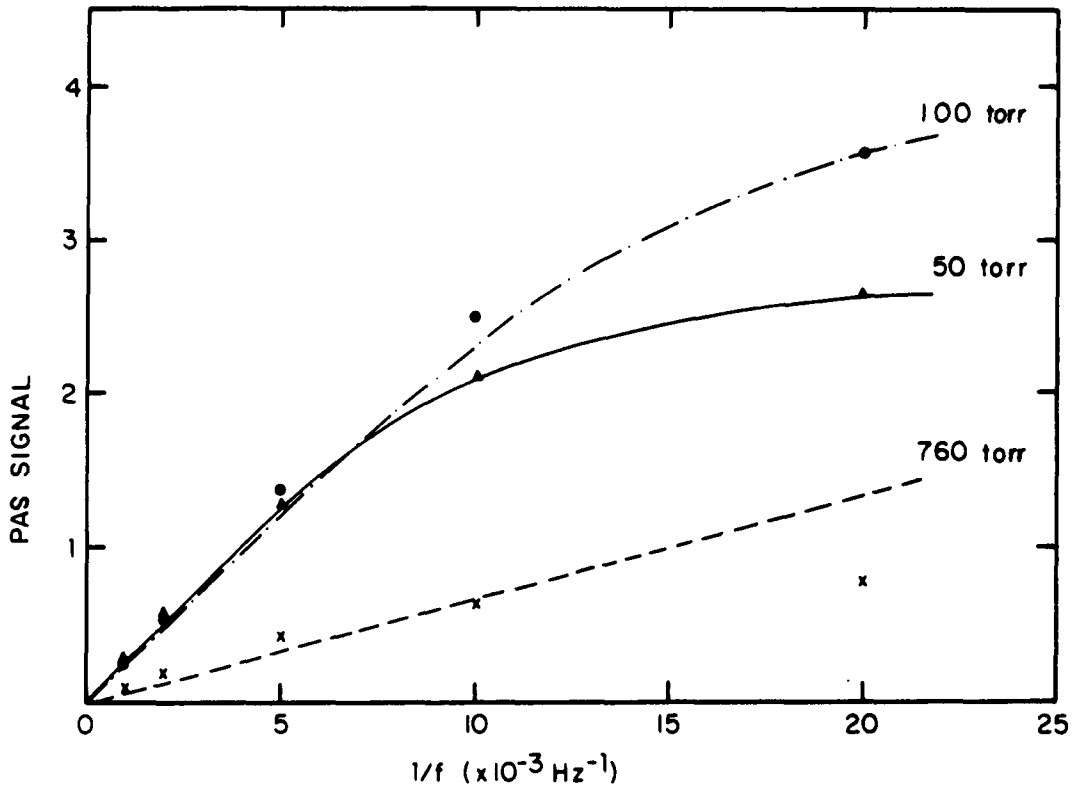

Figure 32. Photoacoustic signal as a function of inverse frequency for 10 torr of CH_4 in air [181]. Triangles, dots and crosses represent experimental data for total pressure of 50 torr, 100 torr and 760 torr respectively. Continuous lines are theoretical curves.

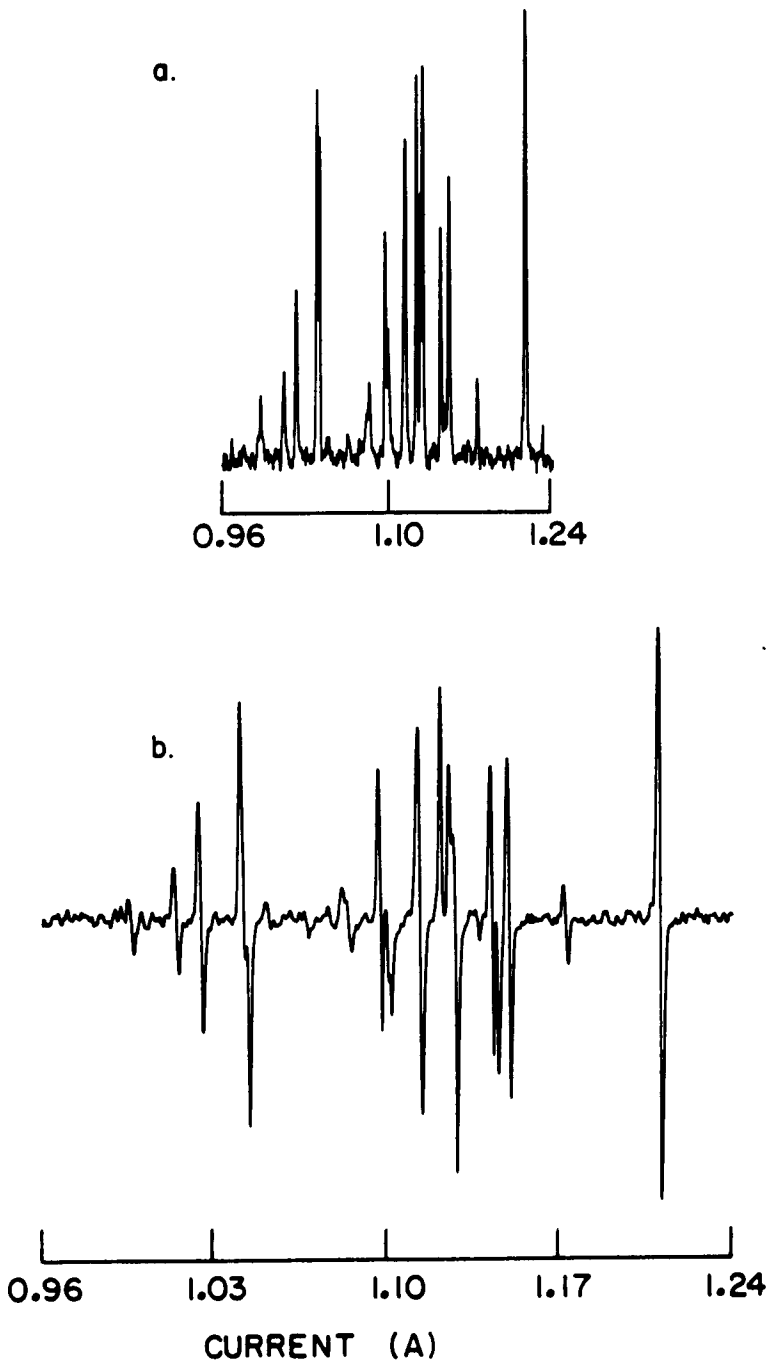

Figure 33. Comparison of normal photoacoustic spectrum (a) with wavelength-modulated photoacoustic spectrum (b) for 0.8 torr NH_3 in 11 torr N_2.

factor of 3 of improvement was obtained. If the window heating background is the major source of noise, one would expect that a much greater improvement could be obtained by using wavelength modulation approach. Since this improvement was not as great as would be expected, this fact indicates that the window heating background is not a serious problem in this system due to very low power laser used as excitation source. So, the major sources of noise in this wavelength-modulated system must be ambient acoustic noise and electronic noise. With bandwidth of 10 Hz and time constant of 10 seconds on lock-in amplifier, the system noise was observed between 0.3 μV to 0.4 μV which was comparable with that obtained by Gerlach and Amer with the same type of microphone [183]. This noise was experimentally verified being dominated by electronic noise. This noise level is considered quite high for photoacoustic detection and further reduction is possible. Electronic noise introduced by microphone can be reduced by reducing the bandwidth of the microphone response frequency with a lock-in amplifier since the microphone noise is proportional to the square root of the bandwidth. Also, since the built-in FET preamplifier is the principle contributor to the microphone noise, the use of a high quality FET amplifier, which is available with intrinsic noise level of 10 $nV/Hz^{\frac{1}{2}}$, should bring down the microphone noise level significantly [162]. Additional electronic noise introduced by subsequent amplification and signal processing, cable pick-up, etc. can be reduced by careful electronic design. Dewey [162] had measured values of 28 nV from these sources and estimated that it can be reduced to 17 nV, yielding a total electronic noise of about 20 to 30 nV. This figure is more than 10 times better than the observed

noise in our system.

b. The effect of modulation amplitude on wavelength-modulated photoacoustic signal The wavelength-modulated photoacoustic signal is a function of modulation amplitude, as shown in Figure 34 and 35. With the increased modulation amplitude, the PAS signal first increased, reached a maximum (optimum point) then decreased. The modulation amplitude which corresponds to the maximum signal at certain total pressure is defined as the optimum modulation amplitude. The position of optimum point varies with the peak linewidth which is determined by both the pressure of absorbing gas and the pressure of nonabsorbing gas. In Figure 35, the four optimum points shifted from low modulation amplitude to higher modulation amplitude with the increase of total pressure, i.e. the increase of linewidth. In Figure 34, the linewidth was so narrow that even a modulation amplitude of only 0.2 mV was too great to obtain optimum point.

c. The effect of total pressure on wavelength-modulated photoacoustic signal Experimentally measured wavelength-modulated photoacoustic signals as functions of total pressure with modulation amplitude fixed at 2 mV and 0.3 mV respectively are shown in Figure 36. A similar plot but using optimum modulation amplitude at each total pressure is shown in Figure 37. All these plots have maximum signal around total pressure of 20 torr. Therefore, to obtain the best signal-to-noise ratio, one should choose a total pressure of about 20 torr and a modulation amplitude which produces maximum signal at this pressure. This condition of low total pressure would also be ideal for multicomponent analysis because high selectivity can be achieved through the high resolution

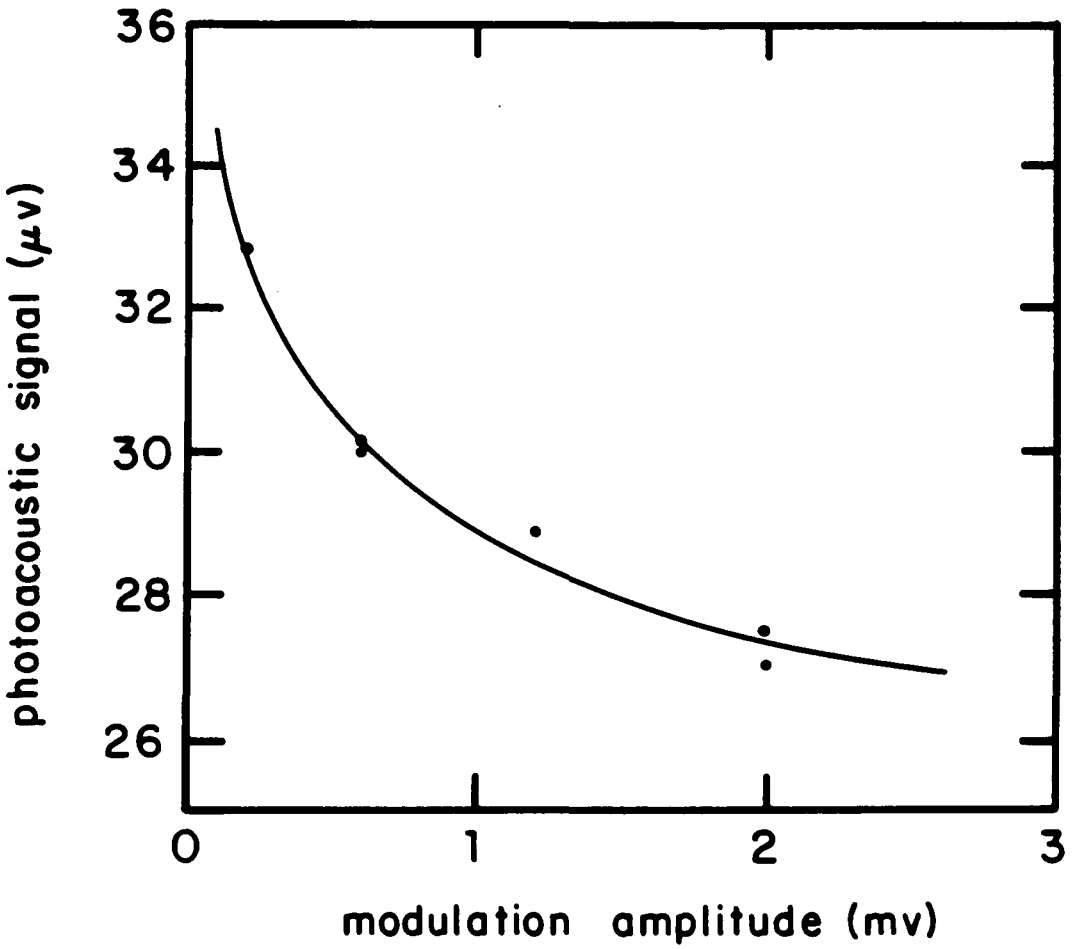

Figure 34. The effect of modulation amplitude on wavelength-modulated photoacoustic signal of NH_3 absorption line at 872.59 cm^{-1} with 0.8 torr of NH_3 in 9 torr of nitrogen.

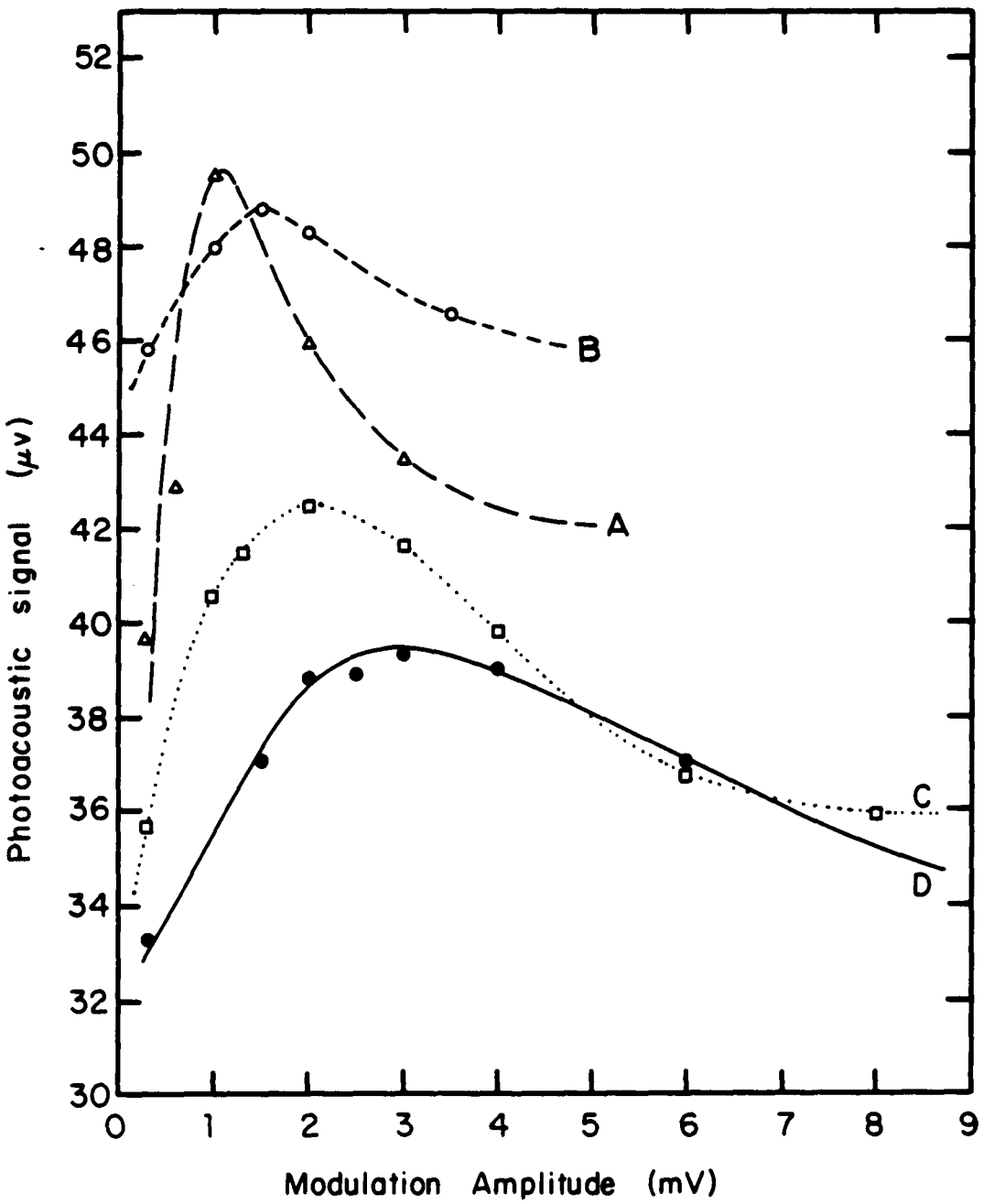

Figure 35. The effect of modulation amplitude on wavelength-modulated photoacoustic signal of NH_3 line at 872.59 cm^{-1} with 1.6 torr of NH_3 in various nitrogen pressure: A, 16.5 torr, B, 28.1 torr; C, 40.1 torr; D, 51.5 torr.

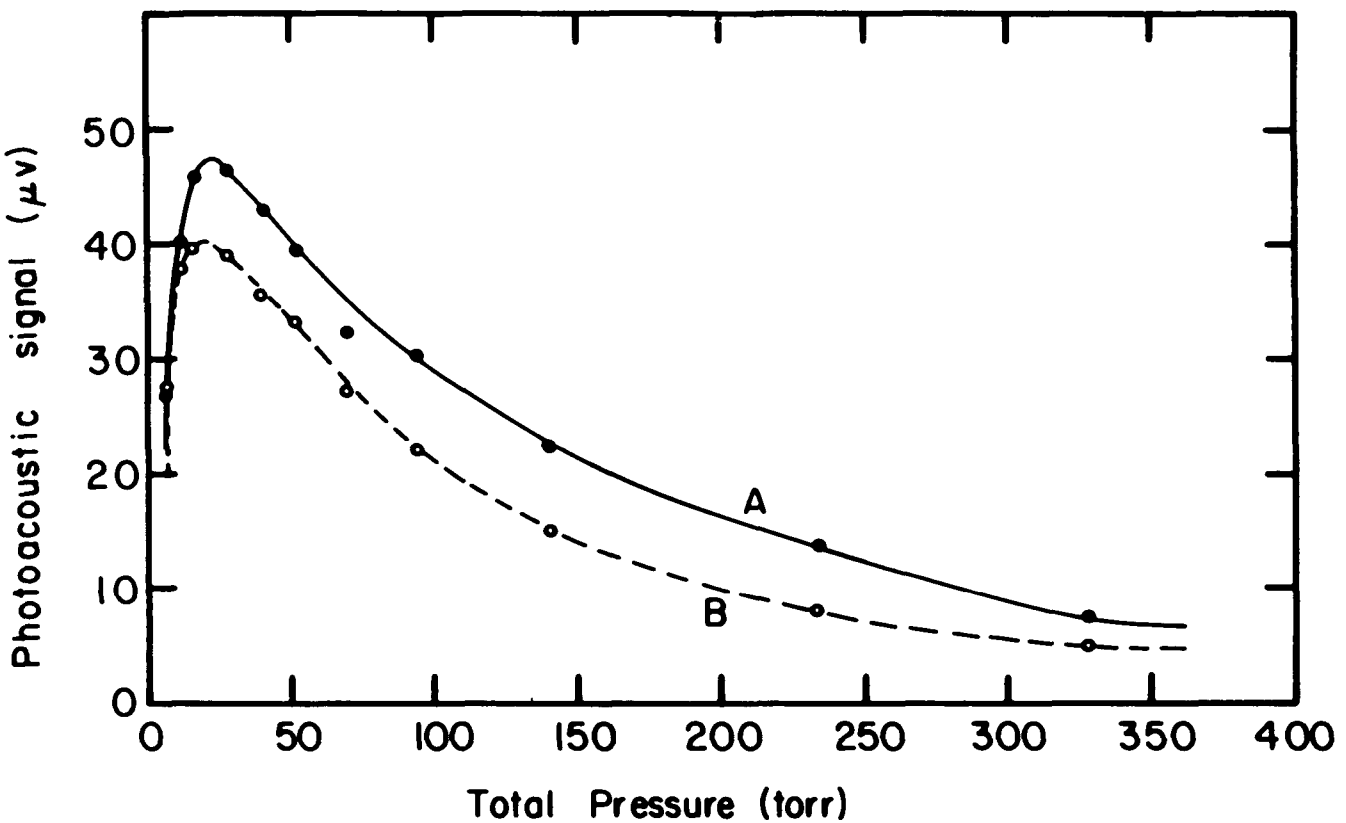

Figure 36. Wavelength-modulated photoacoustic signal vs. total pressure for 1.6 torr of NH_3 in nitrogen. Curve A has modulation amplitude fixed at 2 mV and B has that fixed at 0.3 mV. Modulation frequency is 109 Hz.

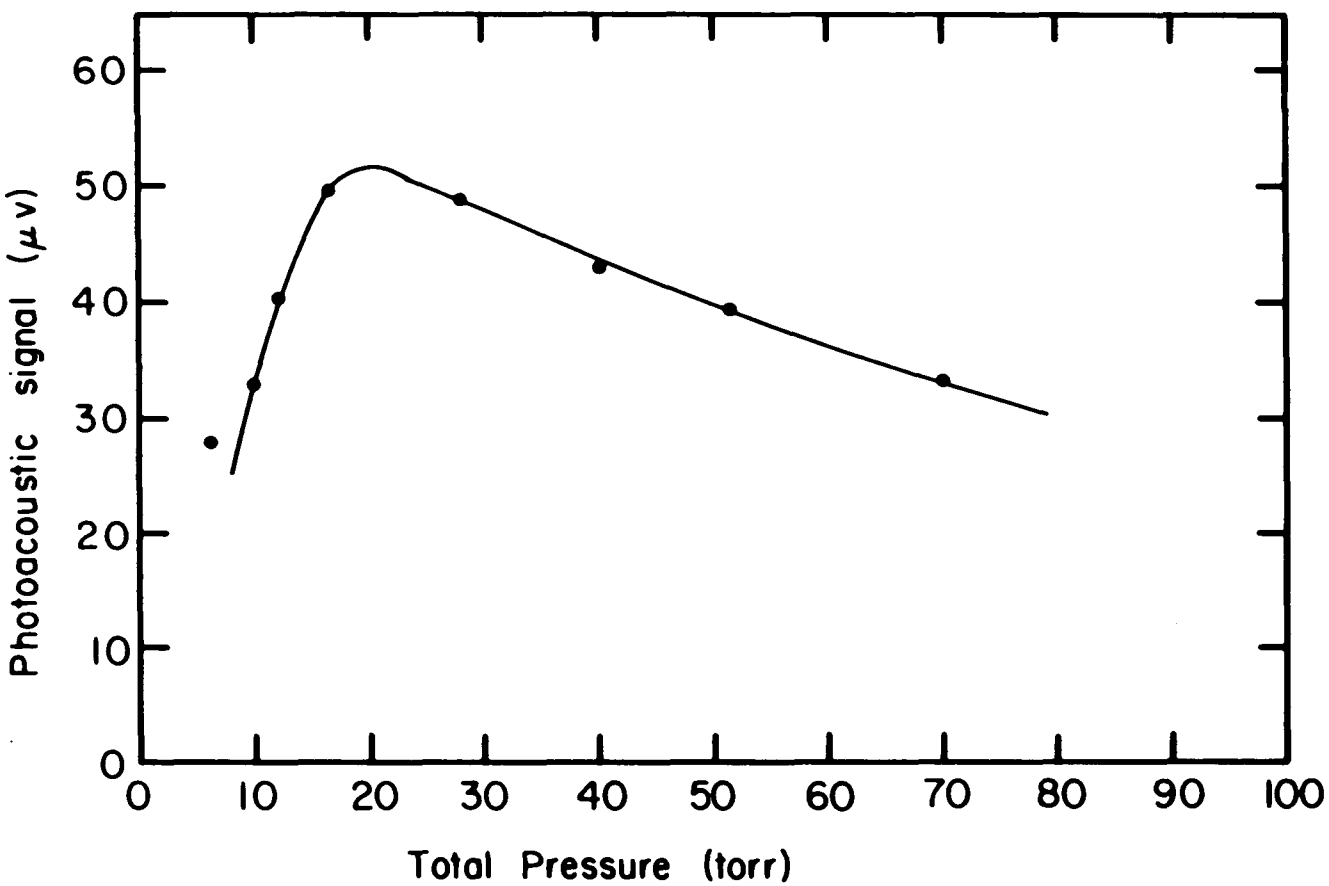

Figure 37. Wavelength-modulated photoacoustic signal vs. total pressure for 1.6 torr of NH_3 in nitrogen with optimum modulation amplitude at each pressure. Modulation frequency is 109 Hz.

at low pressure.

d. The effect of time constant on photoacoustic detection The signal-to-noise ratio (S/N) of the PAS detection could be improved by setting a longer time constant on lock-in amplifier. For example, if noise fluctuation cycle is within 3 second, then a 10-second time constant should smooth out the noise. However, before applying this to PAS detection, one should be certain that the scan rate of laser frequency over the absorption peak should be sufficiently slow so that the response of lock-in amplifier can follow the peak shape well. Otherwise, signal would be largely cut off at the same time when noise is cut off, and therefore, S/N does not benefit from the long time constant.

Normal PAS detection of 1.3 torr NH_3 in 40 torr nitrogen was performed with time constant setting of 1-second, 3-second and 10-second, as shown in Figure 38. The S/N was measured for each case and was found to have a factor of 3 of improvement for 10-second time constant over 1-second time constant. The S/N improvement on wavelength-modulated PAS detection was studied similarly and a similar factor of 3 to 4 of improvement was obtained. Further increase in the time constant would cause operational difficulty because of the very slow response. Therefore, it is decided to use time constant of 10-second in the study of detection limit of NH_3.

e. Detection limit of NH_3 The detection limit of our wavelength-modulated PAS system constructed in this work was examined by measuring PAS signal of 97 ppm NH_3 in nitrogen. Based on the studies of the effects of modulation amplitude, total pressure and lock-in amplifier time constant on wavelength-modulated PAS signal discussed

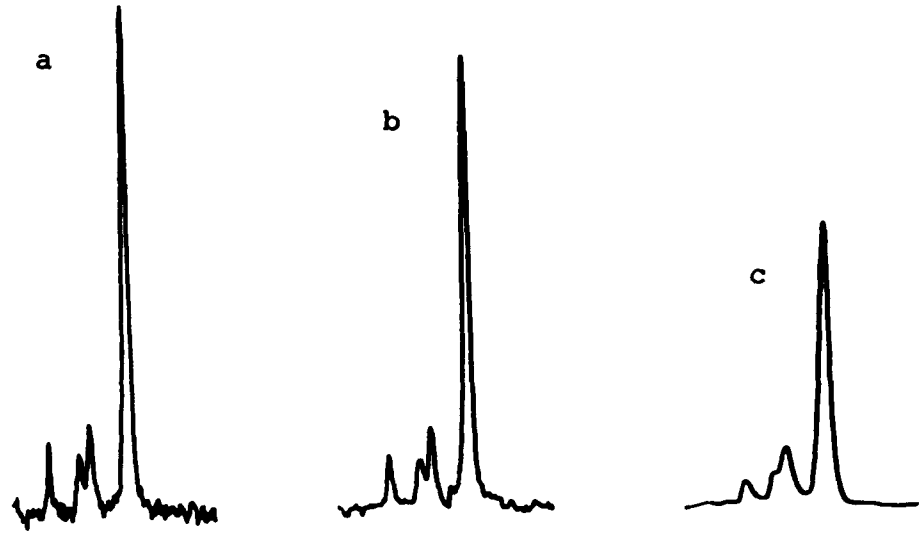

Figure 38. The effect of time constant on signal-to-noise ratio of photoacoustic detection for NH_3 line at 872.589 cm^{-1}. Gas sample is 1.3 torr of NH_3 in 40 torr of nitrogen. a, time constant = 1 second; b, time constant = 3 second; c, time constant = 10 second.

above, a total gas pressure of 20 torr and a time constant of 10-second were chosen, in addition, the modulation amplitude was adjusted to produce maximum signal.

The wavelength-modulated PAS signal under these experimental conditions is shown in Figure 39. The detection limit was estimated to be 25 ppm at S/N = 1 with estimated laser power of 84 μW in this mode. This is better than the detection limit obtained by Vansteenkiste et al. [152] for carbon monoxide using a line with similar absorption coefficient with a laser power of 96 μW.

The 97 ppm gas mixture was premixed in a stainless steel chamber of about 5 liters. A period of two hours was allowed for the adsorption of NH_3 onto the chamber walls before nitrogen was introduced into the chamber. Since adsorption is a function of partial pressure of NH_3, the introduction of nitrogen should not cause desorption of NH_3 from the chamber walls, thus the concentration obtained from the mixing process is reliable. However, when the 97 ppm NH_3 was introduced into the PAS cell, some of the NH_3 must have adsorbed onto the cell walls, windows etc., so the true NH_3 concentration in the cell must be less than 97 ppm. Therefore, the detection limit obtained above was the upper limit.

The detection limit obtained with this system is not sufficient to measure NH_3 concentration near pollution source, which is only a few ppm. However, there are some potential ways to improve this detection limit. First of all, the signal can be enhanced with the use of higher power laser since the photoacoustic signal increases proportionally as the power of the incident beam increases. The maximum power achieved by a diode laser was 50 mW in single mode [67] which is

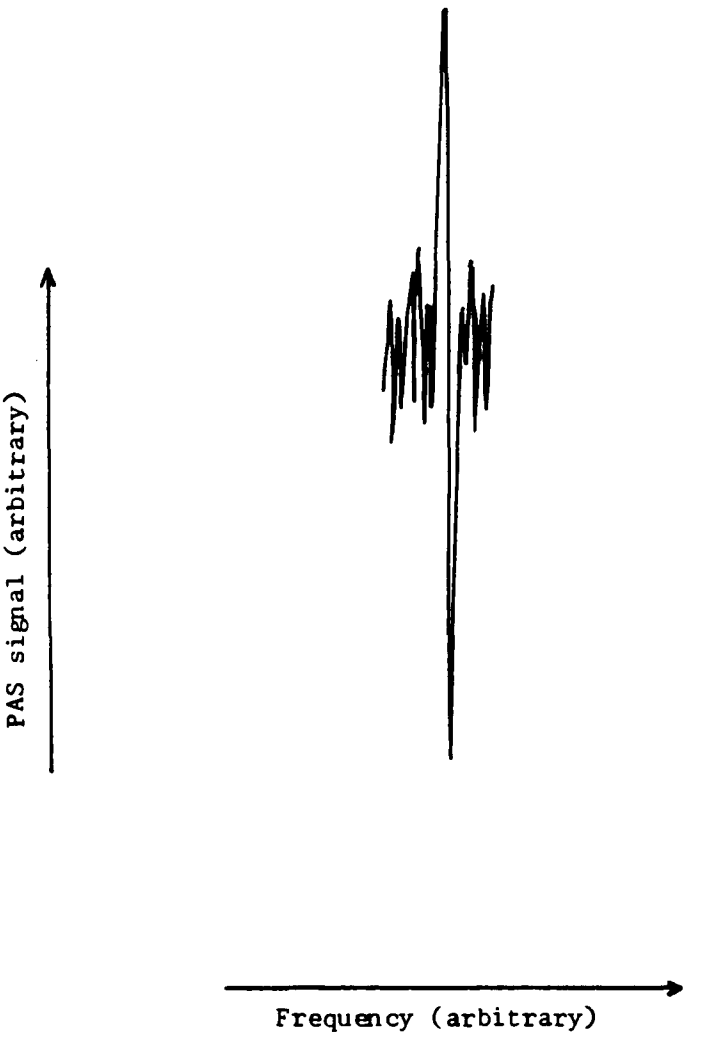

Figure 39. Wavelength-modulated photoacoustic signal of 97 ppm NH_3 in nitrogen. See text for experimental conditions.

about 600 times of the single mode power of our diode laser. Thus, the signal should be improved 600 times if such a diode laser is commercially available in the future. The window heating background is eliminated by wavelength-modulation technique, so the S/N is expected to be increased to the same extent as the signal does, i.e. a detection limit of 0.04 ppm can be achieved. Since window heating background is proportional to the laser power, higher power laser would actually benefit more from wavelength modulation technique. The diode laser is well suited for wavelength-modulation because its wavelength is controlled by injection current which in turn can be controlled easily by a circuit. Another type of tunable infrared laser suitable for wavelength-modulation is spin-flip Raman laser whose wavelength is controlled by the applied magnetic field. This type of lasers can be made with output power (1 watt, see Table 1) higher than that of diode lasers, therefore, a detection limit of 2 ppb can be expected.

However, the sensitivity of PAS system can not be improved indefinitely by simply going into more powerful lasers since at sufficiently high laser intensities (I_0) optical saturation effect occurs. In this case, the signal ceases to increase with increasing I_0 at high intensities, and eventually begins to decrease as $1/I_0$ at very high intensities [184]. Thus higher detectability with PAS must be achieved by reduction in the noise level rather than by simply using ever more powerful laser sources. To reduce the noise level, care must be taken to ensure mechanical and acoustical isolation of the detector. In addition, a better quality

microphone with lower broadband noise is necessary. Carefully designed electronics will further reduce the electronic noise introduced by amplification and signal processing, cable pick-up and other sources. An electronic noise of 20 nV was estimated to be achievable [162]. This is an improvement of more than 10 times better than the noise level in our system. In addition to the use of higher power laser, signal can be enhanced by the proper design of photoacoustic cell. According to Roessler and Foxvog [180], PAS signal is inversely proportional to cell volume, therefore, reducing the cell volume would enhance the signal. Other potential cell designs which can improve the signal is a multipass cell [150,160] in which the incident laser beam is passed back and forth many times, and a resonant cell which enhance signal by accumulating acoustic energy in a standing wave. However, both cell designs are more complicated than the simple cell used in this work.

D. Conclusion

In this work, we have performed the detection of NH_3 by wavelength-modulated photoacoustic detection technique. A detection limit of 25 ppm was obtained. Although this detection limit achievable by our current system is not really sufficient for the NH_3 analysis in air pollution, it is readily improvable to the sub-ppm level. For the detection of other gaseous air pollutants with higher concentration, such as in source monitoring of SO_2, CO, N_2O and NO, and CO monitoring in urban area, its sensitivity is still sufficient. The wavelength-modulated PAS detection system is especially suitable for point sampling and multicomponent

analysis since optimum signal occurs at low pressure. A flow cell developing by this group can be used in conjunction with this wavelength-modulated PAS system for in situ monitoring of air pollutants. The noise from turbulance introduced by the flowing of gas in the flow cell also can be reduced by the wavelength-modulation technique. And the flow cell system can be automated easily to perform essentially real-time analysis. For molecules that interact with cell or with each other, this system avoids potential errors produced by the interaction. Further, because of the small size of the diode lasers, the system can be made compact and movable for field study. Along with the capability of real-time analysis, the system is highly applicable to the air pollution study.

V. CONCLUSION

In this dissertation, we have studied the applications of tunable infrared diode lasers to the analysis of gaseous air pollutants in two ways. First, a simple and reliable internal calibration method was employed to determine the infrared linewidths and line positions with great accuracy. Since these line parameters are the basis of air pollution analysis, the demonstrated accuracy is therefore very important. The calibration method is very simple and can be easily performed on a daily basis. If a minicomputer is interfaced to the laser spectrometer, the calibration can be done in essentially real time. Second, the detectability of a wavelength-modulated photoacoustic detection system was examined through the detection of NH_3, an important gaseous air pollutant. Because of the low power of diode lasers, the achievement of good signal-to-noise ratio in photoacoustic detection system must depend on the reduction of noise level. Wavelength modulation provides a way to significantly reduce the background signal due to window heating, which is a principle source of noise. Even though the detection limit of this system is not yet satisfactory, it is expected to be improvable down to sub-ppm level by either using a higher power laser or reducing the electronic noise, or both. Optimizing the design of the PAS cell further will also improve the detectability. The compactness of the diode laser system allows itself to be easily adapted to field study of air pollutants. In conjunction with a flow cell and having the system automated, the wavelength-modulated PAS detection system can perform real-time air pollution analysis.

VI. BIBLIOGRAPHY

1. Singer, S. F. "Global Effects of Environmental Pollution"; Springer-Verlag: New York, 1970.

2. Diamant, R. M. E. "The Prevention of Pollution"; Pitman: London, 1974.

3. Singer, S. F. "The Changing Global Environment"; D. Reidel: Boston, 1975.

4. Shaheen, E. I. "Environmental Pollution -- Awareness and Control"; Engineering Technology Inc.: Mahomet, Illinois, 1974.

5. Sax, N. I. "Industrial Pollution"; Van Nostrand Reinhold: New York, 1974.

6. Saunders, P. J. W. "The Estimation of Pollution Damage"; Manchester University Press: Manchester, 1976.

7. Lund, T. "Surveillance of Environmental Pollution and Resources by Electromagnetic Waves"; D. Reidel: Dordrecht, Holland, 1978.

8. Thompson, C. R.; Kates, G.; Cameron, J. W. J. Environ. Qual. 1976, 5, 410.

9. Lippmann, M.; Schlesinger, R. S. "Chemical Contamination in the Human Environment"; Oxford University Press: New York, 1979.

10. Hodges, L. "Environmental Pollution," 2nd ed.; Holt, Rinehart and Winston: New York, 1977.

11. Spiro, T. G.; Stigliani, W. M. "Environmental Issues in Chemical Perspective"; State University of New York Press: Albany, New York, 1980.

12. American Chemical Society "Cleaning Our Environment -- A Chemical Perspective," 2nd ed.; ACS: Washington, D.C., 1978.

13. Morgan, G. B.; Ozolines, G.; Tabos, E. C. Science 1970, 170, 289.

14. Ziegler, E. N. In "Advances in Environmental Science and Engineering"; Pfafflin, J. R.; Ziegler, E. N., Eds.; Gordon and Breach: New York, 1979; Vol. 1, p. 184-194.

15. Panofsky, H. A. In "Advances in Environmental Science and Engineering"; Pfafflin, J. R.; Ziegler, E. N., Eds.; Gordon and Breach: New York, 1979; Vol. 1, p. 149-159.

16. Johnston, H. S. In "Tunable Lasers and Applications"; Mooradian, A.; Jaeger, T.; Stokseth, P., Eds.; Springer-Verlag: Berlin, 1976; p. 259-278.

17. Melfi, H. L. In "Laser Monitoring of the Atmosphere"; Hinkley, E. D., Ed.; Springer-Verlag: Berlin, 1976; Chapter 2.

18. Perry, R.; Young, R. J. "Handbook of Air Pollution Analysis"; Chapman and Hall: London, 1977.

19. Scott, W. E.; Stphens, E. R.; Hanst, P. L.; Doerr, R. C. Proc. Am. Petrol. Inst., Sect. III, 1957, 37, 171.

20. Crable, J. V.; Taylor, D. G. "NIOSH Manual of Analytical Methods"; HEW Pub. No. (NIOSH) 75-121, 1974.

21. Wilks, P. A., Jr. In "Microscopy/Pollution Analysis," Ser. 2; International Scientific Communications: Fairfield, Connecticut, 1977; Vol. 3, p. 252-254.

22. Maugh, T. H., II. Science 1972, 177, 685.

23. Byerly, R. IEEE Trans. 1975, NS-22, 856.

24. Collis, R. T. H.; Russel, P. B. In "Laser Monitoring of the Atmosphere"; Hinkley, E. D., Ed.; Springer-Verlag: Berlin, 1976; Chapter 4.

25. Menzies, R. T. In "Laser Monitoring of the Atmosphere"; Hinkley, E. D., Ed.; Springer-Verlag: Berlin, 1976; Chapter 6.

26. Hall, F. F., Jr. In "Laser Applications"; Ross, M., Ed.; Academic Press: New York, 1974; Vol. 2, p. 161.

27. Kildal, H.; Byer, R. L. Proc. IEEE 1971, 59, 1644.

28. Strötter, H. W. In "Advances in Infrared and Raman Spectroscopy"; Clark, R. J. H.; Hester, R. E., Eds.; Heydon and Son: London, 1981; Vol. 8, Chapter 1.

29. Inaba, H. In "Laser Monitoring of the Atmosphere"; Hinkley, E. D., Ed.; Springer-Verlag: Berlin, 1976; Chapter 5.

30. Kobayaki, T.; Inaba, H. Appl. Phys. Lett. 1970, 17, 139.

31. Schrötter, H. W.; Klöckner, H. W. In "Raman Spectroscopy of Gases and Liquids"; Weber, A., Ed.; Springer-Verlag: Berlin, 1979; Chapter 3.

32. Inaba, H.; Kobayaki, T. "Digest of Technical Papers," No. 12-1, 1970; Int. Quant. Electron Conf.: Kyoto, Japan, 1970.

33. Gelbwachs, J. A.; Birnbaum, M.; Tucker, A. W.; Fincher, C. L. Opto-Electronics 1972, 4, 155.

34. Birnbaum, M.; Tucker, A. W. Final Report to EPA No. EPA-650/2-73-059; May 1974.

35. Okabe, H.; Splitstone, D. L.; Ball, J. J. J. Air Pollut. Contr. Assoc. 1973, 23, 514.

36. Schnell, W.; Fischer, G. Appl. Opt. 1975, 14, 2058.

37. Hinkley, E. D. Opto-Electron. 1972, 4, 69.

38. Asai, K; Itabe, T.; Igarashi, T. Appl. Phys. Lett. 1979, 35, 60.

39. Menzies, R. T. Appl. Opt. 1971, 10, 1532.

40. Patty, R. R.; Russwurm, G. M.; McClenny, W. A.; Morgan, D. R. Appl. Opt. 1974, 13, 2850.

41. Brockman, P.; Bair, C. H.; Allario, F. Appl. Opt. 1978, 17, 91.

42. Butler, J. F.; Nill, K. W.; Mantz, A. W.; Eng, R. S. In "New Applications of Lasers to Chemistry," ACS Symposium Series No. 85; ACS: Washington, D.C., 1978; Chapter 2.

43. Baumgartner, R. A.; Byer, R. L. Appl. Opt. 1978, 17, 3555.

44. Pinard, J.; Young, J. F. Opt. Commun. 1972, 4, 425.

45. Evans, D. E.; Prunty, S. L.; Sexton, M. C. Infrared Phys. 1980, 20, 21.

46. Patel, C. K. N.; Burkhardt, E. G.; Lambert, C. A. Opt. Quant. Electron. 1976, 8, 145.

47. Jackson, D. J.; Gerhardt, H.; Hänsch, T. W. Opt. Commun. 1981, 37, 23.

48. Reid, J.; Garside, B. K.; Shewchun, J.; El-Sherbiny, M.; Ballik, E. A. Appl. Opt. 1978, 17, 1806.

49. Baldacchini, G.; Marchetti, S.; Montelatici, V. J. Mol. Spectrosc. 1981, 86, 115-121.

50. Kaiser, W.; Garrett, C. Phys. Rev. Lett. 1961, 7, 229.

51. Brunet, H.; Perez, M. J. Mol. Spectrosc. 1969, 29, 472.

52. McDowell, R. S.; Galbraith, H. W.; Cautrell, C. D.; Nereson, N. G.; Hinkley, E. D. J. Mol. Spectrosc. 1977, 68, 288.

53. Melngailis, I. In "Laser Spectroscopy"; Brewer, R. G.; Mooradian, A., Ed.; Plenum Press: New York, 1974; p. 237.

54. Hinkley, E. D.; Nill, K. W.; Blum, F. A. In "Laser Spectroscopy of Atoms and Molecules"; Walther, H., Ed.; Springer-Verlag: Berlin, 1976; Chapter 2.

55. Colles, M. J.; Pidgeon, C. R. Rep. Prog. Phys. 1975, 38, 329.

56. Preier, H. Appl. Phys. 1979, 20, 189.

57. Steinfeld, J. I. "Molecules and Radiation -- An Introduction to Modern Molecular Spectroscopy"; Harper and Row: New York, 1974.

58. Patel, C. K. N.; Shaw, E. D.; Kerl, R. J. Rev. Lett. 1970, 25, 8.

59. Hinkley, E. D.; Freed, C. Phys. Rev. Lett. 1969, 23, 277.

60. Ralston, R. W.; Melngailis, I.; Calawa, A. R.; Lindley, W. T. IEEE J. Quant. Elect. 1973, QE-9, 350.

61. Besson, J. M.; Paul, W.; Calawa, A. R. Phys. Rev. 1968, 173, 699.

62. Allario, F.; Bair, C. H.; Butler, J. F. IEEE J. Quant. Elect. 1975, QE-11, 205.

63. Hinkley, E. D.; Calawa, A. R.; Kelley, P. C.; Clough, S. A. J. Appl. Phys. 1972, 43, 3222.

64. Anzin, V. B.; Glushkov, M. V.; Kosichkin, Yu. V.; Nadezhdinskii, A. I. Appl. Phys. 1980, 22, 241.

65. Walpole, J. N.; Calawa, A. R.; Ralston, R. W.; Harman, T. C. J. Appl. Phys. 1973, 44, 2905.

66. Calawa, A. R. J. Lumin. 1973, 7, 477.

67. Ralston, R. W.; Walpole, J. N.; Calawa, A. R.; Harman, T. C.; McVittie, J. P. J. Appl. Phys. 1974, 45, 1323.

68. Walpole, J. N.; Calawa, A. R.; Ralston, R. W.; Harman, T. C.; McVittie, J. P. Appl. Phys. Lett. 1973, 23, 620.

69. Linden, K. J.; Nill, K. W.; Butler, J. F. IEEE J. Quant. Elect. 1977, QE-13, 720.

70. Walpole, J. N.; Calawa, A. R.; Harman, T. C.; Groves, S. H. Appl. Phys. Lett. 1976, 28, 552.

71. Preier, H.; Bleicher, M.; Riedel, W.; Maier, H. Appl. Phys. Lett. 1976, 28, 669.

72. Groves, S. H.; Nill, K. W.; Strauss, A. J. Appl. Phys. Lett. 1974, 25, 331.

73. Preier, H.; Bleicher, M.; Riedel, W.; Maier, H. J. Appl. Phys. 1976, 47, 5476.

74. Preier, H.; Bleicher, M; Riedel, W.; Pfeiffer, H.; Maier, H. Appl. Phys. 1977, 12, 277.

75. Walpole, J. N.; Calawa, A. R.; Chinn, S. R.; Groves, S. H.; Harman, T. C. Appl. Phys. Lett. 1977, 30. 524.

76. Lo, W. IEEE J. Quant. Elect. 1977, QE-13, 591.

77. Lo, W.; Swets, D. E. Appl. Phys. Lett. 1978, 33, 938.

78. Partin, D. L.; Lo, W. J. Appl. Phys. 1981, 52, 1579.

79. Oron, M.; Zussman, A. Appl. Phys. Lett. 1980, 37, 7.

80. Cole, A. R. H. "Tables of Wavenumbers for the Calibration of Infrared Spectrometers," 2nd ed.; Pergamon: Oxford, 1977.

81. McClatchey, R. A.; Benedict, W. S.; Clough, S. A.; Burch, D. E.; Calfee, R. F.; Fox, K.; Rothman, L. S.; Garing, J. S. Air Force Cambridge Research Labs. Report No. AFCRL-TR-73-0096, 1973.

82. Rothman, L. S.; Clough, S. A.; McClatchey, R. A.; Young, L. G.; Snider, D. E.; Goldman, A. Appl. Opt. 1978, 17, 507.

83. Knoll, J. S.; Tettemer, G. L.; Planet, W. G.; Rao, K. N.; Chen, D.-W.; Pugh, L. A. Appl. Opt. 1976, 15, 2973.

84. Montgomery, G. P.; Hill, J. C. J. Opt. Soc. Am. 1975, 65, 579.

85. Fayt, A.; Van Lerberghe, D.; Kupfer, J. P.; Pascher, H. P.; Häfele, H. G. Mol. Phys. 1977, 33, 603.

86. Wells, J. S.; Petersen, F. R.; Maki, A. G. Appl. Opt. 1979, 18, 3567.

87. Wells, J. S.; Petersen, F. R.; Maki, A. G.; Sukle, D. J. Appl. Opt. 1981, 20, 1676.

88. Petersen, F. R.; McDonald, D. G.; Cupp, J. D.; Danielson, B. L. In "Laser Spectroscopy"; Brewer, R. G.; Mooradian, A., Eds.; Plenum Press: New York, 1974; p. 555.

89. Blaney, T. G.; Edwards, G. J.; Jolliffe, B. W.; Knight, D. J. E.; Woods, P. T. J. Phys. D: Appl. Phys. 1976, 9, 1323.

90. Freed, C.; Ross, A. H. M.; O'Donnell, R. G. J. Mol. Spectrosc. 1974, 49, 439.

91. Menzies, R. T.; Shumate, M. S. IEEE J. Quant. Elect. 1973, QE-9, 862.

92. Kildal, H.; Eng, R. S.; Ross, A.H. M. J. Mol. Spectrosc. 1974, 53, 479.

93. Reddy, S. P.; Ivancic, W.; Devi, V. M.; Baldacci, A.; Rao, K. N.; Mantz, A. W.; Eng, R. S. Appl. Opt. 1979, 18, 1350.

94. Jennings, D. E. Appl. Opt. 1980, 19, 2695.

95. Flicker, H.; Aldridge, J. P.; Filip, H.; Nereson, N. G.; Reisfeld, M. J.; Weber, W. H. Appl. Opt. 1978, 17, 851.

96. Chraplyvy, A. R. Appl. Opt. 1978, 17, 2674.

97. Sattler, J. P.; Worchesky, T. L.; Ritter, K. J. Opt. Lett. 1980, 5, 21.

98. Lyszyk, M.; Depannemaecker, J. C.; Bantegnie, J. G.; Herlemont, F.; Lemaire, J.; Riant, Y. Opt. Commun. 1981, 37, 53.

99. Spears, D. L.; Freed, C. Appl. Phys. Lett. 1973, 23, 445.

100. Aukerman, L. W.; Erler, J. W. Opt. Lett. 1977, 1, 178.

101. Blum, F. A.; Nill, K. W.; Calawa, A. R.; Harman, T. C. Chem. Phys. Lett. 1972, 15, 144.

102. Nill, K. W.; Blum, F. A.; Calawa, A. R.; Harman, T. C. Appl. Phys. Lett. 1972, 21, 132.

103. Golden, B. M.; Yeung, E. S. Anal. Chem. 1975, 47, 2132.

104. McDowell, R. S. In "Advances in Infrared and Raman Spectroscopy"; Clark, R. J. H.; Hester, R. E., Eds.; Heyden and Son: London, 1978; Vol. 5, p. 38.

105. Montgomery, G. P., Jr. Appl. Opt. 1978, 17, 2299.

106. Eng, R. S.; Mantz, A. W. J. Mol. Spectrosc. 1979, 74, 388.

107. Montgomery, G. P., Jr.; Majkowski, R. F. Appl. Opt. 1978, 17, 173.

108. Eng, R. S.; Petagna, G.; Nill, K. W. Appl. Opt. 1978, 17, 1723.

109. Restelli, G.; Cappellani, F.; Melandrone, G. Chem. Phys. Lett. 1979, 66, 454.

110. Hirota, E.; J. Mol. Spectrosc. 1979, 74, 209.

111. Sattler, J. P.; Simonis, G. J. IEEE J. Quant. Elect. 1977, QE-13, 461.

112. Das, P. P.; Devi, V. M.; Rao, K. N. J. Mol. Spectrosc. 1980, 84, 305.

113. Cappellani, F.; Restelli, G. Infrared Phys. 1979, 19, 195.

114. Planet, W. G.; Tettemer, G. L.; Knoll, J. S. J. Quant. Spectrosc. Radiat. Transfer 1978, 20, 547.

115. Aronson, J. R.; Von Thüna, P. C.; Butler, J. F. Appl. Opt. 1975, 14, 1120.

116. Eng, R. S.; Mantz, A. W. J. Mol. Spectrosc. 1979, 74, 331.

117. Wahlen, M.; Eng, R. S.; Nill, K. W. Appl. Opt. 1977, 16, 2350.

118. Eng, R. S.; Nill, K. W.; Wahlen, M. Appl. Opt. 1977, 16, 3072.

119. Reddy, S. P.; Devi, V. M.; Baldacci, A.; Ivancic, W.; Rao, K. N. J. Mol. Spectrosc. 1977, 74, 217.

120. Das, P. P.; Devi, V. M.; Rao, K. N. J. Mol. Spectrosc. 1980, 84, 313.

121. Ohashi, N.; Kawaguchi, K.; Hirota, E. J. Mol. Spectrosc. 1981, 85, 427.

122. Menzies, R. T.; Margolis, J. S.; Hinkley, E. D.; Toth, R. A. Appl. Opt, 1977, 16, 523.

123. Nereson, N. J. Mol. Spectrosc. 1978, 69, 489.

124. Hillman, J. J.; Kostiuk, T.; Buhl, D.; Faris, J. L.; Novaco, J. C.; Mumma, M. J. Opt. Lett. 1977, 1, 81.

125. Cappellani, F.; Restelli, G. J. Mol. Spectrosc. 1979, 77, 36.

126. Sattler, J. P.; Ritter, K. J. J. Mol. Spectrosc. 1978, 69, 486.

127. Giorgianni, S. J. Mol. Spectrosc. 1980, 83, 228.

128. El-Sherbiny, M.; Ballik, E. A.; Shewchun, J.; Garside, B. K.; Reid, J. Appl. Opt. 1979, 18, 1198.

129. Forrest, G. T. Appl. Opt. 1980, 19, 2094.

130. Reid, J.; Shewchun, J.; Garside, B. K.; Ballik, E. A. Opt. Engineering 1978, 17, 56.

131. Forrest. G. T.; Vilcins, G. Appl. Spectrosc. 1980, 34, 418.

132. Reid, J.; Shewchun, J.; Garside, B. K.; Ballik, E. A. Appl. Opt. 1978, 17, 300.

133. Reid, J.; Garside, B. K.; Shewchun, J. Opt. Quant, Electron, 1979, 11, 385.

134. Hinkley, E. D.; Kelley, P. L. Science 1971, 171, 635.

135. Kreuzer, L. B.; Patel, C. K. N. Science 1971, 173, 45.

136. Hinkley, E. D. Final Report to EPA No. EPA-R2-73-218; May 1973.

137. Hinkley, E. D. Opt. Quant. Electron. 1976, 8, 155.

138. Ku, R. T.; Hinkley, E. D.; Sample, J. O. Appl. Opt. 1975, 14, 854.

139. Max, E.; Eng, S. T. Opt. Quant. Electron. 1979, 11, 97.

140. Chaney, L. W.; Rickel, D. G.; Russwurm, G. M.; McClenny, W. A. Appl. Opt. 1979, 18, 3004.

141. Kerr, E. L.; Atwood, J. G. Appl. Opt. 1968, 7, 915.

142. Rosengren, L. G.; Max, E.; Eng, S. T. J. Appl. Phys. 1974, E7, 125.

143. Claspy, P. C.; Pao, Y. H.; Kwong, S.; Nodov, E. Appl. Opt. 1976, 15, 1506.

144. Patel, C. K. W.; Burkhardt, E. G.; Lambert, C. A. Science 1974, 184, 1173.

145. Patel, C. K. N. Opt. Quant. Electron. 1976, 8, 145.

146. Burkhardt, E. G.; Lambert, C. A.; Patel, C. K. N. Science 1975, 188, 1111.

147. Kreuzer, L. B.; Kenyon, N. D.; Patel, C. K. N. Science 1972, 177, 347.

148. Konjević, N.; Jovićević, S. Spectrosc. Lett. 1979, 12, 259.

149. Dewey, C. F., Jr.; Kamm, R. D.; Hackett, C. E. Appl. Phys. Lett. 1973, 23, 633.

150. Goldan, P. D.; Goto, K. J. Appl. Phys. 1974, 45, 4350.

151. Deaton, T. F.; Depatie, D. A.; Walker, T. W. Appl. Phys. Lett. 1975, 26, 300.

152. Vansteenkiste, T. H.; Faxvog, F. R.; Roessler, D. M. Appl. Spectrosc. 1981, 35, 194.

153. Kreuzer, L. B. J. Appl. Phys. 1971, 42, 2934.

154. Rosengren, L.-G. Appl. Opt. 1975, 14, 1960.

155. Max, E.; Rosengren, L.-G. Opt. Commun. 1974, 11, 422.

156. Eng. R. S. Solid State Research (M.I.T. Lincoln Laboratory) 1974, 4, 36.

157. Claspy, P. C.; Pao, Y.H.; Kwong, S.; Nodov, E. IEEE/OSA Conf. Laser Engineering and Applications, Washington, D.C., Paper 9.10, 1975.

158. Bonczyk, P. A.; Ultee, C. J. Opt. Commun. 1972, 6, 196.

159. Kaldor, A.; Olson, W. B.; Maki, A. G. Science 1972, 176, 508.

160. Chakarian, C., Jr.; Weisbach, M. F. J. Opt. Soc. Am. 1973, 63, 342.

161. Shtrikman, S.; Slatkine, M. Appl. Phys. Lett. 1977, 31, 830.

162. Dewey, C. F., Jr. Opt. Engineering 1974, 13, 483.

163. Kavaya, M. J.; Margolis, J. S.; Shumate, M. S. Appl. Opt. 1979, 18, 2602.

164. Dewey, C. F., Jr. In "Optoacoustic Spectroscopy and Detection," Pao, Y.-H., Ed.; Academic Press: New York, 1977; p. 47.

165. Kamm, R. D. J. Appl. Phys. 1976, 47, 3550.

166. Kritchman, E.; Shtrikman, S.; Slatkine, M. J. Opt. Soc. Am. 1978, 1257.

167. Leslie, D. H.; Trusty, G. L. Appl. Opt. 1981, 20, 1941.

168. Patel, C. K. N.; Kerl, R. J. Appl. Phys. Lett. 1977, 30, 578.

169. Shimoda, K. In "High Resolution Laser Spectroscopy"; Shimoda, K., Ed.; Springer-Verlag: Berlin, 1976; Chapter 2.

170. Penner, S. S. "Quantitative Molecular Spectroscopy and Gas Emissivities"; Addison-Wesley: Cambridge, Mass., 1959.

171. Mitchell, A. C. G.; Zemansky, M. W. "Resonance Radiation and Excited Atoms"; Cambridge University Press: Cambridge, 1961.

172. Kielkopf, J. F. J. Opt. Soc. Am. 1973, 63, 987.

173. Morris, R. N. Ph.D. Dissertation, Iowa State University, Ames, Iowa, 1977.

174. Varanasi, P. J. Quant. Spectrosc. Radiat. Transfer 1972, 12, 1283.

175. Taylor, F. W. J. Quant. Spectrosc. Radiat. Transfer 1973, 13, 1181.

176. Antcliffe, G. A.; Wrokel, J. S. Appl. Optics 1972, 11, 1548.

177. Benedict, W. S.; Clough, S. A.; Frenkel, L.; Sullivan, T. E. J. Chem. Phys. 1970, 53, 2565.

178. Bell, A. G. Am. J. Sci. 1880, 20, 305.

179. Houghton, J. T.; Smith, D. S. "Infra-Red Physics"; Oxford: England, 1966, p. 276.

180. Roessler, D. M.; Foxvog, F. R. J. Opt. Soc. Am. 1979, 69, 1699.

181. Wake, D. R.; Amer, N. M. Appl. Phys. Lett. 1979, 34, 379.

182. Curtis, J. B. Ph.D. Dissertation, The Ohio State University, Columbus, Ohio, 1974.

183. Gerlach, R.; Amer, N. M. Appl. Phys. Lett. 1978, 32, 228.

184. Rosencwaig, A. "Photoacoustics and Photoacoustic Spectroscopy"; John Wiley & Sons: New York, 1980.

185. Snedecor, G. W.; Cochran, W. G. "Statistical Methods," 6th ed.; The Iowa State University Press: Ames, 1967.

VII. ACKNOWLEDGMENTS

I am deeply grateful to Dr. Edward S. Yeung for his generous assistance, constant encouragement and valuable guidance throughout my graduate school career at Iowa State.

I also would like to express my sincere appreciation to Dr. and Mrs. Velmer A. Fassel as well as Dr. and Mrs. George Burnet for their thoughtfulness in the past few years. Thanks are also due to J.C., Donna and Roger for their warm friendship.

Finally, my special thanks goes to my husband, Kan-Sen, whose love, understanding, sacrifice and unfailing support helped me to complete this research.

VIII. APPENDIX A: OPERATIONAL PROCEDURES FOR EXPERIMENTAL APPARATUS

A. Internal Calibration

1. Cooling the liquid He chamber to near liquid N_2 temperatures. (Although this cooling step is not absolutely necessary, the extra liquid He required to cool the liquid He chamber from room temperature is considerable and liquid He is expensive. This portion of the procedure should be done about twelve hours prior to the liquid He transfer operation.)

   Step 1. Make sure that the cryostat is being pumped by the liquid nitrogen trapped oil diffusion pump.

   Step 2. Fill the liquid N_2 chamber with liquid N_2. Stopper the inlet tube of the liquid N_2 chamber.

   Step 3. Run a tube from the liquid N_2 chamber exit tube to the entrance tube of the liquid He chamber.

   Step 4. Place bunsen valve on the liquid He chamber exit hole.

   Step 5. Place a bunsen valve on the He gas boil-off tube.

2. Semiconductor diode laser operational procedure.

   Step 1. Turn on the lock-in amplifier for warm-up.

   Step 2. Turn on the X-Y recorder for warm-up.

   Step 3. Attach vacuum line hose to the He gas boil-off tube.

   Step 4. Place the shorter end of the liquid He transfer tube into the liquid He chamber. Place a bunsen valve on the liquid N_2 exit tube.

   Step 5. Attach tubing from the He gas cylinder to the other end of the transfer tube.

   Step 6. Partially evacuate the He chamber being careful not to collapse the bunsen valve and letting air into the chamber.

   Step 7. Fill the chamber with He gas. He gas will rush out the bunsen valve when the chamber is full of gas.

   Step 8. Repeat steps 7 and 8 two more times.

   Step 9. Remove the bunsen valve and the vacuum line hose, attach the He return lines, and open the He return valve.

Step 10. Turn on the He gas cylinder momentarily and verify that He is passing through the He return line by observing the ping-pong ball movement in the check valve.

Step 11. Remove the rubber hose attached to the He cylinder from the bottom of the transfer tube and place the hose over the pressurizing tube on the side of the transfer tube.

Step 12. Place the long end of the He transfer tube into the liquid He dewar, being careful that the bottom of the transfer tube rests about an inch off the bottom and being careful not to freeze the rubber connecting tube before the transfer tube is in place.

Step 13. Pressurize the He dewar to about six pounds to drive the liquid He through the transfer tube into the cryostat.

Step 14. Fill the cryostat. When liquid He first enters the cryostat, all of the He will boil off until the cryostat becomes cold enough to retain liquid He. This change is marked by a large rush of He gas in the return line that gradually decreases. When the liquid He level nears the top of the cryostat, the rush of the He gas will again rise and this change can be used to ascertain when the cryostat is full.

Step 15. Quickly remove the transfer tube from both the cryostat and the dewar simultaneously and stopper the He chamber entrance tube.

Step 16. Measure and record the liquid He level in the dewar.

Step 17. Fill the detector with liquid N_2 and turn on the detector.

Step 18. Turn on the power to the tuning fork light chopper.

Step 19. Open the spectrometer slits to about 9000μ and set the monochromator reading to the region where the laser is expected to output.

Step 20. Remove the plastic covers from the optics and windows in the optical path.

Step 21. Connect HP regulated dc power supply to the current supply. Care must be taken to ascertain the right polarity connection. Turn on HP power supply. Set current to a proper value between 1.5 amp and 2 amp. Set voltage to zero.

Step 22. Turn on the current supply, voltage offset, and voltage ramp. Turn the short switch to the short position, and verify that current is flowing through the short switch

by observing the voltmeter attached to the current monitor terminal. (1 volt is equivalent to 1 amp of current.)

Step 23. With the short switch still in the short position and the internal-external switch in the internal position, connect the laser contacts to the power supply.

Step 24. Operate the internal-external switch to external, operate the short switch to open, slowly turn up the voltage of HP power supply to 20 V, and adjust the dc offset knob until the desired current is flowing through the laser.

Step 25. Fine tune the optics, the monochromator setting, and the gas cell to maximize the signal as displayed on the lock-in amplifier panel meter. Since signal can usually be seen, fine tuning is all that is needed unless some components in the optical path has been moved. In this case, it might require the realignment of the system.

Step 26. Decrease slit size to a value which will keep different modes from coming through the spectrometer at the same time (200μ). As the slits are changed further fine tuning may be necessary.

Step 27. Adjust the voltage ramp to the desired range for current scanning the laser.

Step 28. Adjust the X-Y plotter to have its minima and maxima correspond to the minimum and maximum of the voltage ramp and the minimum and maximum of the lock-in amplifier output.

Step 29. Turn on the A/D converter and the paper tape punch.

Step 30. Operate the rear switches on the A/D converter to 215 and operate the reset switch to ON. Allow about three feet of paper tape to be punched with the ASCII 215 for leader tape and then operate the reset switch to reset.

Step 31. Operate the rear switches to data.

Step 32. One is now ready to make an experimental run. Introduce the gas sample of interest into the gas cell, start the voltage ramp on the laser power supply, and operate the reset switch on the A/D converter to ON.

Step 33. At the end of an experimental run, block the light to generate a base line, operate the reset switch to reset to halt paper tape punching, operate the rear switches to 215, start the paper tape punch (reset switch to ON), generate 4 to 5 215s, press the M button and allow 4 to 5 Ms to be generated, and release the M button and allow

4 to 5 more 215s to be generated. Halt the paper tape punch and operate the rear switches to data.

Step 34. One is now ready for the next experimental run.

3. Shutdown procedure.

Step 1. When the liquid He is out or when no more runs are planned, slowly turn down the voltage of HP power supply to zero, operate the short switch to short and operate the internal-external switch on the power supply to internal.

Step 2. Disconnect the laser from the power supply.

Step 3. With the paper tape punch off, switch the rear switch on the A/D converter to 215, turn the paper tape punch ON, generate 4 or 5 215s, press the "Control D" button to generate 4 or 5 "Control Ds," release the Control D button and allow about three feet of trailer tape to be generated.

Step 4. Turn off all devices (order is not important) and cover the optics.

Step 5. Rewind the paper tape on the takeup reel so that the trailer tape is on the inside and the leader tape on the outside.

B. Wavelength-modulated PAS System

1. Cool the liquid He chamber to near liquid N_2 temperature as in (A).

2. Semiconductor diode laser operational procedure.

Step 1 through step 17 are the same as in (A).

Step 18. Remove the plastic covers from the optics and windows in the optical path.

Step 19. Connect the square wave generating circuit to the current supply. Connect HP power supply to the current supply. Care must be taken to ascertain the right polarity connection. Turn on HP power supply. Set current to a proper value between 1.5 amp and 2 amp. Set voltage to zero.

Step 20. Connect the microphone to its power supply. Turn on the current supply, square wave generator voltage offset, and voltage ramp. Turn the short switch to the short position, and verify that current is flowing through the short switch as in step 22 of (A).

Step 21. With square wave generator off, short switch in the short position, internal-external switch in the internal position, zero voltage and proper current setting on the HP power supply, connect the laser contacts to the power supply.

Step 22. Operate the internal-external switch to external, operate the short switch to open, turn on the square wave, slowly turn up the voltage on HP power supply to 20 V and adjust the dc offset knob until the desired current is flowing through the laser.

Step 23. Fine tune the optics and the gas cell to maximize the signal as displayed on the lock-in amplifier panel meter. Since signal can usually be seen, fine tuning is all that is needed unless some components in the optical path has been moved. In this case, it might require the realignment of the system.

Step 24. Adjust the voltage ramp to the desired range for current scanning the laser.

Step 25. Adjust the amplitude of the square wave to obtain the maximum signal.

Step 26. Adjust the X-Y recorder to have its minima and maxima correspond to the minimum and maximum of the voltage ramp and the minimum and maximum of the lock-in amplifier output.

3. Shutdown procedure.

Step 1. When the liquid He is out or when no more runs are planned turn the square wave amplitude to zero, operate the short switch to short and operate the internal-external switch on the power supply to internal.

Step 2. Disconnect the laser from the power supply.

Step 3. Turn off all the devices and cover the optics.

IX. APPENDIX B: COMPUTER PROGRAMS

This Appendix contains descriptions and listings of computer programs used in the internal calibration method.

A. Program I: Paper Tape Reading Program

This program reads the numbers, which have been punched on paper tape during the experimental run off the paper tape and punches thoses numbers on computer cards. The A/D converter is a twelve bit binary converter and the paper tape reader at the Iowa State University Computation Center is designed to read in seven bit ASCII code. Because three of the seven bits must be set in a particular fashion to signify that the other four bits are information bits, the twelve binary bits are divided into three groups of four bits when punched on the paper tape. Each group of three units of information are separated by an ASCII 215 which is a return character. The control cards at the end of the program signify that a 215 is the end of a "card image." Each group of four bits represents sixteen different possible units of information although only ten such units represent the numbers zero through nine. For this reason, the program reads the tape in A format and converts the alphanumeric information to an equivalent number zero through fifteen. The first value read is from the four most significant bits and is therefore multiplied by 16^2, the second value is from the next four significant bits and is multiplied by 16, and the third value, which is from the least significant bits, is taken as is and all three are then added together. Eight values at a time generated in this manner are then punched on computer cards. The program is always checking for the letter "M" in the alphanumeric values read. This "M" marks the end

of a particular run and the program prints the number of values which have been generated since the previous run on a separate card. Next, eighty "+'s" are printed on a card to facilitate manual separation of the entire deck into separate runs. An ASCII "control D" indicates the end of information on the paper tape. Four runs at a time are then placed on a Simplotter generated graph to help determine base lines, beginnings and endings of peaks, etc. for the next program which determines experimental parameters. The paper tape reading program follows.

```
/*JOBPARM CARDS=4000
//JOBLIB  DD  DSN=SYS2.PDPLIB,DISP=SHR
//S0  EXEC  PGM=FLOPPY
//SYSPRINT  DD  SYSOUT=A
//SYSUT1  DD  UNIT=PTAPEROR,VOL=SER=LINK1,
//  DCB=OPTCD=ZU
//SYSUT2  DD  DSN=C.A0035.LINK1,DISP=(NEW,CATLG),
//  DCB=(LRECL=10,BLKSIZE=3150,RECFM=FB),UNIT=DISK,VOL=SER=LIB001,
//  SPACE=(TRK,(5,2),RLSE)
//S1  EXEC  WATFIV,TIME.GO=(,10),REGION.GO=192K
//FT09F001  DD  DSN=C.A0035.LINK1,DISP=OLD,UNIT=DISK,
//    VOL=SER=LIB001,DCB=BUFNO=1
//GO.SYSIN  DD  *
$JOB    CHANG,TIME=5
       DIMENSIONX(2000),Y(2000)
       CHARACTER*1 A(6),B(80)/80*'+'/
       INTEGER*2 IX(3),J(255)/255*0/,INUM(8)
       EQUIVALENCE (IX,A)
       IX(1)=4
       IX(2)=0
       IX(3)=0
  111 FORMAT(3A1)
  222 FORMAT(8I10)
  333 FORMAT(80A1)
      J(241)=1
      J(242)=2
      J(243)=3
      J(244)=4
      J(245)=5
      J(246)=6
      J(247)=7
      J(248)=8
      J(249)=9
```

```
      J(122)=10
      J(94)=11
      J(76)=12
      J(126)=13
      J(110)=14
      J(111)=15
      KNT4=0
      KNT3=0
    7 KNT3=KNT3+1
      KNT=0
      DO1II=1,2000
      X(II)=II
      KNT2=II-1
      READ(9,111,END=3)A(2),A(4),A(6)
      IF(A(2).EQ.'M'.OR.A(4).EQ.'M')GOTO15
      IF(IX(1).LT.1)IX(1)=1
      IF(IX(2).LT.1)IX(2)=1
      IF(IX(3).LT.1)IX(3)=1
      KNT=KNT+1
      INUM(KNT)=J(IX(1))*256+J(IX(2))*16+J(IX(3))
      Y(II)=INUM(KNT)
      IF(KNT-8)1,16,16
   16 WRITE(7,222)(INUM(K),K=1,8)
      KNT=0
    1 CONTINUE
   15 IF(KNT)21,21,22
   22 WRITE(7,222)(INUM(K),K=1,KNT)
   21 WRITE(7,222)KNT2
      WRITE(7,333)(B(K),K=1,80)
      KNT4=KNT4+1
      IF(KNT4-1)61,61,62
   61 CALLGRAPH(KNT2,X,Y,KNT3,7,40.0,10.0,20.0,0.0,410.0,0.0,'X','Y','
     1','I')
```

```
      GOTO7
   62 CALLGRAPHS(KNT2,X,Y,KNT3,7,'I')
      IF(KNT4.EQ.4)KNT4=0
      GOTO7
    3 IF(KNT)27,27,28
   28 WRITE(7,222)(INUM(K),K=1,KNT)
   27 WRITE(7,222)KNT2
      CALLGRAPHS(KNT2,X,Y,KNT3,7,'I')
      STOP
      END
$ENTRY
//GO.FT14F001 DD DSNAME=&SM,UNIT=SCRTCH,DISP=(NEW,PASS),                    SMPLT1/3
// SPACE=(800,(120,15)),DCB=(RECFM=VBS,LRECL=796,BLKSIZE=800)               SMPLT2/3
//SMPLTTR EXEC PLOT,PLOTTER=INCRMNTL
//S1   EXEC  PGM=IEFBR14
//KILL  DD  DSN=C.AH035.LINK1,UNIT=DISK,DISP=(MOD,DELETE),
//    SPACE=(TRK,(1,1))
//KILL1  DD  DSN=&SM,UNIT=SCRTCH,DISP=(MOD,DELETE),
//   SPACE=(TRK,(1,1))
/*
//
```

B. Analytical Parameters Determining Programs

1. Program II(A): For peaks with negligible pressure broadening effect

This program is used for the determination of analytical parameters of experimental absorption peak at pressures that pressure broadening is negligible. It reads into memory all the experimental points, one run at a time, from the cards generated from the paper tape by the paper tape reading program. An average baseline for dark current is determined, and the points chosen by the programmer minus the points in the transmission peaks are fitted to a fourth degree polynomial to determine the 100% transmission value at each point in the transmission peak. Transmitted intensity, I, (in transmission unit) at each point in the transmission peak is then determined. The transmission at each point in the peak is then converted to an absorption value. Using programmer provided data for the analytical parameters, a theoretical absorption value is obtained at each point in the peak, and the difference between this value and the experimental value is squared and the squares are summed over all points in the peak. This procedure is followed for a range of values determined by the programmer for each analytical parameter, and the set of parameters which gives the smallest sum of the squares value is recorded. This parameter set is then used in the program III to generate and plot the theoretical peak.

The graphs which were produced by the paper tape reading program aid in choosing points for the baseline determination, beginning and

ending points for each peak, and starting values for line centers and half-widths at half maximum. The program follows.

```
C     THIS PROGRAM IS USED TO FIND OUT DOPPLER WIDTH.
C     IT USES VOIGT PROFILE, WITH VARIED DOPPLER WIDTH AND FIXED
C     LORENTZIAN WIDTH, TO FIND THE BEST FITTING FOR THE EXPERIMENTAL
C     PEAKS. IT ALSO CALCULATES AREA, CENTER FREQUENCY, ABSORPTION, AND
C     LINE WIDTH.
      PROGRAM MAIN(INPUT,OUTPUT,TAPE5=INPUT,TAPE6=OUTPUT)
      INTEGER SAMPLE(5),DATA(5),DATE(5)
      DIMENSION AX(1000),AY(1000),Y(1000),IPKMIN(6),IPKMAX(6),W(1500)
      DIMENSION TRANSY(200),SERROR(20,20,20),CNTR(6),HALFW(6)
      DIMENSION ALFA(6),DLTA(6),DLTW(6),DLTF(6)
      DOUBLEPRECISION D(5)
C   IDTSTS=NO OF DATA SETS.
C   ITOT = TOTAL NO OF POINTS.
C   IBMIN = STARTING POINT FOR BASE.
C   IBMAX = END POINT OF BASE.
C   NUMPKS = NUMBER OF PEAKS.
C   LOW = STARTING POINT FOR POLYNOMIAL FIT.
C   IHIGH = END POINT FOR THE FIT.
C   LOOPN 1,2 & 3 = NUMBER OF DO LOOPS OF PEAK, CENTER POSITION AND
C                   HALFWIDTH IN BEST FIT DETERMINATION OF THE
C                   ABSORPTION EQUATION.
C   IPKMIN(I) = STARTING POINT OF PEAK I.
C   IPKMAX(I) = END POINT OF PEAK I.
C   CNTR(I) = VISUAL GUESS FOR ABS CENTER OF PEAK I.
C   HALFW(I) = VISUAL GUESS FOR HALFWIDTH AT HALF MAX OF PEAK I(GAUSSIAN)
C   ALFA(I) = LORENTZIAN WIDTH
C   DLTA(I) = INCREMENTS OF PEAK I IN THE BEST FIT OF ABS EQUATION.
C               (IN ABS TRANSMITTANCE)
C   DLTW(I) = INCREMENTS OF HALFWIDTH AT HALF MAX IN THE BEST FIT OF
C               ABS EQUATION(IN PERCENT OF TRIAL WIDTH).
C   DLTF(I) = INCREMENTS OF POSITION CHANGE OF PEAK I CENTER.
C               (IN ABS HORIZONTAL UNITS)
      READ(5,111)IDTSTS
```

```
      DO 1951 IHAUCK=1,IDTSTS
      READ(5,110) (SAMPLE(K),K=1,5),(DATA(K),K=1,5),(DATE(K),K=1,5)
      READ(5,111)ITOT,IBMIN,IBMAX,NUMPKS,LOW,LOWB,IHIGHA,IHIGH
      READ(5,111)LOOPN1,LOOPN2,LOOPN3
      WRITE(6,777)
      WRITE(6,102) (SAMPLE(K),K=1,5),(DATA(K),K=1,5),(DATE(K),K=1,5)
      WRITE(6,100)ITOT,IBMIN,IBMAX,NUMPKS,LOW,LOWB,IHIGHA,IHIGH
      WRITE(6,103)LOOPN1,LOOPN2,LOOPN3
      DO 1 I=1,NUMPKS
      READ(5,111)IPKMIN(I),IPKMAX(I)
      READ(5,222)CNTR(I),HALFW(I),ALFA(I)
      READ(5,222)DLTA(I),DLTW(I),DLTF(I)
      WRITE(6,103)IPKMIN(I),IPKMAX(I)
      WRITE(6,104)CNTR(I),HALFW(I),ALFA(I)
      WRITE(6,104)DLTA(I),DLTW(I),DLTF(I)
    1 WRITE(6,101)
      READ(5,222)(Y(I),I=1,ITOT)
C
C     BASE AVERAGING
      AKNT1=0.
      TOT1=0.
      DO 2 I=IBMIN,IBMAX
      AKNT1=AKNT1+1.
    2 TOT1=TOT1+Y(I)
      BASE=TOT1/AKNT1
C
C     (X,Y) POINTS FROM BEGINNING TO START THE FIRST PEAK
      KNT2=0
      MIN=IPKMIN(1)
      DO 4 I=LOW,LOWB
      KNT2=KNT2+1
      AX(KNT2)=I
```

```
    4 AY(KNT2)=Y(I)
      IF (NUMPKS.EQ.1) GO TO 6
C
C       (X,Y) POINTS BETWEEN ALL PEAKS
      DO 3 I=2,NUMPKS
      II=I-1
      MAX=IPKMAX(II)
      MIN=IPKMIN(I)
      DO 5 J=MAX,MIN
      KNT2=KNT2+1
      AX(KNT2)=J
    5 AY(KNT2)=Y(J)
    3 CONTINUE
C
C       (X,Y) POINTS FROM LAST PEAK TO END
    6 MAX=IPKMAX(NUMPKS)
      DO 7 I=IHIGHA,IHIGH
      KNT2=KNT2+1
      AX(KNT2)=I
    7 AY(KNT2)=Y(I)
C
C         WEIGHTING FACTOR
      DO 8 I=1,KNT2
    8 W(I)=1.
C
C         POLYNOMIAL COFF DETERMINATION
      CALLOPLSPA(4,KNT2,AX,AY,W,Q,A,0)
      WRITE(6,555)(Q(I),I=1,5)
C
      DO 9 I=1,NUMPKS
      DLTW(I)=DLTW(I)*HALFW(I)/100.
      MINPK=IPKMIN(I)
      MAXPK=IPKMAX(I)
```

```
      KNT3=0
C
C     TRANSMITTANCE POINTS CALC FROM ENVELOPE AND BASE
      PEAK=1.
      DO 10 J=MINPK,MAXPK
      RILJ=J
      KNT3=KNT3+1
      TEMPY=Q(1)
      DO 11 K=2,5
      L=K-1
   11 TEMPY=TEMPY+Q(K)*RILJ**L
      TRANSY(KNT3)=(Y(J)-BASE)/(TEMPY-BASE)
      IF (TRANSY(KNT3).GT.PEAK) GO TO 10
      PEAK=TRANSY(KNT3)
   10 CONTINUE
      WRITE(6,666)I
      WRITE(6,444)(TRANSY(J),J=1,KNT3)
C
C     CALC OF TRUE AREA UNDER EXPT PEAK
      AREA=0.
      KNT4=0
      MAXPK1=MAXPK-1
      DO 12 J=MINPK,MAXPK1
      KNT4=KNT4+1
      KNT5=KNT4+1
   12 AREA=AREA+(ALOG10(1./TRANSY(KNT4))+ALOG10(1./TRANSY(KNT5)))/2.
      WRITE(6,333)I,AREA,CNTR(I),HALFW(I),ALFA(I),DLTA(I),DLTW(I),DLTF(I
     1)
C
C     LEAST SQUARES FOR A SERIES OF AREAS, HALFWIDTHS, AND FREQ CENTERS
      WL=ALFA(I)
      HLFLP1 = LOOPN1/2
      HLFLP2 = LOOPN2/2
```

```
      HLFLP3 = LOOPN3/2
      PEAK=PEAK-HLFLP1*DLTA(I)
      DO 13 IA=1,LOOPN1
      IF (PEAK.GT.1.) PEAK=1.
      IF (PEAK.LT.0.) PEAK=0.
      PP=ALOG10(1./PEAK)
      FSTRT=CNTR(I)-HLFLP2*DLTF(I)
      DO 14 IF=1,LOOPN2
      WSTRT=HALFW(I)-HLFLP3*DLTW(I)
      DO 15 IW=1,LOOPN3
      WD=WSTRT
      KNT6=0
      SERROR(IA,IF,IW)=0.
      DO 16 J=MINPK,MAXPK
      RILJ=J
      KNT6=KNT6+1
      CALL VOIGT (WL,WD,FSTRT,RILJ,U,PP)
   16 SERROR(IA,IF,IW)=SERROR(IA,IF,IW)+(1./10.**U-TRANSY(KNT6))**2
      RKNT6=KNT6
      SERROR(IA,IF,IW)=SERROR(IA,IF,IW)/RKNT6
   15 WSTRT=WSTRT+DLTW(I)
   14 FSTRT=FSTRT+DLTF(I)
   13 PEAK=PEAK+DLTA(I)
C
C     DETERMINATION OF AREA, HALFWIDTH AND FREQ CENTER
C         GIVING LEAST VALUE
      DO 55 IA=1,LOOPN1
      DO 55 IF=1,LOOPN2
      WRITE(6,999)IA,IF
      WRITE(6,444)(SERROR(IA,IF,IW),IW=1,LOOPN3)
   55 CONTINUE
      IREF=1
```

```
      JREF=1
      KREF=1
      CHECK=SERROR(1,1,1)
      DO 66 IA=1,LOOPN1
      DO 66 IF=1,LOOPN2
      DO 66 IW=1,LOOPN3
      IF (SERROR(IA,IF,IW)-CHECK)41,66,66
   41 CHECK=SERROR(IA,IF,IW)
      IREF=IA
      JREF=IF
      KREF=IW
   66 CONTINUE
      WRITE(6,888)IREF,JREF,KREF
      G1=LOOPN1+1-IREF
      PEAK=PEAK-G1*DLTA(I)
      PEAK=ALOG10(1./PEAK)
      G2=LOOPN2+1-JREF
      FSTRT=FSTRT-G2*DLTF(I)
      G3=LOOPN3+1-KREF
      WSTRT=WSTRT-G3*DLTW(I)
      WRITE(6,123)PEAK,FSTRT,WSTRT
      WRITE(6,777)
C
    9 CONTINUE
C
C
  100 FORMAT('0','THE INPUT DATA ARE'/8I10)
  101 FORMAT('0')
  102 FORMAT(' ','SAMPLE  ',5A4,5X,'DATA #  ',5A4,5X,'DATE  ',5A4)
  103 FORMAT(' ',8I10)
  104 FORMAT(' ',8F10.5)
  110 FORMAT(15A4)
  111 FORMAT(8I10)
```

```
 123 FORMAT(1X,'MIN PEAK =',F10.5,2X,'MIN FREQ CENTR =',F10.5,2X,'MIN H
    1ALFWIDTH =',F10.5)
 222 FORMAT(8F10.0)
 333 FORMAT(1X,'PEAK NO',I5,2X,'CENTER AREA =',F10.5,2X,'CENTER FREQ ='
    1,F10.5,2X,'CENTER HLF WDTH =',F10.5,/,1X,'ALFA      =',F10.5,2X,'PE
    2AK INC =',F10.5,2X,'WIDTH INC =',F10.5,2X,'FREQ INC =',F10.5)
 444 FORMAT(' ',8(1PE14.6,2X))
 555 FORMAT(1X,'POLYNOMIAL COEFFS ARE',1X,5(1PE14.6,2X)//)
 666 FORMAT(1X,'ADJUSTED TRANSMITTANCE FOR PEAK NO',I5)
 777 FORMAT('1')
 888 FORMAT('0',3I3)
 999 FORMAT(1X,'PEAK RUN = ',I5,2X,'FREQ RUN = ',I4)
1951 CONTINUE
     STOP
     END
     SUBROUTINE VOIGT (WL,WD,VZ,V,U,PEAK)
     A=WL/WD
     E2=ALOG(2.)
     ETA=.099
     EL=1.-ETA*E2
     EL=EL*EL+4.*E2/A/A
     EL=1.+ETA*E2+SQRT(EL)
     EL=2./EL
     BETA=WL/EL
     X=((V-VZ)/BETA)**2
     G=(1./E2)*(1.-EL*(1.+ETA*E2)+EL*EL*ETA*E2)
     ETA=EL/(EL+G)
     G=0.
     IF (E2*X.GT.100.) GO TO 21
     G=EXP(-E2*X)
  21 CONTINUE
     EL=1./(1.+X)
     E=(.8029-.4287*X)/(1.+.203*X+.07335*X*X)
```

```
      U=(1.-ETA)*G+ETA*EL+ETA*(1.-ETA)*E*(G-EL)
      U=U*PEAK
      RETURN
      END
      SUBROUTINE OPLSPA(NDEG,NPTS,X,Y,W,Q,TUWYLO)
      DIMENSION X(1),Y(1),W(1)
      DOUBLE PRECISION Q(1),PN(11),PN1(10),SUM(4),B,C,PNX,TMP
C          POLYNOMIAL FITTING ROUTINE
C     NDEG=DEGREE OF THE POLYNOMIAL
C              X=   VECTOR OF INDEPENDENT VARIABLES
C              Y=   VECTOR OF DEPENDENT VARIABLES
C              W=VECTOR  OF WEIGHTS
C              Q=VECTOR OF FITTED PARAMETERS CALC BY OPLSPA
C              TUWYLO MUST BE SET TO 0. BY THE CALLING ROUTINE
C              FOR OTHER USE OF THIS SWITCH, SEE BILL HIGBY FOR DETAILS.
      IF(TUWYLO) 2,1,2
    1 N=0
      C=0.
      PN(1)=1.0
      GO TO 6
    2 C=-SUM(3)/SUM(4)
    3 B=-SUM(1)/SUM(3)
      SUM(4)=SUM(3)
      N=N+1
      PN1(N)=0.
      PN(N+1)=0.
      DO 4 J=1,N
      TMP=PN(J)
      PN(J)=B*PN(J)+C*PN1(J)
    4 PN1(J)=TMP
      DO 5 J=1,N
    5 PN(J+1)=PN(J+1)+PN1(J)
```

```
    6 DO 7 K=1,3
    7 SUM(K)=0.0
      DO 11 I=1,NPTS
      PNX=1.0
      J=N
    8 IF(J) 10,10,9
    9 PNX=PN(J)+PNX*X(I)
      J=J-1
      GO TO 8
   10 SUM(1)=SUM(1)+W(I)*X(I)*PNX*PNX
      SUM(2)=SUM(2)+W(I)*Y(I)*PNX
   11 SUM(3)=SUM(3)+W(I)*PNX*PNX
      Q(N+1)=SUM(2)/SUM(3)
      IF(N)3,3,12
   12 DO 13 J=1,N
   13 Q(J)=Q(J)+Q(N+1)*PN(J)
      IF(N-NDEG)2,14,14
   14 RETURN
      END
```

2. Program II(B): For peaks with nonnegligible pressure broadening effect

This program is similar to program II(A), only the role of Doppler width and Lorentzian width is switched. It is used for absorption peak at pressures that pressure broadening is not negligible.

```
C     THIS PROGRAM IS FOR PRESSURE-BROADENED PEAKS.
C     IT USES VOIGT PROFILE, WITH FIXED DOPPLER WIDTH AND VARIED
C     LORENTZIAN WIDTH, TO FIND THE BEST FITTING FOR THE EXPERIMENTAL
C     PEAKS.  IT ALSO CALCULATES AREA, CENTER FREQUENCY, ABSORPTION,
C     AND LINE WIDTH.
      PROGRAM MAIN(INPUT,OUTPUT,TAPE5=INPUT,TAPE6=OUTPUT)
      INTEGER SAMPLE(5),DATA(5),DATE(5)
      DIMENSION AX(1500),AY(1500),Y(1500),IPKMIN(6),IPKMAX(6),W(1500)
      DIMENSION TRANSY(300),SERROR(20,20,20),CNTR(6),HALFW(6)
      DIMENSION ALFA(6),DLTA(6),DLTW(6),DLTF(6)
      DOUBLEPRECISION D(5)
C   IDTSTS=NO OF DATA SETS.
C   ITOT = TOTAL NO OF POINTS.
C   IAMIN = STARTING POINT FOR BASE.
C   IBMAX = END POINT OF BASE.
C   NUMPKS = NUMBER OF PEAKS.
C   LOW = STARTING POINT FOR POLYNOMIAL FIT.
C   IHIGH = END POINT FOR THE FIT.
C   LOOPN 1,2 & 3 = NUMBER OF DO LOOPS OF PEAK, CENTER POSITION AND
C                   HALFWIDTH IN BEST FIT DETERMINATION OF THE
C                   ABSORPTION EQUATION.
C   IPKMIN(I) = STARTING POINT OF PEAK I.
C   IPKMAX(I) = END POINT OF PEAK I.
C   CNTR(I) = VISUAL GUESS FOR ABS CENTER OF PEAK I.
C   HALFW(I) = VISUAL GUESS FOR HALFWIDTH AT HALF MAX OF PEAK I(GAUSSIAN)
C   ALFA(I) = LORENTZIAN WIDTH
C   DLTA(I) = INCREMENTS OF PEAK I IN THE BEST FIT OF ABS EQUATION.
C               (IN ABS TRANSMITTANCE)
C   DLTW(I) = INCREMENTS OF HALFWIDTH AT HALF MAX IN THE BEST FIT OF
C               ABS EQUATION(IN PERCENT OF TRIAL WIDTH).
C   DLTP(I) = INCREMENTS OF POSITION CHANGE OF PEAK I CENTER.
C               (IN ABS HORIZONTAL UNITS)
      READ(5,111)IDTSTS
      DO 1951 IHAUCK=1,IDTSTS
```

```
      READ(5,110) (SAMPLE(K),K=1,5),(DATA(K),K=1,5),(DATE(K),K=1,5)
      READ(5,111)ITOT,IBMIN,IBMAX,NUMPKS,LOW,LOWB,IHIGHA,IHIGH
      READ(5,111)LOOPN1,LOOPN2,LOOPN3
      WRITE(6,777)
      WRITE(6,102) (SAMPLE(K),K=1,5),(DATA(K),K=1,5),(DATE(K),K=1,5)
      WRITE(6,100)ITOT,IBMIN,IBMAX,NUMPKS,LOW,LOWB,IHIGHA,IHIGH
      WRITE(6,103)LOOPN1,LOOPN2,LOOPN3
      DO 1 I=1,NUMPKS
      READ(5,111)IPKMIN(I),IPKMAX(I)
      READ(5,222)CNTR(I),HALFW(I),ALFA(I)
      READ(5,222)DLTA(I),DLTW(I),DLTF(I)
      WRITE(6,103)IPKMIN(I),IPKMAX(I)
      WRITE(6,104)CNTR(I),HALFW(I),ALFA(I)
      WRITE(6,104)DLTA(I),DLTW(I),DLTF(I)
    1 WRITE(6,101)
      READ(5,222)(Y(I),I=1,ITOT)
C
C     BASE AVERAGING
      AKNT1=0.
      TOT1=0.
      DO 2 I=IBMIN,IBMAX
      AKNT1=AKNT1+1.
    2 TOT1=TOT1+Y(I)
      BASE=TOT1/AKNT1
C
C     (X,Y) POINTS FROM BEGINNING TO START THE FIRST PEAK
      KNT2=0
      MIN=IPKMIN(1)
      DO 4 I=LOW,LOWB
      KNT2=KNT2+1
      AX(KNT2)=I
    4 AY(KNT2)=Y(I)
      IF (NUMPKS.EQ.1) GO TO 6
C
```

```
C       (X,Y) POINTS BETWEEN ALL PEAKS
        DO 3 I=2,NUMPKS
        II=I-1
        MAX=IPKMAX(II)
        MIN=IPKMIN(I)
        DO 5 J=MAX,MIN
        KNT2=KNT2+1
        AX(KNT2)=J
      5 AY(KNT2)=Y(J)
      3 CONTINUE
C
C       (X,Y) POINTS FROM LAST PEAK TO END
      6 MAX=IPKMAX(NUMPKS)
        DO 7 I=IHIGHA,IHIGH
        KNT2=KNT2+1
        AX(KNT2)=I
      7 AY(KNT2)=Y(I)
C
C         WEIGHTING FACTOR
        DO 8 I=1,KNT2
      8 W(I)=1.
C
C         POLYNOMIAL COFF DETERMINATION
        CALLOPLSPA(4,KNT2,AX,AY,W,0,0,0)
        WRITE(6,555)(Q(I),I=1,5)
C
        DO 9 I=1,NUMPKS
        DLTW(I)=DLTW(I)*ALFA(I)/100.
        MINPK=IPKMIN(I)
        MAXPK=IPKMAX(I)
        KNT3=0
C
C       TRANSMITTANCE POINTS CALC FROM ENVELOPE AND BASE
```

```
      PEAK=1.
      DO 10 J=MINPK,MAXPK
      RILJ=J
      KNT3=KNT3+1
      TEMPY=Q(1)
      DO 11 K=2,5
      L=K-1
   11 TEMPY=TEMPY+Q(K)*RILJ**L
      TRANSY(KNT3)=(Y(J)-BASE)/(TEMPY-BASE)
      IF (TRANSY(KNT3).GT.PEAK) GO TO 10
      PEAK=TRANSY(KNT3)
   10 CONTINUE
      WRITE(6,666)I
      WRITE(6,444)(TRANSY(J),J=1,KNT3)
C
C     CALC OF TRUE AREA UNDER EXPT PEAK
      AREA=0.
      KNT4=0
      MAXPK1=MAXPK-1
      DO 12 J=MINPK,MAXPK1
      KNT4=KNT4+1
      KNT5=KNT4+1
   12 AREA=AREA+(ALOG10(1./TRANSY(KNT4))+ALOG10(1./TRANSY(KNT5)))/2.
      WRITE(6,333)I,AREA,CNTR(I),HALFW(I),ALFA(I),DLTA(I),DLTW(I),DLTF(I
     1)
C
C     LEAST SQUARES FOR A SERIES OF AREAS, HALFWIDTHS, AND FREQ CENTERS
      WD=HALFW(I)
      HLFLP1 = LOOPN1/2
      HLFLP2 = LOOPN2/2
      HLFLP3 = LOOPN3/2
      PEAK=PEAK-HLFLP1*DLTA(I)
      DO 13 IA=1,LOOPN1
```

```
      IF (PEAK.GT.1.) PEAK=1.
      IF (PEAK.LT.0.) PEAK=0.
      PP=ALOG10(1./PEAK)
      FSTRT=CNTR(I)-HLFLP2*DLTF(I)
      DO 14 IF=1,LOOPN2
      WSTRT=ALFA(I)-HLFLP3*DLTW(I)
      DO 15 IW=1,LOOPN3
      WL=WSTRT
      KNT6=0
      SERROR(IA,IF,IW)=0.
      DO 16 J=MINPK,MAXPK
      RILJ=J
      KNT6=KNT6+1
      CALL VOIGT (WL,WD,FSTRT,RILJ,U,PP)
   16 SERROR(IA,IF,IW)=SERROR(IA,IF,IW)+(1./10.**U-TRANSY(KNT6))**2
      RKNT6=KNT6
      SERROR(IA,IF,IW)=SERROR(IA,IF,IW)/RKNT6
   15 WSTRT=WSTRT+DLTW(I)
   14 FSTRT=FSTRT+DLTF(I)
   13 PEAK=PEAK+DLTA(I)
C
C     DETERMINATION OF AREA, HALFWIDTH AND FREQ CENTER
C         GIVING LEAST VALUE
      DO 55 IA=1,LOOPN1
      DO 55 IF=1,LOOPN2
      WRITE(6,999)IA,IF
      WRITE(6,444)(SERROR(IA,IF,IW),IW=1,LOOPN3)
   55 CONTINUE
      IREF=1
      JREF=1
      KREF=1
      CHECK=SERROR(1,1,1)
      DO 66 IA=1,LOOPN1
      DO 66 IF=1,LOOPN2
```

```
      DO 66 IW=1,LOOPN3
      IF (SERROR(IA,IF,IW)-CHECK)41,66,66
   41 CHECK=SERROR(IA,IF,IW)
      IREF=IA
      JREF=IF
      KREF=IW
   66 CONTINUE
      WRITE(6,888)IREF,JREF,KREF
      G1=LOOPN1+1-IREF
      PEAK=PEAK-G1*DLTA(I)
      PEAK=ALOG10(1./PEAK)
      G2=LOOPN2+1-JREF
      FSTRT=FSTRT-G2*DLTF(I)
      G3=LOOPN3+1-KREF
      WSTRT=WSTRT-G3*DLTW(I)
      WRITE(6,123)PEAK,FSTRT,WSTRT
      WRITE(6,777)
C
    9 CONTINUE
C
C
  100 FORMAT('0','THE INPUT DATA ARE'/8I10)
  101 FORMAT('0')
  102 FORMAT(' ','SAMPLE  ',5A4,5X,'DATA #  ',5A4,5X,'DATE  ',5A4)
  103 FORMAT(' ',8I10)
  104 FORMAT(' ',8F10.5)
  110 FORMAT(15A4)
  111 FORMAT(8I10)
  123 FORMAT(1X,'MIN PEAK =',F10.5,2X,'MIN FREQ CENTR =',F10.5,2X,'MIN H
     1ALFWIDTH =',F10.5)
  222 FORMAT(8F10.0)
  333 FORMAT(1X,'PEAK NO',I5,2X,'CENTER AREA =',F10.5,2X,'CENTER FREQ ='
     1,F10.5,2X,'CENTER HLF WDTH =',F10.5,/,1X,'ALFA     =',F10.5,2X,'PE
```

```
   2AK INC =',F10.5,2X,'WIDTH INC =',F10.5,2X,'FREQ INC =',F10.5)
 444 FORMAT(' ',8(1PE14.6,2X))
 555 FORMAT(1X,'POLYNOMIAL COEFFS ARE',1X,5(1PE14.6,2X)//)
 666 FORMAT(1X,'ADJUSTED TRANSMITTANCE FOR PEAK NO',I5)
 777 FORMAT('1')
 888 FORMAT('0',3I3)
 999 FORMAT(1X,'PEAK RUN = ',I5,2X,'FREQ RUN = ',I4)
1951 CONTINUE
     STOP
     END
     SUBROUTINE VOIGT (WL,WD,VZ,V,U,PEAK)
     A=WL/WD
     E2=ALOG(2.)
     ETA=.099
     EL=1.-ETA*E2
     EL=EL*EL+4.*E2/A/A
     EL=1.+ETA*E2+SQRT(EL)
     EL=2./EL
     BETA=WL/EL
     X=((V-VZ)/BETA)**2
     G=(1./E2)*(1.-EL*(1.+ETA*E2)+EL*EL*ETA*E2)
     ETA=EL/(EL+G)
     G=0.
     IF (E2*X.GT.100.) GO TO 21
     G=EXP(-E2*X)
  21 CONTINUE
     EL=1./(1.+X)
     E=(.8929-.4207*X)/(1.+.203*X+.97335*X*X)
     U=(1.-ETA)*G+ETA*EL+ETA*(1.-ETA)*E*(G-EL)
     U=U*PEAK
     RETURN
     END
     SUBROUTINE OPLSPA(NDEG,NPTS,X,Y,W,Q,TUWYLO)
```

```
      DIMENSION X(1),Y(1),W(1)
      DOUBLE PRECISION Q(1),PN(10),PN1(10),SUM(4),B,C,PNX,TMP
C          POLYNOMIAL FITTING ROUTINE
C     NDEG=DEGREE OF THE POLYNOMIAL
C               X=   VECTOR OF INDEPENDENT VARIABLES
C               Y=   VECTOR OF DEPENDENT VARIABLES
C               W=VECTOR  OF WEIGHTS
C               Q=VECTOR OF FITTED PARAMETERS CALC BY OPLSPA
C               TOWYLO MUST BE SET TO 0. BY THE CALLING ROUTINE
C               FOR OTHER USE OF THIS SWITCH, SEE BILL HIGBY FOR DETAILS.
      IF(TOWYLO) 2,1,2
    1 N=0
      C=0.
      PN(1)=1.0
      GO TO 6
    2 C=-SUM(3)/SUM(4)
    3 B=-SUM(1)/SUM(3)
      SUM(4)=SUM(3)
      N=N+1
      PN1(N)=0.
      PN(N+1)=0.
      DO 4 J=1,N
      TMP=PN(J)
      PN(J)=B*PN(J)+C*PN1(J)
    4 PN1(J)=TMP
      DO 5 J=1,N
    5 PN(J+1)=PN(J+1)+PN1(J)
    6 DO 7 K=1,3
    7 SUM(K)=0.0
      DO 11 I=1,NPTS
      PNX=1.0
      J=N
    8 IF(J) 10,10,9
```

```
 9 PNX=PN(J)+PNX*X(I)
   J=J-1
   GO TO 8
10 SUM(1)=SUM(1)+W(I)*X(I)*PNX*PNX
   SUM(2)=SUM(2)+W(I)*Y(I)*PNX
11 SUM(3)=SUM(3)+W(I)*PNX*PNX
   Q(N+1)=SUM(2)/SUM(3)
   IF(N)3,3,12
12 DO 13 J=1,N
13 Q(J)=Q(J)+Q(N+1)*PN(J)
   IF(N-NDEG)2,14,14
14 RETURN
   END
```

C. Program III: Spectrum Plotting Program

This program uses the best-fit parameter set obtained through programs II(A) and II(B) to generate the theoretical peak.

For each run a graph is produced upon the incremental plotter (Figure 11). The graph includes the experimental points, a continuous line representing the fourth degree polynomial for the 100% transmission curve, and a continuous line representing the theoretical transmission of each peak obtained from the theoretical absorption values which were obtained from the best fitting analytical parameters.

The subroutines GRAPH, GRAPHS, and OPLSPA are in the Fortran library at the I.S.U. Computation Center. GRAPH plots the points which are given it with a variety of possible marks along with scaling the axes and labeling the axes. GRAPHS adds additional (X,Y) points to the graph generated by the most recent GRAPH subroutine. OPLSPA fits a polynomial equation of specified degree to the (X,Y) point set transferred to it and passes back the coefficients of the polynomial.

```
//S1  EXEC  FORTG,REGION.GO=96K,TIME.GO=5
//FORT.SYSIN  DD  *
C  THIS PROGRAM IS USED TO PLOT THE SPECTRA, BOTH THEORETICAL AND EXPERIMENTAL
C  CURVES, AFTER THE CALCULATION HAS BEEN DONE WITH BERKELEY CDC COMPUTER.
      INTEGER SAMPLE(5),DATA(5),DATE(5)
      DIMENSION AX(1000),AY(1000),Y(1000),IPKMIN(8),IPKMAX(8)
      DIMENSION TRANSY(300),CNTR(8),HALFW(8)
      DIMENSION ALFA(8),BPEAK(8)
      DIMENSION Q(5)
C  IDTSTS=NO OF DATA SETS.
C  ITOT = TOTAL NO OF POINTS.
C  IBMIN = STARTING POINT FOR BASE.
C  IBMAX = END POINT OF BASE.
C  NUMPKS = NUMBER OF PEAKS.
C  LOW = STARTING POINT FOR POLYNOMIAL FIT.
C  IHIGH = END POINT FOR THE FIT.
C  IPKMIN(I) = STARTING POINT OF PEAK I.
C  IPKMAX(I) = END POINT OF PEAK I.
C  CNTR(I) = BEST FIT VALUE OF ABS CENTER OF PEAK I.
C  HALFW(I) = BEST FIT VALUE OF HALFWIDTH AT HALF MAX OF PEAK I (GAUSSIAN).
C  ALFA(I) = BEST FIT VALUE OF LORENTZIAN WIDTH.
C  BPEAK(I) = BEST FIT OF ABSORBANCE AT CENTER OF PEAK I.
C  Q(1) TO Q(5) = POLYNOMIAL COEFFICIENTS OF ENVELOPE.
      READ(5,111)IDTSTS
      DO 1951 IHAUCK=1,IDTSTS
      READ(5,110) (SAMPLE(K),K=1,5),(DATA(K),K=1,5),(DATE(K),K=1,5)
      READ(5,400) (Q(I),I=1,5)
      READ(5,111)ITOT,IBMIN,IBMAX,NUMPKS,LOW,LOWB,IHIGHA,IHIGH
      WRITE(6,777)
      WRITE(6,102) (SAMPLE(K),K=1,5),(DATA(K),K=1,5),(DATE(K),K=1,5)
      WRITE(6,555) (Q(I),I=1,5)
      WRITE(6,100)ITOT,IBMIN,IBMAX,NUMPKS,LOW,LOWB,IHIGHA,IHIGH
      DO 1 I=1,NUMPKS
```

```
      READ(5,111)IPKMIN(I),IPKMAX(I)
      READ(5,222)CNTR(I),HALFW(I),ALFA(I),BPEAK(I)
      WRITE(6,103)IPKMIN(I),IPKMAX(I)
      WRITE(6,104)CNTR(I),HALFW(I),ALFA(I),BPEAK(I)
    1 WRITE(6,101)
      READ(5,222)(Y(I),I=1,ITOT)
      DO 77 I=1,ITOT
   77 AX(I)=I
      IF (ITOT.GT.800)ITOT=800
      CALLGRAPH(ITOT,AX,Y,3,7,40.0,10.0,20.0,0.0,410.0,0.0,'X','Y',' '
     1,' ')
C
C     BASE AVERAGING
      AKNT1=0.
      TOT1=0.
      DO 2 I=IRMIN,IRMAX
      AKNT1=AKNT1+1.
    2 TOT1=TOT1+Y(I)
      BASE=TOT1/AKNT1
C
      DO 9 I=1,NUMPKS
      MINPK=IPKMIN(I)
      MAXPK=IPKMAX(I)
      KNT3=0
C
C     TRANSMITTANCE POINTS CALC FROM ENVELOPE AND BASE
      PEAK=1.
      DO 10 J=MINPK,MAXPK
      RILJ=J
      KNT3=KNT3+1
      TEMPY=Q(1)
      DO 11 K=2,5
```

```
      L=K-1
   11 TEMPY=TEMPY+Q(K)*RILJ**L
      TRANSY(KNT3)=(Y(J)-BASE)/(TEMPY-BASE)
      IF (TRANSY(KNT3).GT.PEAK) GO TO 10
      PEAK=TRANSY(KNT3)
   10 CONTINUE
      WRITE(6,666)I
      WRITE(6,444)(TRANSY(J),J=1,KNT3)
C
C  CALCULATION OF LEAST SQUARE FOR THE BEST FIT SET OF PEAK, HALFWIDTH, AND FREQ
C  CENTER
      WD=HALFW(I)
      PP=BPEAK(I)
      WL=ALFA(I)
      FSTRT=CNTR(I)
      KNT6=0
      SERROR=0.
      DO 16 J=MINPK,MAXPK
      RILJ=J
      KNT6=KNT6+1
      CALL VOIGT (WL,WD,FSTRT,RILJ,U,PP)
   16 SERROR=SERROR+(1./10.**U-TRANSY(KNT6))**2
      RKNT6=KNT6
      SERROR=SERROR/RKNT6
      WRITE(6,420) SERROR
C
C     DETERMINATION OF THEORETICAL POINTS OF TRANS OF PEAK
C          JUST CALCULATED
      KNT7=0
      DO 83 JJ=MINPK,MAXPK
      RILJ=JJ
      KNT7=KNT7+1
      AX(KNT7)=JJ
```

```
      CALL VOIGT (WL,WD,FSTRT,RILJ,U,PP)
      TRANS2=1./10.**U
   83 AY(KNT7)=TRANS2*(Y(JJ)-BASE)/TRANSY(KNT7)+BASE
      CALLGRAPHS(KNT7,AX,AY,3,4,'J')
    9 CONTINUE
C
C     DETERMINATION OF POINTS IN ENVELOPE EQN FROM STARTING POINT TO END
      KNT7=0
      DO 84 I=LOW,IHIGH
      RILI=I
      KNT7=KNT7+1
      AX(KNT7)=I
      AY(KNT7)=Q(1)
      DO 84 J=2,5
      L=J-1
   84 AY(KNT7)=AY(KNT7)+Q(J)*RILI**L
      CALLGRAPHS(KNT7,AX,AY,3,4,'J')
C
  100 FORMAT('0','THE INPUT DATA ARE'/8I10)
  101 FORMAT('0')
  102 FORMAT(' ','SAMPLE  ',5A4,5X,'DATA #  ',5A4,5X,'DATE  ',5A4)
  103 FORMAT(' ',8I10)
  104 FORMAT(' ',8F10.5)
  110 FORMAT(15A4)
  111 FORMAT(8I10)
  222 FORMAT(8F10.0)
  400 FORMAT(5(1PE14.6))
  420 FORMAT('0','THE LEAST SQUARE IS  ',1PE14.6)
  444 FORMAT(' ',8(1PE14.6,2X))
  555 FORMAT('0','POLYNOMIAL COEFFS ARE',1X,5(1PE14.6,2X))
  666 FORMAT(1X,'ADJUSTED TRANSMITTANCE FOR PEAK NO',I5)
  777 FORMAT('1')
 1951 CONTINUE
```

```
      STOP
      END
      SUBROUTINE VOIGT (WL,WD,VZ,V,U,PEAK)
      A=WL/WD
      E2=ALOG(2.)
      ETA=.999
      EL=1.-ETA*E2
      EL=EL*EL+4.*E2/A/A
      EL=1.+ETA*E2+SQRT(EL)
      EL=2./EL
      BETA=WL/EL
      X=((V-VZ)/BETA)**2
      G=(1./E2)*(1.-EL*(1.+ETA*E2)+EL*EL*ETA*E2)
      ETA=EL/(EL+G)
      G=0.
      IF (E2*X.GT.100.) GO TO 21
      G=EXP(-E2*X)
   21 CONTINUE
      EL=1./(1.+X)
      E=(.8029-.4287*X)/(1.+.203*X+.97335*X*X)
      U=(1.-ETA)*G+ETA*EL+ETA*(1.-ETA)*E*(G-EL)
      U=U*PEAK
      RETURN
      END
//GO.SYSIN  DD  *
//GO.FT14F001 DD DSNAME=ASM,UNIT=SCRTCH,DISP=(NEW,PASS),                SMPLT1/3
   SPACE=(800,(120,15)),DCB=(RECFM=VBS,LRECL=796,BLKSIZE=800)          SMPLT2/3
//SMPLTTR EXEC PLOT,PLOTTER=INCRMNTL
/*
```

X. APPENDIX C: CALCULATIONS FOR FITTING A LINEAR REGRESSION PASSING THROUGH THE ORIGIN

The mathematical equations used in the calculation of the fitted line and its standard deviation for linear regression passing through the origin, i.e. $Y = aX$, are as follows [185].

The slope of the fitted line can be expressed as

$$a = \Sigma X_i Y_i / \Sigma X_i^2$$

and the standard deviation of the slope is

$$S_a = [S_{y \cdot x}^2 / \Sigma (X_i - \bar{X})^2]^{\frac{1}{2}}$$

where

$$S_{y \cdot x}^2 = \left[\Sigma Y_i^2 - \frac{(\Sigma X_i Y_i)^2}{\Sigma X_i^2}\right] / (n-1)$$

and

n is the number of measurements,

X_i is the X of the ith measurement,

Y_i is the Y of the corresponding ith measurement,

and $\bar{X}$ is the arithmetic mean of the n measurements.